was found that, the main products from the ethanol steam reforming over Ni/CeO_2 (HSA) were H_2, CO, CO_2, and CH_4, with small amounts of C_2H_4 and C_2H_6 depending on the operating temperature. In contrast, significant amounts of C_2H_4 and C_2H_6 were also observed as well as other chemical components from the ethanol steam reforming over Ni/CeO_2 (LSA) and Ni/Al_2O_3 in the range of conditions studied. Consequently, less H_2, CO, and CO_2 selectivities were achieved over these catalysts.

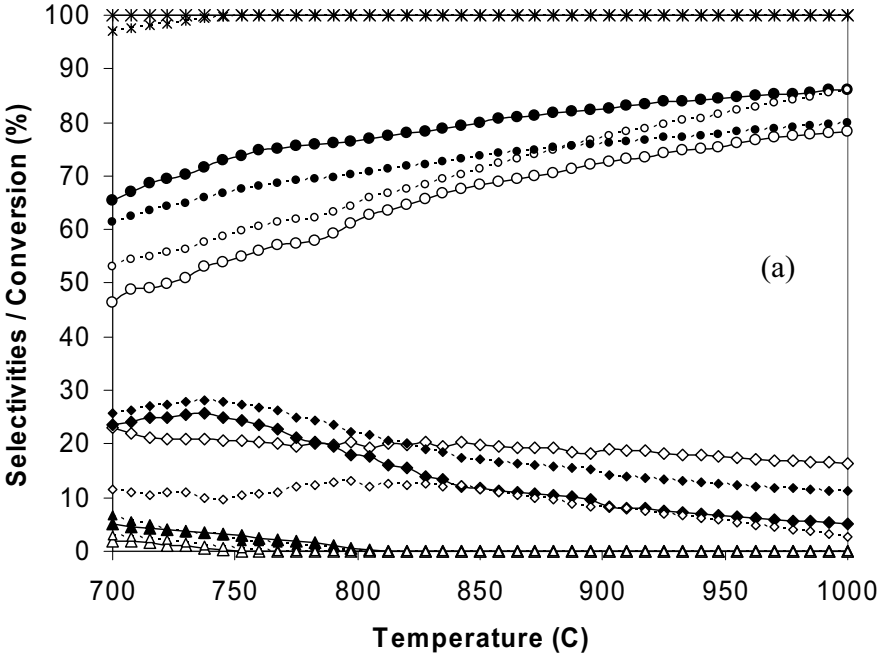

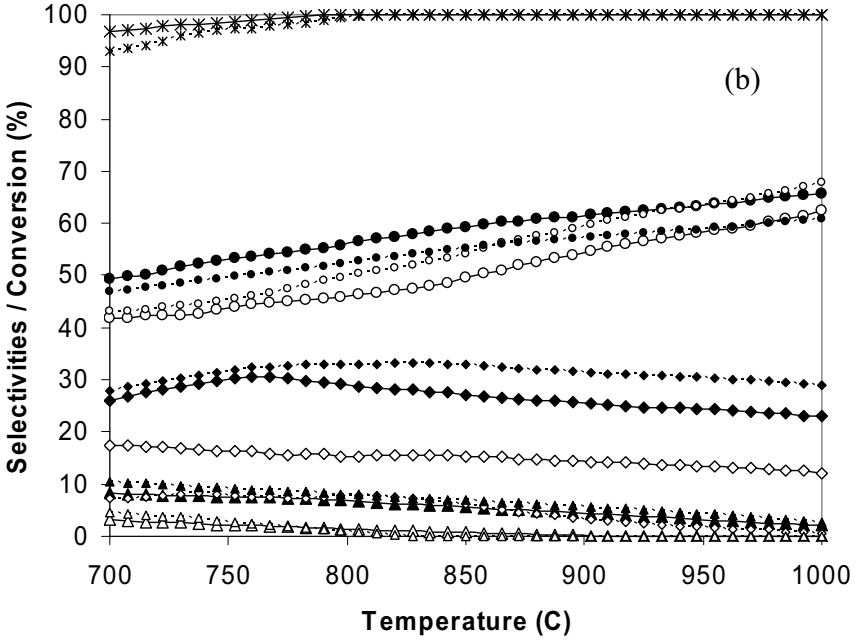

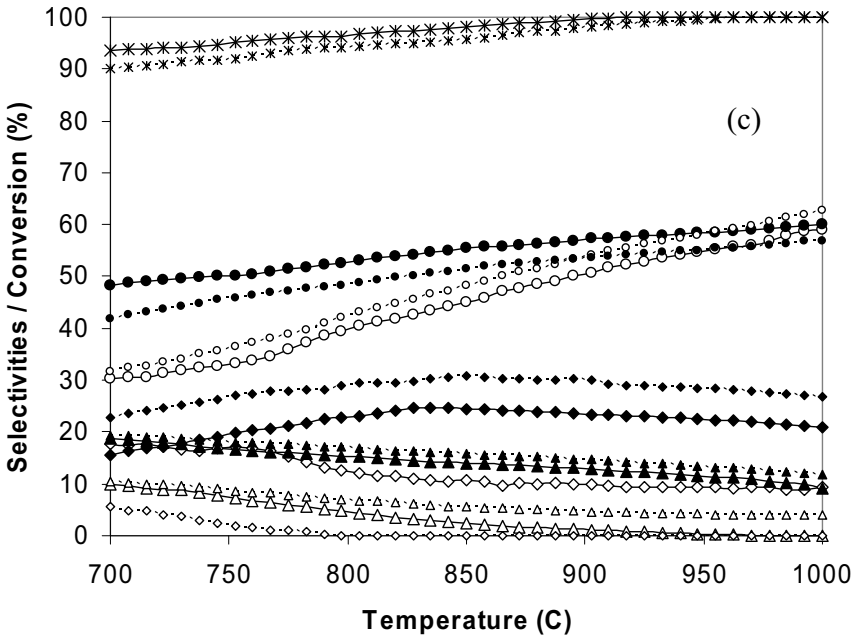

Figure 4 Effect of temperature on the conversion and product selectivities (EtOH (×), H_2 (●), CO (○), CO_2 (◇), CH_4 (◆), C_2H_6 (△), and C_2H_4 (▲)) from ethanol steam reforming over Ni/CeO_2 (HSA) (a), Ni/CeO_2 (LSA) (b), and Ni/Al_2O_3 (c) with inlet EtOH/H_2O ratios of 1/3 (large symbols with solid lines) and 1/2 (small symbols with dot lines).

It can be concluded that Ni/CeO_2 (HSA) was found in this study to be a promising catalyst for the steam reforming of ethanol. This catalyst provided excellent resistance toward carbon deposition compared to conventional Ni/CeO_2 (LSA) and Ni/Al_2O_3. At the temperature higher than 800ºC, the main products from the reforming of ethanol over Ni/CeO_2 (HSA) were H_2, CO, CO_2, and small amount of CH_4; neither C_2H_4 nor C_2H_6 was observed from the system over this catalyst. In contrast, the steam reforming of ethanol over Ni/CeO_2 (LSA) and Ni/Al_2O_3 formed significant amounts of C_2H_4 and C_2H_6, in addition, high amount of carbon deposition was also observed over these catalysts. The high resistance toward carbon deposition for CeO_2 especially high surface area CeO_2 was reported in our previous publications and is mainly due to the high oxygen storage capacity (OSC) of this material. CeO_2 contains a high concentration of highly mobile oxygen vacancies and thus acts as a local source or sink for oxygen on its surface. It has been reported that at high temperature the lattice oxygen (O_x) at the CeO_2 surface can oxidize gaseous hydrocarbons (methane, ethane, and propane). Although conventional CeO_2 (CeO_2 (LSA)) has also been reported to provide high resistance toward carbon formation, the major weaknesses of CeO_2 (LSA) are its low specific surface area and also high size reduction due to the thermal sintering impact, resulting in its significant lower redox properties than CeO_2 (HSA), and its lower Ni dispersion percentage on the surface compared to Ni/CeO_2 (HSA) and Ni/Al_2O_3. These disadvantages result in the low ethanol steam reforming reactivity for Ni/CeO_2 (LSA). By using Ni/CeO_2 (HSA) as the catalyst, in addition to the reaction on Ni surface, ethane and ethylene formations and the possible carbon depositions from these hydrocarbons could be inhibited by the gas-solid reactions between these hydrocarbons and the lattice oxygen (O_x) at CeO_2 surface forming hydrogen and carbon dioxide, which are thermodynamically unflavored to form carbon species, as illustrated schematically below.

$C_2H_6 + 2S \Leftrightarrow 2(CH_3\text{-}S)$ (1)

$C_2H_4 + 2S \Leftrightarrow 2(CH_2\text{-}S)$ (2)

$CH_4 + 2S \Leftrightarrow CH_3\text{-}S + H\text{-}S$ (3)

$CH_3\text{-}S + S \Leftrightarrow CH_2\text{-}S + H\text{-}S$ (4)

$CH_2\text{-}S + S \Leftrightarrow CH\text{-}S + H\text{-}S$ (5)

$CH\text{-}S + S \Leftrightarrow C\text{-}S + H\text{-}S$ (6)

$C\text{-}S + O_x \Leftrightarrow CO + O_{x-1} + S$ (7)

$2H\text{-}S \Leftrightarrow H_2 + 2S$ (8)

S is the catalyst surface site and CH_x-S is an intermediate surface hydrocarbon species. During the steam reforming, the lattice oxygen is regenerated by reaction with oxygen containing compounds (steam) present in the system.

Conclusion

Ni on high surface area CeO_2 support (Ni/CeO_2 (HSA)) provides excellent reactivity toward the steam and autothermal reforming of ethanol with high resistance toward carbon deposition and better product selectivities compared to Ni/Al_2O_3 and Ni on conventional low surface area ceria (Ni/CeO_2 (LSA)). The main products from these reforming processes over Ni/CeO_2 (HSA) were H_2, CO, and CO_2 with small amount of CH_4, whereas the formations of C_2H_4 and C_2H_6 were also observed together with the above gas components from the reactions over Ni/CeO_2 (LSA) and Ni/Al_2O_3 in the range of conditions studied. The great benefits of Ni/CeO_2 (HSA) in terms of stability and reactivity toward ethanol reforming, high resistance toward carbon deposition, and good product selectivities are due to the high redox property of CeO_2 (HSA).

Acknowledgments

The supports from the Thailand Research Fund (TRF) and National Metal and Materials Technology Center (MTEC) are gratefully acknowledged.

References

1. P. Aguiar, D. Chadwick and L. Kershenbaum, *Chem. Eng. Sci*. **57**, 1665 (2002).
2. S. Cavallaro, S. Freni, *Int. J. Hydrogen Energy* **21**, 465 (1996).
3. N.F. Athanasio, X.E. Verykios, *J. Catal*. **225**, 39 (2004).
4. S. Cavallaro and S. Freni. *Int. J. Hydrogen Energy* **21**, 465 (1996).
5. S. Cavallaro. *Energy and Fuels* **14**, 1195 (2000).
6. S. Freni. *J. Power Sour*. **94**, 14 (2001).
7. S. Freni, S. Cavallaro, N. Mondello, L. Spadaro, F. Frusteri. *J. Power Sour*. **108**, 53 (2002).
8. N. Laosiripojana and S. Assabumrungrat, *Appl. Catal. B: Environ*. **60**, 107 (2005).
9. N. Laosiripojana, W. Sutthisripok, and S. Assabumrungrat, *Chem. Eng. J.* **112**, 13 (2005).
10. N. Laosiripojana, W. Sangtongkitcharoen, and S. Assabumrungrat, *Fuel* **85**, 323 (2006).
11. D. Terribile, A. Trovarelli, J. Llorca, C. de Leitenburg and G. Dolcetti, *Catal. Today* **43**, 88 (1998).

ELSEVIER

Chemical Engineering Journal 138 (2008) 264–273

Chemical Engineering Journal

www.elsevier.com/locate/cej

Effect of high surface area CeO_2 and Ce-ZrO_2 supports over Ni catalyst on CH_4 reforming with H_2O in the presence of O_2, H_2, and CO_2

N. Laosiripojana [a,*], D. Chadwick [b], S. Assabumrungrat [c]

[a] *The Joint Graduate School of Energy and Environment, King Mongkut's University of Technology Thonburi, Bangkok 10140, Thailand*
[b] *Department of Chemical Engineering, Imperial College London SW7 2AZ, UK*
[c] *Center of Excellence on Catalysis and Catalytic Reaction Engineering, Department of Chemical Engineering, Chulalongkorn University, Bangkok 10330, Thailand*

Received 31 January 2007; received in revised form 9 May 2007; accepted 17 May 2007

Abstract

Methane steam reforming over Ni on high surface area (HSA) CeO_2 and Ce-ZrO_2 supports, synthesized by surfactant-assisted method, was studied and compared to conventional Ni/CeO_2, Ni/Ce-ZrO_2, and Ni/Al_2O_3. It was firstly observed that Ni/Ce-ZrO_2 (HSA) with the Ce/Zr ratio of 3/1 showed the best performance in terms of activity and stability. This catalyst presented considerably better resistance toward carbon formation than conventional Ni/CeO_2, Ni/Ce-ZrO_2, and Ni/Al_2O_3; and the minimum inlet H_2O/CH_4 ratio requirement to operate without the detectable of carbon are significantly lower. These benefits are related to the high oxygen storage capacity (OSC) of high surface area Ce-ZrO_2 support. During the reforming process, in addition to the reactions on Ni surface, the redox reactions between the absorbed CH_4 and the lattice oxygen (O_x) on CeO_2 and Ce-ZrO_2 surface also take place, which effectively prevent the formation of carbon on the surface of Ni.

The effects of possible inlet co-reactant, i.e. H_2O, H_2, CO_2, and O_2 on the conversion of CH_4 were also studied. It was found that H_2 presented positive effect on the CH_4 conversion when small amount of H_2 was introduced; nevertheless, this positive effect became less pronounced and eventually inhibited the conversion of CH_4 at high inlet H_2 concentration particularly for Ni/CeO_2 (HSA) and Ni/Ce-ZrO_2 (HSA). The dependence of H_2O on the rate was non-monotonic due to the competition of the active sites, as have also been presented by Xu [1], Xu and Froment [2,3], Elnashaie et al. [4] and Elnashaie and Elshishini [5]. Addition of CO_2 inhibited the reforming rate, whereas addition of O_2 promoted the CH_4 conversion but reduced both CO and H_2 productions.

Keywords: Methane steam reforming; Carbon formation; CeO_2; Ce-ZrO_2

1. Introduction

Methane steam reforming is a widely practiced technology to produce hydrogen or synthesis gas for utilization in chemical processes and solid oxide fuel cells (SOFCs). Three main reactions take place as in the following equations.

$$CH_4 + H_2O = CO + 3H_2 \quad (1)$$

$$CO + H_2O = CO_2 + H_2 \quad (2)$$

$$CH_4 + 2H_2O = CO_2 + 4H_2 \quad (3)$$

Both the water-gas shift reaction (Eq. (2)) and reverse methanation (Eq. (3)) are always associated with catalytic steam reforming at elevated temperatures. Due to their overall high endothermic nature, these reactions are carried out at high-temperature (700–900 °C) to achieve high conversions.

Commercial catalysts for the methane steam reforming reaction are nickel on supports, such as Al_2O_3, MgO, $MgAl_2O_4$ or their mixtures. Selection of a support material is an important issue as it has been evident that metal catalysts are not very active for the steam reforming when supported on inert oxides [6]. Various support materials have been tested, for example, α-Al_2O_3 [7], γ-Al_2O_3 and γ-Al_2O_3 with alkali metal oxide and rare earth metal oxide [8], $CaAl_2O_4$ [9] and Ce-ZrO_2 [10]. A promising catalyst system for the reforming reactions appears to be a metal on Ce-ZrO_2 support, where the metal can be Ni, Pt or Pd [11–19]. Ni/Ce-ZrO_2 has also been successfully applied to partial oxidation and autothermal reforming of methane [20].

It is well-established that cerium oxide (CeO_2) and ceria-zirconia (Ce-ZrO_2) are useful in a wide variety of applications

* Corresponding author.
E-mail address: navadol_l@jgsee.kmutt.ac.th (N. Laosiripojana).

1385-8947/$ – see front matter © 2007 Elsevier B.V. All rights reserved.
doi:10.1016/j.cej.2007.05.035

involving oxidation or partial oxidation of hydrocarbons (e.g. automotive catalysis) and as components of anodes for SOFCs. This material has high oxygen storage capacity, which is beneficial in oxidation processes and carbon combustion. The excellent resistance toward carbon formation from methane cracking reaction over CeO_2 compared to commercial Ni/Al_2O_3 was also reported recently [21]. The addition of zirconium oxide (ZrO_2) to cerium oxide (CeO_2) has been found to improve the oxygen storage capacity, redox property, thermal stability, and catalytic activity [22–31]. Nevertheless, the major limitations for applying CeO_2 and to a lesser extent Ce-ZrO_2 in high-temperature steam reforming are their low specific surface and surface area reduction due to sintering [21]. Therefore, the use of high surface area (HSA) ceria-based materials as the catalyst support would be a good alternative to improve the methane steam reforming performance. Several methods have been described recently for the preparation of high surface area (HSA) CeO_2 and Ce-ZrO_2 solid solutions. Most interest is focused on the preparation of transition-metal oxides using templating pathways [32–34]. However, only a few of these composites showed a regular pore structure after calcination [35–37]. A surfactant-assisted approach was employed to prepare high surface area CeO_2 and Ce-ZrO_2 with improved textural, structural and chemical properties for environmental applications [38]. They were prepared by reacting a cationic surfactant with a hydrous mixed oxide produced by co-precipitation under basic conditions. By this preparation procedure, materials with good homogeneity and stability especially after thermal treatments were achieved.

In the present work, high surface area (HSA) CeO_2 and Ce-ZrO_2 were synthesized by the surfactant-assisted approach. Ni was selected as a metal catalyst and impregnated on these high surface area CeO_2 and Ce-ZrO_2. It should be noted that, for Ni/Ce-ZrO_2, different ratios of Ce/Zr were firstly investigated to determine a suitable composition ratio. The stability and activity of Ni on high surface area CeO_2 and Ce-ZrO_2 were then studied and compared to Ni on low surface area CeO_2 and Ce-ZrO_2, and also conventional Ni/Al_2O_3. Furthermore, the resistance toward carbon formation and the influences of possible inlet co-reactant, i.e. H_2, H_2O, CO_2, and O_2 (as oxidative steam reforming) on the methane steam reforming over these catalysts were determined by adding and varying the partial pressures of these components at the inlet feed, as these are important issues in the industrial applications.

2. Experimental

2.1. Material preparation and characterization

Conventional Ce-ZrO_2 supports (Ce-ZrO_2 (LSA)) with different Ce/Zr molar ratios were prepared by co-precipitation of cerium chloride ($CeCl_3{\cdot}7H_2O$), and zirconium oxychloride ($ZrOCl_2{\cdot}8H_2O$) from Aldrich. The starting solution was prepared by mixing 0.1 M of metal salt solutions with 0.4 M of ammonia at a 2 to 1 volumetric ratio. This solution was stirred by magnetic stirring (100 rpm) for 3 h, then sealed and placed in a thermostatic bath maintained at 90 °C. The ratio between each metal salt was altered to achieve nominal Ce/Zr molar ratios of 1/3, 1/1 and 3/1. The precipitate was filtered and washed with deionised water and acetone to remove the free surfactant. It was dried overnight in an oven at 110 °C, and then calcined in air at 1000 °C for 6 h.

High surface area (HSA) Ce-ZrO_2 supports were prepared by the surfactant-assisted method [38]. An aqueous solution of an appropriate cationic surfactant and 0.1 M cetyltrimethylammonium bromide solution from Aldrich were added to an 0.1 M aqueous solution containing $CeCl_3{\cdot}7H_2O$ and $ZrOCl_2{\cdot}8H_2O$ in a desired molar ratio. The molar ratio of ([Ce] + [Zr])/[cetyltrimethylammonium bromide] was kept constant at 0.8. The mixture was stirred and then aqueous ammonia was slowly added with vigorous stirring. The mixture was continually stirred for 3 h, then sealed and placed in the thermostatic bath maintained at 90 °C. After that, the mixture was cooled and the resulting precipitate was filtered and washed repeatedly with water and acetone. The filtered powder was dried in the oven at 110 °C for 1 day and then calcined in air at 1000 °C for 6 h. Similarly, CeO_2 (LSA and HSA) were prepared using the same procedures as Ce-ZrO_2, but without the addition of $ZrOCl_2{\cdot}8H_2O$.

Ni/Ce-ZrO_2, Ni/CeO_2 and Ni/Al_2O_3 with 5 wt.% Ni were prepared by impregnating the respective supports with $NiCl_3$ solution at room temperature. These solutions were stirred by magnetic stirring (100 rpm) for 6 h. The solution was dried overnight in the oven at 110 °C, calcined in air at 1000 °C and reduced with 10%H_2 for 6 h. The BET measurements of all synthesized Ni/CeO_2 and Ni/Ce-ZrO_2 were then carried out in order to determine the specific surface area. These values as well as the observed pore volume and pore size of the catalysts are presented in Table 1. It can be seen that the introduction of

Table 1
Specific surface areas, pore volume, and pore size of catalysts after treatments

Catalysts	Surface area after calcination ($m^2\ g^{-1}$)	Pore volume ($cm^3\ g^{-1}$)	Pore size (Å)
Ni/Ce-ZrO_2 (HSA) (Ce/Zr = 1/3)	45	0.15	63.71
Ni/Ce-ZrO_2 (HSA) (Ce/Zr = 1/1)	44	0.14	63.90
Ni/Ce-ZrO_2 (HSA) (Ce/Zr = 3/1)	41.5	0.14	63.15
Ni/CeO_2 (HSA)	24	0.13	63.02
Ni/Ce-ZrO_2 (LSA) (Ce/Zr = 1/3)	20	0.13	63.67
Ni/Ce-ZrO_2 (LSA) (Ce/Zr = 1/1)	18	0.11	61.19
Ni/Ce-ZrO_2 (LSA) (Ce/Zr = 3/1)	19	0.11	62.42
Ni/CeO_2 (LSA)	8.5	0.08	61.20

Table 2
Physicochemical properties of the synthesized catalysts

Catalyst	Metal-load (wt.%)	Metal-reducibility (%)	Ni-dispersion (%)
Ni/Ce-ZrO_2 (HSA) (Ce/Zr = 1/3)	4.9	91.8	9.67
Ni/Ce-ZrO_2 (HSA) (Ce/Zr = 1/1)	4.9	91.0	8.82
Ni/Ce-ZrO_2 (HSA) (Ce/Zr = 3/1)	5.0	92.6	8.95
Ni/CeO_2 (HSA)	5.0	92.2	6.41
Ni/Ce-ZrO_2 (LSA) (Ce/Zr = 1/3)	4.8	90.8	4.69
Ni/Ce-ZrO_2 (LSA) (Ce/Zr = 1/1)	4.9	91.6	4.73
Ni/Ce-ZrO_2 (LSA) (Ce/Zr = 3/1)	4.9	92.1	4.68
Ni/CeO_2 (LSA)	5.0	91.3	3.12
Ni/Al_2O_3	5.0	94.5	4.85

ZrO_2 stabilizes the surface area of catalyst, which is in good agreement with the results obtained on catalysts prepared by conventional routes [21]. It should be noted that the catalysts were also characterized with several physicochemical methods after reduction. The weight content of Ni in Ni/Al_2O_3, Ni/Ce-ZrO_2 (with different Ce/Zr ratio), and Ni/CeO_2 were determined by X-ray fluorescence (XRF) analysis. The reducibility and dispersion percentages of nickel were measured from temperature programmed reduction (TPR) with 5% H_2 in Ar and temperature programmed desorption (TPD), respectively. All physicochemical properties of the synthesized catalysts are presented in Table 2.

2.2. Experimental set-up

Fig. 1 shows the schematic diagram of the experimental reactor system. It consists of three main sections: feed, reaction, and analysis sections. The main obligation of the feed section is to supply the components of interest, such as CH_4, H_2O, H_2, or O_2 to the reaction section, where an 8 mm internal diameter and 40 cm length quartz reactor was mounted vertically inside a furnace. The catalyst (with the weight of 50 mg) was loaded in the quartz reactor, which was packed with a small amount of quartz wool to prevent the catalyst from moving. Preliminary experiments were carried out to find suitable conditions in which internal and external mass transfer effects are not predominant. Considering the effect of external mass transfer, the total flow rate was kept constant at 100 $cm^3\,min^{-1}$ at a constant residence time of 5×10^{-4} g min cm^{-3} in all testing. The suitable average sizes of catalysts were also verified in order to confirm that the experiments were carried out within the region of intrinsic kinetics. In our system, a Type-K thermocouple was placed into the annular space between the reactor and furnace. This thermocouple was mounted in close contact with the catalyst bed to minimize the temperature difference. Another Type-K thermocouple, covering by closed-end quartz tube, was inserted in the middle of the quartz reactor in order to re-check the possible temperature gradient.

After the reactions, the exit gas was transferred via trace-heated lines to the analysis section, which consists of a Porapak Q column Shimadzu 14B gas chromatography (GC) and a mass spectrometer (MS). The gas chromatography was applied in order to investigate the steady state condition experiments, whereas the mass spectrometer was used for the transient carbon formation and water-gas shift reaction experiments.

2.3. Temperature programmed techniques (TP)

In the present work, temperature programmed technique (TP) was applied for studying carbon formation and water-gas shift reaction experiments. Temperature programmed methane adsorption (TPMA) was done in order to investigate the reaction of methane with the surface of catalyst. Five percent CH_4 in He with the total flow rate of 100 $cm^3\,min^{-1}$ was introduced into the system, while the operating temperature increased from room temperature to 900 °C by the rate of 10 °C min^{-1}. Then, the system was cooled down to the room temperature under helium flow. After the TPMA experiment, the carbon deposited on the catalyst was investigated by the temperature programmed oxidation (TPO). Ten percent O_2 in He with the total flow rate of 100 $cm^3\,min^{-1}$ was introduced into the system, after a He purge. Similar to TPMA, the temperature was increased from room temperature to 900 °C. The amount of carbon formation on the surface of each catalyst was then determined by measuring the CO and CO_2 yield obtained from the TPO result.

The temperature programmed reaction (TPR_x) of CO/H_2O/He gas mixture was also carried out in order to investigate the water-gas shift reaction. The mixture of 5%CO and 10%H_2O in He was introduced into the system during heating up period by the rate of 10 °C min^{-1} before reaching the isothermal condition at 900 °C.

3. Results

3.1. Selection of suitable Ce/Zr ratio for Ni/Ce-ZrO_2

Ni/Ce-ZrO_2 catalysts with different Ce/Zr ratios (1/3, 1/1, and 3/1) were firstly tested in methane steam reforming conditions at 900 °C for both HSA and LSA materials in order to select the most suitable ratio of Ce/Zr for the main studies. The results shown in Fig. 2 revealed that at steady state, the Ni/Ce-ZrO_2 with Ce/Zr ratio of 3/1 shows the best performance in terms of stability and activity for both high and low surface areas. Consequently, Ni/Ce-ZrO_2 with Ce/Zr ratio of 3/1 was selected for further investigations.

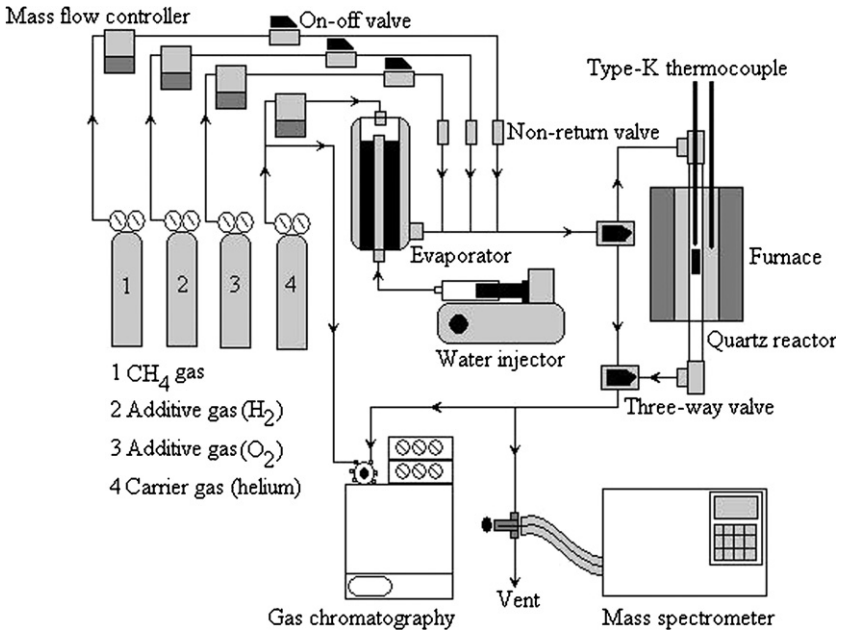

Fig. 1. Schematic diagram of the experimental set-up.

3.2. Stability and activity toward methane steam reforming

The reactivity of methane steam reforming over Ni/CeO_2 (HSA), $Ni/Ce\text{-}ZrO_2$ (HSA) with Ce/Zr ratio of 3/1, Ni/Al_2O_3, $Ni/Ce\text{-}ZrO_2$ (LSA) and Ni/CeO_2 (LSA) were then tested. The inlet components were $CH_4/H_2O/H_2$ in helium with the inlet ratio of 1.0/3.0/0.2 (with the inlet CH_4 partial pressure of 4 kPa). The main products from the reactions over these catalysts were H_2 and CO with some CO_2, indicating a contribution from the water-gas shift, and the reverse methanation at this high-temperature. The steam reforming rate was measured as a function of time in order to indicate the stability and the deactivation rate. The variations in CH_4 conversion with time for different catalysts are shown in Fig. 3. At steady state, Ni/CeO_2 (HSA) and $Ni/Ce\text{-}ZrO_2$ (HSA) presented much higher reactivity toward the methane steam reforming than Ni/Al_2O_3, $Ni/Ce\text{-}ZrO_2$ (LSA), and Ni/CeO_2 (LSA). As seen from the figure, the steam reforming activities of Ni/CeO_2 (LSA) and Ni/Al_2O_3 significantly declined with time before reaching a new steady state rate at a much lower value, while the activity of Ni/CeO_2 (HSA), $Ni/Ce\text{-}ZrO_2$ (HSA), and $Ni/Ce\text{-}ZrO_2$ (LSA) declined slightly. Catalyst stabilities expressed as a deactivation percentage are given in Table 3. In order to investigate the reason of the catalyst deactivation, the post-reaction temperature programmed oxidation (TPO) experiments were then carried out. TPO experiments detected small amount of carbon formation on the surface of Ni over ceria-based supports, whereas significant amount of carbon deposited was observed from the TPO over Ni/Al_2O_3 (1.31 mmol g_{cat}^{-1}). According to these TPO results, the deacti-

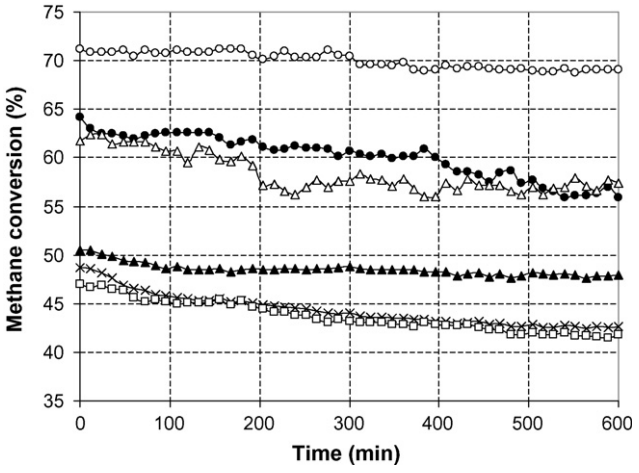

Fig. 2. Steam reforming of methane at 900 °C for $Ni/Ce\text{-}ZrO_2$ with different Ce/Zr ratios using the inlet $CH_4/H_2O/H_2$ ratio of 1.0/3.0/0.2 ($Ni/Ce\text{-}ZrO_2$ (HSA) Ce/Zr = 3/1 (◯), $Ni/Ce\text{-}ZrO_2$ (HSA) Ce/Zr = 1/1 (●), $Ni/Ce\text{-}ZrO_2$ (HSA) Ce/Zr = 1/3 (△), $Ni/Ce\text{-}ZrO_2$ (LSA) Ce/Zr = 3/1 (▲), $Ni/Ce\text{-}ZrO_2$ (LSA) Ce/Zr = 1/1 (×), and $Ni/Ce\text{-}ZrO_2$ (LSA) Ce/Zr = 1/3 (□)).

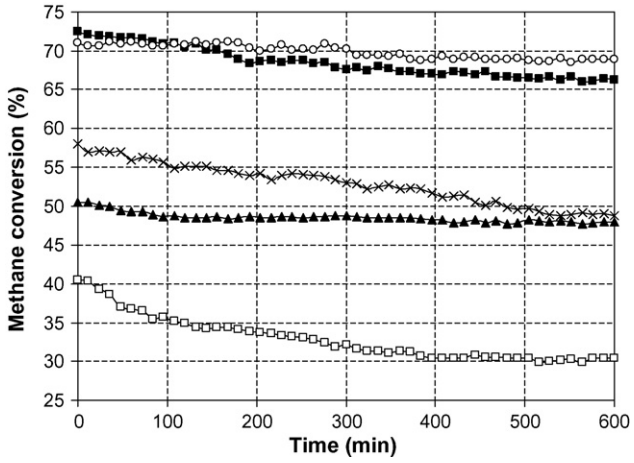

Fig. 3. Steam reforming of methane at 900 °C for different catalysts using the inlet $CH_4/H_2O/H_2$ ratio of 1.0/3.0/0.2 ($Ni/Ce\text{-}ZrO_2$ (HSA) (◯), Ni/CeO_2 (HSA) (■), Ni/Al_2O_3 (×), $Ni/Ce\text{-}ZrO_2$ (LSA) (▲), and Ni/CeO_2 (LSA) (□)).

Table 3
Physicochemical properties of the synthesized catalysts after running the reaction at 900 °C for 10 h

Catalyst	Deactivation (%)	Surface area after reaction ($m^2\ g^{-1}$)	C. formation[a] (mmol g_{cat}^{-1})	Ni-dispersion (%)
Ni/Ce-ZrO_2 (HSA) (Ce/Zr = 1/3)	7.0	42	0.08	9.62
Ni/Ce-ZrO_2 (HSA) (Ce/Zr = 1/1)	12	40	0.11	8.71
Ni/Ce-ZrO_2 (HSA) (Ce/Zr = 3/1)	3.0	40	~0	8.75
Ni/CeO_2 (HSA)	8.7	22	~0	6.33
Ni/Ce-ZrO_2 (LSA) (Ce/Zr = 1/3)	11	18	0.21	4.52
Ni/Ce-ZrO_2 (LSA) (Ce/Zr = 1/1)	12	15	0.19	4.61
Ni/Ce-ZrO_2 (LSA) (Ce/Zr = 3/1)	5.1	18	~0	4.62
Ni/CeO_2 (LSA)	24	6.2	0.14	3.06
Ni/Al_2O_3	16	40	1.31	4.81

[a] Measured from temperature programmed oxidation (TPO).

vation of Ni/Al_2O_3 during the methane steam reforming was mainly related to the carbon formation. In contrast, the deactivations of Ni/CeO_2 and Ni/Ce-ZrO_2 were not caused by the carbon formation; the BET measurement (Table 3) suggested that the deactivations of Ni/CeO_2 and Ni/Ce-ZrO_2, particularly for the low surface area supports, could be due to reduction of surface area. The lower magnitude of the reduction for Ni/CeO_2 (HSA) and Ni/Ce-ZrO_2 (HSA) than for the LSA materials indicates a higher thermal stability for CeO_2 (HSA) and Ce-ZrO_2 (HSA). It should be noted from the BET and TPO studies that although Ni/Al_2O_3 was thermally stable at high operating temperature, it was more susceptible to carbon formation which led to the catalyst deactivation.

3.3. Resistance toward carbon formation

More investigations on the resistance toward the formation of carbon species for all catalysts were investigated by Temperature programmed techniques, i.e. TPMA and TPO. In order to provide the best conditions for testing and obtain the actual resistance toward carbon formation, the influences of exposure time and methane concentration on the amount of carbon formation were firstly determined. Five percent CH_4 in He was fed to the catalyst bed at the isothermal condition (900 °C) for several exposure times (15, 30, 60, 90, 120, 150, and 180 min). The profiles of carbon formation over different catalysts with several exposure times are shown in Fig. 4. Clearly, the quantity of carbon formed on the catalyst surface increased with increasing CH_4 exposure time, and reached its maximum value after 120 min for all catalysts. The influence of inlet CH_4 concentration on the amount of carbon formation was then investigated by introducing different inlet methane partial pressures (2.0–10.0 kPa) with the constant exposure time of 120 min. The amount of carbon deposition seemed to be independent of the inlet methane partial pressure at the same operating conditions. It should be noted that although the rate of carbon formation reaction ($CH_4 \rightarrow C + H_2$) should vary with the methane partial pressure, the reaction time of 120 min may be sufficiently long enough to achieve its maximum carbon formation on the surface of each catalyst and, therefore, the influence of methane partial pressure on coke deactivation was not obviously observed. Therefore, in all experiments, TPMA was carried out by introducing 5% CH_4 in He for 120 min before investigating the degree

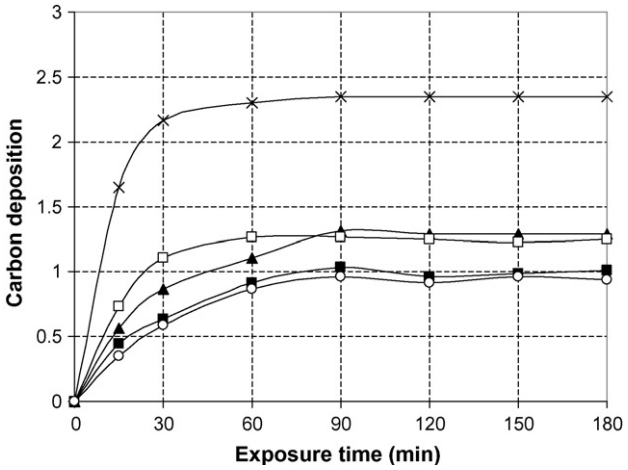

Fig. 4. Influence of exposure time on the amount of carbon formation (mmol g_{cat}^{-1}) for different catalysts at 900 °C (Ni/Ce-ZrO_2 (HSA) (◯), Ni/CeO_2 (HSA) (■), Ni/Al_2O_3 (×), Ni/Ce-ZrO_2 (LSA) (▲), and Ni/CeO_2 (LSA) (□)).

of carbon formation by TPO. Fig. 5 presents the TPMA results for Ni/Ce-ZrO_2 (LSA), Ni/CeO_2 (HSA), Ni/Ce-ZrO_2 (HSA), and Ni/Al_2O_3, while Fig. 6 presents the TPO results for those catalysts.

As seen in Fig. 5, carbon monoxide and carbon dioxide were also produced together with hydrogen for Ni catalysts on ceria-

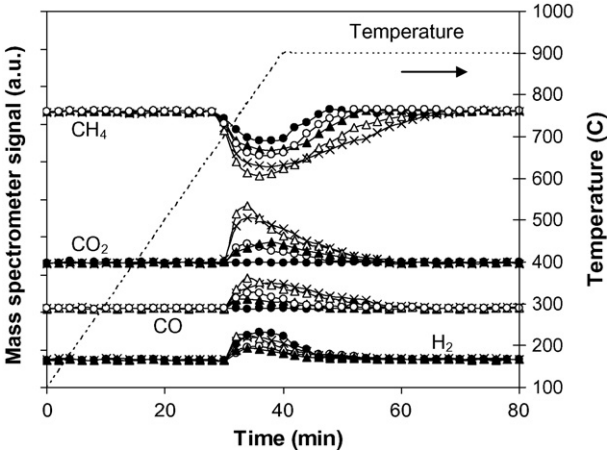

Fig. 5. TPMA over (△) Ni/CeO_2-ZrO_2 (HSA), (×) Ni/CeO_2 (HSA), (◯) Ni/CeO_2-ZrO_2 (LSA), (▲) Ni/CeO_2 (LSA), and (●) Ni/Al_2O_3.

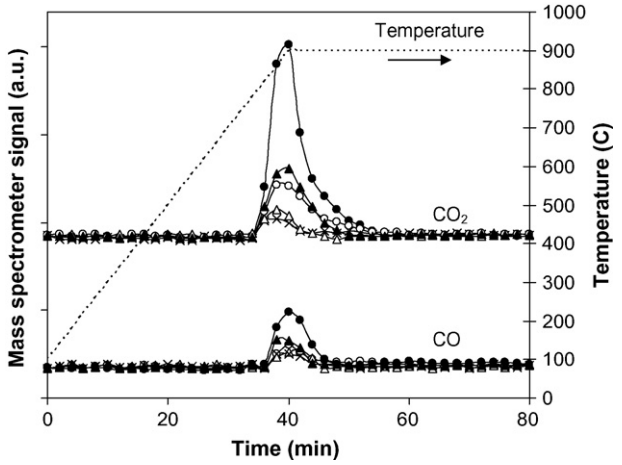

Fig. 6. Temperature programmed oxidation over (△) Ni/CeO_2-ZrO_2 (HSA), (×) Ni/CeO_2 (HSA), (◯) Ni/CeO_2-ZrO_2 (LSA), (▲) Ni/CeO_2 (LSA), and (●) Ni/Al_2O_3 following TPMA to 900 °C.

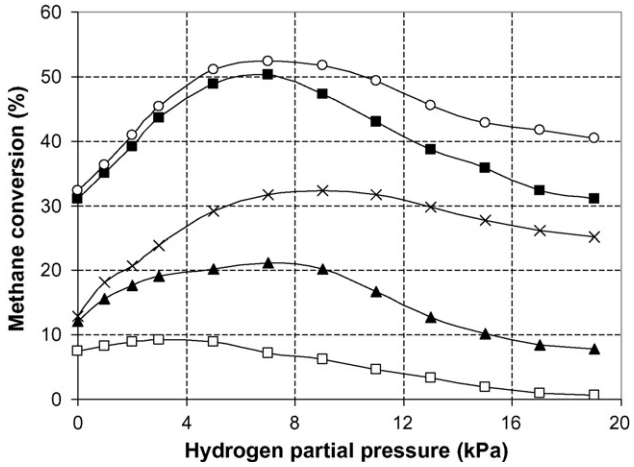

Fig. 7. Effect of hydrogen partial pressure on steam reforming rate over different catalysts at 800 °C (Ni/Ce-ZrO_2 (HSA) (◯), Ni/CeO_2 (HSA) (■), Ni/Al_2O_3 (×), Ni/Ce-ZrO_2 (LSA) (▲), and Ni/CeO_2 (LSA) (□)).

based supports, whereas only hydrogen peak was detected for TPMA over Ni/Al_2O_3. The CO and CO_2 formations from TPMA of Ni catalysts on ceria-based supports comes from the gas–solid reaction of CH_4 with the lattice oxygen (O_x) on ceria surface (Eq. (4)):

$$CH_4 + O_x = 2H_2 + CO + V_O^{\bullet\bullet} + 2e' \quad (4)$$

$V_O^{\bullet\bullet}$ denotes an oxygen vacancy with an effective charge 2^+, e' is an electron which can either be more or less localized on a cerium ion or delocalized in a conduction band. The quantities of carbon deposited (mmol g_{cat}^{-1}) on the surface of each catalyst, which could be calculated by measuring the CO and CO_2 yields, are presented in Table 4. Clearly, Ni/CeO_2 (HSA) and Ni/Ce-ZrO_2 (HSA) provided higher resistance toward carbon formation than Ni/Al_2O_3, Ni/Ce-ZrO_2 (LSA), and Ni/CeO_2 (LSA).

The influence of adding H_2O along with CH_4 at the feed on the amount of carbon formation was studied by varying the inlet H_2O/CH_4 ratio from 0.0/0.05 to 0.15/0.05. As seen in Table 4, it was observed that the carbon deposition over nickel catalyst on ceria-based supports rapidly decreased with increasing inlet steam partial pressure. Nickel catalyst on low surface area (LSA) Ce-ZrO_2 required inlet H_2O/CH_4 ratio of 3.0 in order to prevent the formation of carbon species on catalyst surface, while nickel catalyst on high surface area (HSA) Ce-ZrO_2 required inlet H_2O/CH_4 ratio as low as 1.0. It should be noted that Ni/Al_2O_3 required much higher H_2O/CH_4 ratio to reduce the carbon formation, and the carbon species remains detectable on the surface of Ni/Al_2O_3 even the inlet H_2O/CH_4 ratio is higher than 3.0.

3.4. Effect of inlet co-reactant compositions

The influences of possible co-reactant compositions, i.e. H_2, H_2O, CO_2, and O_2 on the conversion of CH_4 over these Ni catalysts were investigated. First, various inlet H_2 partial pressures were added along with CH_4 and H_2O to the feed in order to investigate the influence of this component on the CH_4 conversion. The inlet CH_4 and H_2O partial pressures were kept constant at 4.0 and 12.0 kPa, respectively. As shown in Fig. 7, with the presence of low H_2 partial pressure (0–5 kPa), H_2 presented positive effect on the CH_4 conversion. Without inlet hydrogen, the CH_4 conversions for all catalysts were apparently low, suggesting that some hydrogen must be fed together with methane and steam to obtain significant reforming rate. Similar result was earlier reported over Ni/ZrO_2 [1]. Table 5 gives the reaction orders in H_2 for all catalysts in this range of H_2 partial pressure. Compared to Ni/Al_2O_3, the reaction orders in hydrogen for Ni catalyst on ceria-based supports, especially on high surface area (HSA) supports were significantly lower. The CH_4 conversion at higher inlet H_2 partial pressures (>5 kPa) was also measured. When the inlet hydrogen partial pressure was greater than 8–10 kPa, a strong reduction in rate was observed for all catalysts, Fig. 7, as expected.

Fig. 8 shows the effect of steam on the CH_4 conversion. It was found that the conversion increased with increasing inlet H_2O partial pressure at low values but H_2O then presented a negative effect on the reforming rate at higher inlet H_2O/CH_4 ratio. It should be noted that the steam requirement for Ni/CeO_2

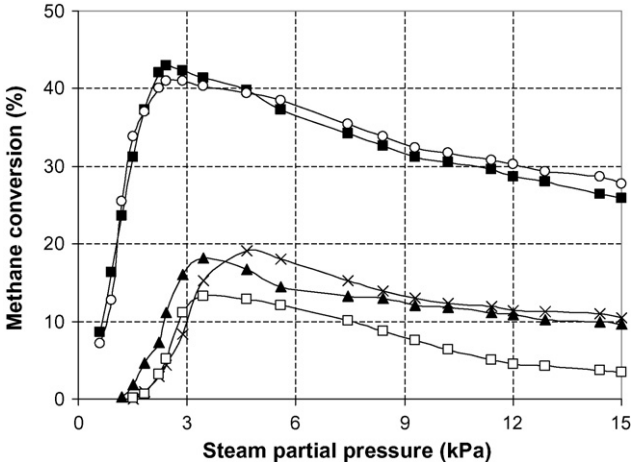

Fig. 8. Effect of steam partial pressure on steam reforming rate over different catalysts at 800 °C (Ni/Ce-ZrO_2 (HSA) (◯), Ni/CeO_2 (HSA) (■), Ni/Al_2O_3 (×), Ni/Ce-ZrO_2 (LSA) (▲), and Ni/CeO_2 (LSA) (□)).

Table 4
Dependence of inlet H_2O/CH_4 ratio on the amount of carbon formation on the catalyst surface (900 °C)

Catalysts	Amount of carbon formation at various H_2O/CH_4 ratios (mmol g_{cat}^{-1})							
	0	0.2	0.4	0.6	0.8	1.0	2.0	3.0
Ni/CeO_2 (HSA)	0.90	0.73	0.59	0.26	0.14	0.09	~0	~0
$Ni/Ce\text{-}ZrO_2$ (HSA)	1.04	0.85	0.54	0.21	0.07	~0	~0	~0
Ni/CeO_2 (LSA)	1.26	1.24	1.09	0.73	0.50	0.34	0.23	0.14
$Ni/Ce\text{-}ZrO_2$ (LSA)	1.30	1.18	0.79	0.56	0.32	0.18	0.09	~0
Ni/Al_2O_3	2.37	2.37	2.25	2.16	2.06	1.99	1.49	1.35

Table 5
Reaction orders in hydrogen from the methane steam reforming reaction at low hydrogen partial pressure (4 kPa CH_4, 12 kPa H_2O, and up to 5 kPa H_2)

Catalysts	Reaction order in hydrogen at different temperatures				
	650 °C	700 °C	750 °C	800 °C	850 °C
Ni/CeO_2 (HSA)	0.16	0.18	0.16	0.16	0.17
$Ni/Ce\text{-}ZrO_2$ (HSA)	0.17	0.18	0.19	0.16	0.17
Ni/CeO_2 (LSA)	0.17	0.18	0.19	0.18	0.17
$Ni/Ce\text{-}ZrO_2$ (LSA)	0.18	0.19	0.18	0.20	0.18
Ni/Al_2O_3	0.34	0.31	0.28	0.30	0.29

(HSA) and $Ni/Ce\text{-}ZrO_2$ (HSA) to achieve the maximum reforming reactivity were lower than the others.

The methane steam reforming in the presence of CO_2 was then investigated by adding different inlet CO_2 partial pressures (1–5 kPa) to the feed gas. Fig. 9 presents the effect of CO_2 on the reforming rate for each catalyst by plotting the relationship between $\ln(\text{Rate}_{\text{with CO}_2}/\text{Rate}_{\text{without CO}_2})$ and $\ln(P_{CO_2})$. As seen from this figure, CO_2 presented a negative effect on the CH_4 conversion for all catalysts; however, in contrast to the influence of H_2, the weaker inhibition effect by CO_2 was observed for Ni on ceria-based supports. According to the reaction order in CO_2 calculation, the reaction order in CO_2 for Ni/Al_2O_3 was approximately −0.12, whereas those over Ni on ceria-based supports were around −0.06 to −0.03, which clearly indicated the weaker inhibitory effect of CO_2 for Ni on ceria-based supports.

Finally, the methane steam reforming in the presence of O_2 (as autothermal reforming) was then carried out by adding different O_2 partial pressures (1–4 kPa) into the feed gas at several operating temperatures. The rate increased with increasing the inlet oxygen partial pressure for all catalysts as shown in Fig. 10. However, H_2 and $CO/(CO+CO_2)$ production selectivity were found to decrease with increasing O_2 concentration as shown in Fig. 11 for Ni/Al_2O_3, $Ni/Ce\text{-}ZrO_2$ (LSA), and Ni/CeO_2 (LSA) and Fig. 12 for $Ni/Ce\text{-}ZrO_2$ (HSA) and Ni/CeO_2 (HSA), respectively. It should be noted that, at the same operating conditions, the $CO/(CO+CO_2)$ production selectivity for Ni/Al_2O_3 was observed to be higher than that over Ni on ceria-based supports. The difference in this production selectivity is due to the reactivity toward the water-gas shift reaction of each support. The water-gas shift reaction (WGS) activities of each support was also carried out in the present work to ensure the influence of this reaction on the $CO/(CO+CO_2)$ selectivity. Fig. 13 shows the activities of all supports toward this reaction at several tem-

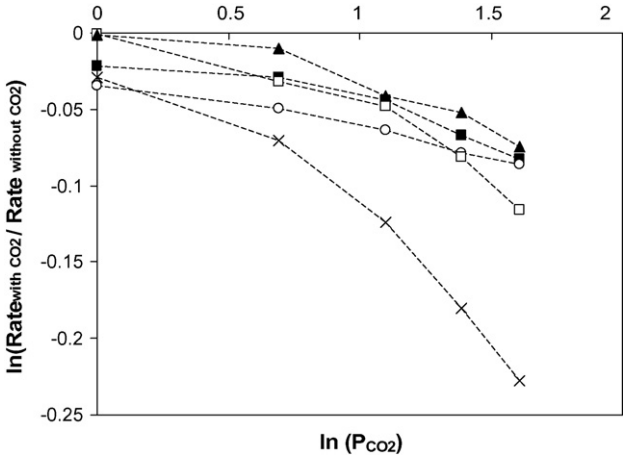

Fig. 9. Effect of carbon dioxide partial pressure on steam reforming rate over different catalysts at 800 °C ($Ni/Ce\text{-}ZrO_2$ (HSA) (◯), Ni/CeO_2 (HSA) (■), Ni/Al_2O_3 (×), $Ni/Ce\text{-}ZrO_2$ (LSA) (▲), and Ni/CeO_2 (LSA) (□)).

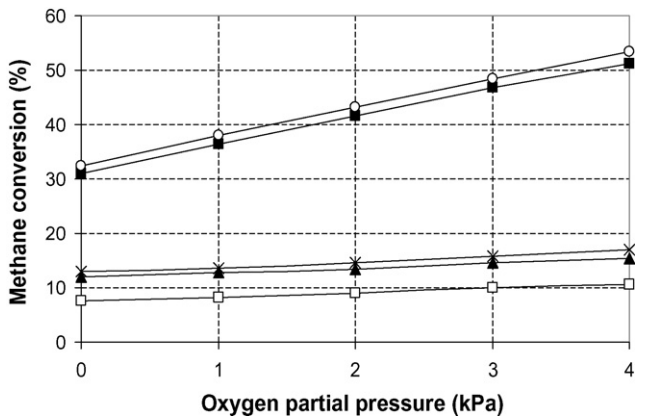

Fig. 10. Effect of oxygen partial pressure on steam reforming rate over different catalysts at 800 °C ($Ni/Ce\text{-}ZrO_2$ (HSA) (◯), Ni/CeO_2 (HSA) (■), Ni/Al_2O_3 (×), $Ni/Ce\text{-}ZrO_2$ (LSA) (▲), and Ni/CeO_2 (LSA) (□)).

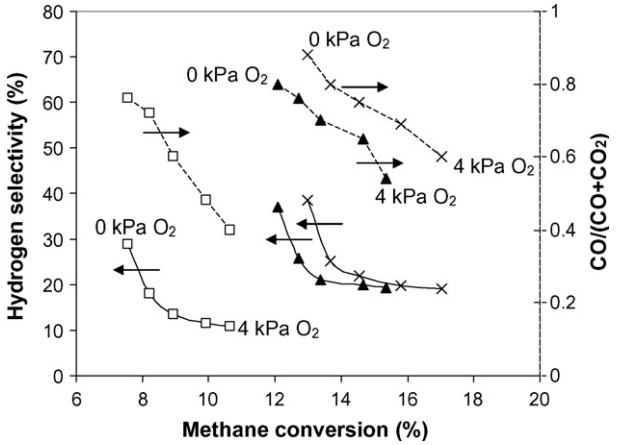

Fig. 11. Effect of oxygen partial pressure on the H_2 selectivity (solid lines) and $CO/(CO+CO_2)$ (dot lines) at isoconversion from steam reforming over Ni/Al_2O_3 (×), $Ni/Ce\text{-}ZrO_2$ (LSA) (▲), and Ni/CeO_2 (LSA) (□) at 800 °C.

peratures. Among the supports, the activity toward this reaction over CeO_2 (HSA) was the highest.

4. Discussion

Improvements of stability and activity toward methane steam reforming were achieved for Ni on high surface area (HSA) ceria-based supports. The high stability is due to the lower sintering rate compared to Ni on low surface area (HSA) ceria-based supports and the higher resistance toward carbon deposition compared to Ni/Al_2O_3, while the high reforming activity is possibly due to the improvement of Ni-dispersion on the high surface area support (Table 2), and also the strong gas–solid redox reaction between methane and the high surface area (HSA) ceria-based supports. It has been reported that the solid–gas reaction between CeO_2 and CH_4 produces synthesis gas with a H_2/CO ratio of two (Eq. (4)), while the reduced ceria can react with CO_2 and H_2O to recover CeO_2 and also produce CO and H_2 (Eqs. (5) and (6)) [39–41]. Importantly, we reported in our previous work that these redox reactions (Eqs. (4)–(6))

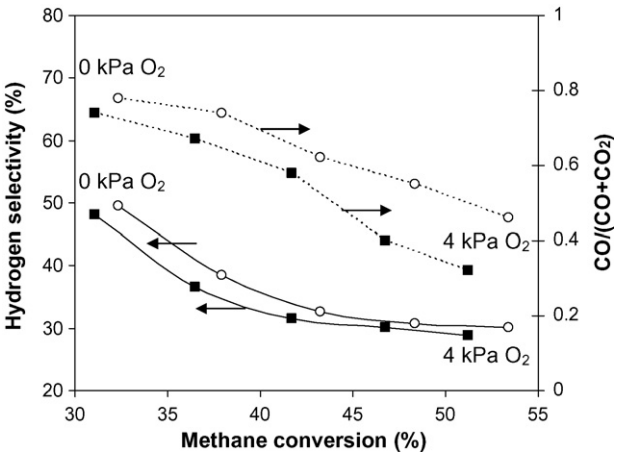

Fig. 12. Effect of oxygen partial pressure on the H_2 selectivity (solid lines) and $CO/(CO+CO_2)$ (dot lines) at isoconversion from steam reforming over $Ni/Ce\text{-}ZrO_2$ (HSA) (◯), and Ni/CeO_2 (HSA) (■) at 800 °C.

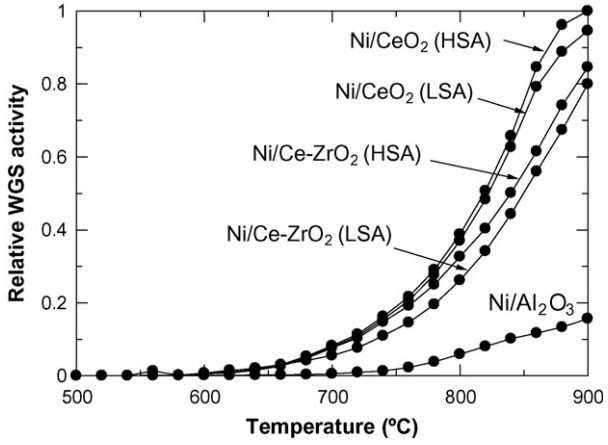

Fig. 13. The activities of each catalyst toward the water-gas shift reaction.

increase with increasing the specific active surface area of CeO_2 [42].

$$V_{O}^{\bullet\bullet} + 2e' + CO_2 = O_x + CO \quad (5)$$

$$V_{O}^{\bullet\bullet} + 2e' + H_2O = O_x + H_2 \quad (6)$$

The addition of suitable ratio of ZrO_2 over ceria, as $Ce\text{-}ZrO_2$, has also been widely reported to improve the oxygen storage capacity, and the redox reactivity of material [22–31]. These benefits were associated with enhanced reducibility of cerium (IV) in $Ce\text{-}ZrO_2$, which is a consequence of high O^{2-} mobility inside the fluorite lattice. The reason for the increasing mobility might be related to the lattice strain, which is generated by the introduction of a smaller isovalent Zr cation into the CeO_2 lattice (Zr^{4+} has a crystal ionic radius of 0.84 Å, which is smaller than 0.97 Å for Ce^{4+} in the same co-ordination environment).

The high resistance toward carbon deposition, which was observed from the catalyst over high surface area ceria-based supports, is also related to the facile redox reaction. During the steam reforming of methane, the following reactions are theoretically the most probable reactions that could lead to surface carbon formation:

$$2CO = CO_2 + C \quad (7)$$

$$CH_4 = 2H_2 + C \quad (8)$$

$$CO + H_2 = H_2O + C \quad (9)$$

$$CO_2 + 2H_2 = 2H_2O + C \quad (10)$$

Reactions (9)–(10) are favorable at low-temperatures, whereas the Boudouard reaction (Eq. (7)) and the decomposition of methane (Eq. (8)) are the major pathways for carbon formation at high-temperatures as they show the largest change in Gibbs energy. According to the range of temperature in this study, carbon formation would be formed via the decomposition of methane and Boudouard reactions. By applying ceria-based supports, the formation of carbon species via both reactions could be inhibited by the redox reactions with the lattice oxygen (O_x) forming H_2 and CO_2, which is thermodynamically unfavored to form carbon species in this range of conditions.

Therefore, significant lower amount of carbon deposition were consequently observed even at low inlet H_2O/CH_4 ratio.

The experiments on the effect of co-reactants yielded non-linear positive hydrogen trend. The positive effect at the low hydrogen appearance could be due to the reduction of oxidized state on the surface active site of nickel, while the inhibitory effect at high hydrogen partial pressure is due to the reverse methane steam reforming methanation, and the reverse water-gas shift reactions [1–3]. In addition, the presence of hydrogen atom on some active sites of nickel particle could also lead to the decrease in methane conversion [1–3]. Regarding the observed reaction order in hydrogen, the inhibitory impact for Ni catalysts on ceria-based supports (both HSA and LSA) is stronger than that for Ni/Al_2O_3 due to the redox property of the ceria-based materials. As described earlier, the gas-solid reaction between the ceria-based materials and CH_4 can generate CO and H_2, while the reduced state can react with steam and CO_2 to produce H_2 and CO, respectively. For $Ni/Ce\text{-}ZrO_2$ and Ni/CeO_2, although hydrogen prevents the oxidized state of nickel, this component can also reduce ceria via the reverse of Eq. (6) and consequently results in the inhibition of methane conversion via Eq. (4). This explanation is in good agreement with the previous studies [43] which investigated kinetics parameters for the methane steam reforming on ceria-based materials and reported the negative effect of hydrogen on methane conversion over these materials due to the change of Ce^{4+} to Ce^{3+}.

The dependence of H_2O on the CH_4 conversion is non-monotonic due to adsorption competition between CH_4 and H_2O on the catalyst active sites. Previous works [4,5] also reported the same results and explanation. The CH_4 conversion increased with increasing the inlet O_2 partial pressure. However, the $CO/(CO + CO_2)$ production selectivity and H_2 production rates strongly decreased with increasing O_2 partial pressure. This could be due to the combustion of H_2 and CO productions and the inhibition of H_2O adsorption on the catalyst surface active sites by O_2.

5. Conclusion

High surface area CeO_2 and $Ce\text{-}ZrO_2$ with Ce/Zr ratio of 3/1 are the good candidates to be used as the support for Ni catalysts for the steam reforming of CH_4 producing H_2 for later utilization in SOFC. The great advantages of Ni on high surface area (HSA) ceria-based supports are the high reforming reactivity, and also the high stability due to their excellent resistance toward carbon formation. Lower inlet H_2O/CH_4 ratio is required for Ni on high surface area (HSA) CeO_2 and $Ce\text{-}ZrO_2$ to prevent the carbon formation.

According to the effect of co-reactants (i.e. H_2O, H_2, CO_2, and O_2), the effects of H_2O on the methane steam reforming over Ni/CeO_2 (HSA) and $Ni/Ce\text{-}ZrO_2$ (HSA) are similar to those for Ni/Al_2O_3 in terms of reaction orders, whereas a stronger negative effect of H_2 was observed over Ni/CeO_2 (HSA) and $Ni/Ce\text{-}ZrO_2$ (HSA) as H_2 inhibits the gas-solid reaction between CeO_2 and CH_4. Additional of CO_2 inhibited the reforming rate, whereas addition of O_2 promoted the CH_4 conversion but reduced both CO and H_2 productions due to the further combustion and/or the inhibition of H_2O adsorption on the catalyst surface active sites. Lastly, the difference between Ni/CeO_2 (HSA) and $Ni/Ce\text{-}ZrO_2$ (HSA) is the $CO/(CO + CO_2)$ production selectivity. This selectivity for $Ni/Ce\text{-}ZrO_2$ is higher than that for Ni/CeO_2 due to the high reactivity toward water-gas shift reaction of CeO_2 compared to $Ce\text{-}ZrO_2$.

Acknowledgement

The financial support from The Thailand Research Fund (TRF) throughout this project is gratefully acknowledged.

References

[1] J. Xu, Ph.D. Thesis, Laboratorium Voor Petrochemische Techniek, Rijkuniversiteit, Gent, Belgium, 1986.
[2] J. Xu, G.F. Froment, AIChE 35 (1989) 88.
[3] J. Xu, G.F. Froment, AIChE 35 (1989) 97.
[4] S.S.E.H. Elnashaie, A.M. Adris, A.S. Al-Ubaid, M.A. Soliman, Chem. Eng. Sci. 45 (1990) 491.
[5] S.S.E.H. Elnashaie, S.S. Elshishini, Modeling, Simulation and Optimization of Industrial Fixed Bed Catalytic Reactors, Gordon and Breach Science Publishers, UK, 1993.
[6] X. Wang, R.J. Gorte, Appl. Catal. A 224 (2002) 209–218.
[7] H.S. Roh, K.W. Jun, W.S. Dong, J.S. Chang, S.E. Park, Y.I. Joe, J. Mol. Catal. A 181 (2002) 137–142.
[8] Q. Miao, G. Xiong, S. Sheng, W. Cui, L. Xu, L.X. Guo, Appl. Catal. A 154 (1987) 17–27.
[9] A.A. Lemonidou, M.A. Goula, I.A. Vasalos, Catal. Today 46 (1987) 175–183.
[10] W.S. Dong, H.S. Roh, K.W. Jun, S.E. Park, Y.S. Oh, Appl. Catal. A 226 (2002) 63–72.
[11] M. Mamak, N. Coombs, G. Ozin, Adv. Mater. 12 (2000) 198–202.
[12] M. Mamak, N. Coombs, G. Ozin, J. Am. Chem. Soc. 122 (2000) 8932.
[13] M. Mamak, N. Coombs, G.A. Ozin, Chem. Mater. 13 (2001) 3564.
[14] P. Bera, S. Mitra, S. Sampath, M.S. Hegde, Chem. Commun. (2001) 927.
[15] A. Martinez-Arias, J.M. Coronado, R. Cataluna, J.C. Conesa, J.C. Soria, J. Phys. Chem. B 102 (1998) 4357.
[16] D. Skarmoutsos, F. Tietz, P. Nikolopoulos, Fuel Cells 1 (2001) 243.
[17] T. Takeguchi, S.N. Furukawa, M. Inoue, J. Catal. 202 (2001) 14.
[18] J. Sfeir, P.A. Philippe, P. Moseki, N. Xanthopoulos, R. Vasquez, J.M. Hans, V.H. Jan, K.R. Thampi, J. Catal. 202 (2001) 229.
[19] N. Kiratzis, P. Holtappels, C.E. Hatchwell, M. Mogensen, J.T.S. Irvine, Fuel Cells 1 (2001) 211.
[20] H.S. Roh, W.S. Dong, K.W. Jun, S.E. Park, Chem. Lett. 88 (2001).
[21] P. Aguiar, E. Ramírez-Cabrera, N. Laosiripojana, A. Atkinson, L.S. Kershenbaum, D. Chadwick, Stud. Surf. Sci. Catal. 145 (2002) 387–390.
[22] M. Ozawa, M. Kimura, A. Isogai, J. Alloys Comp. 193 (1993) 73.
[23] G. Balducci, J. Kaspar, P. Fornasiero, M. Graziani, M.S. Islam, J. Phys. Chem. B 102 (1998) 557.
[24] G. Vlaic, P. Fornasiero, S. Geremia, J. Kaspar, M. Graziani, J. Catal. 168 (1997) 386.
[25] G.R. Rao, J. Kaspar, S. Meriani, R. Dimonte, M. Graziani, Catal. Lett. 24 (1994) 107.
[26] P. Fornasiero, R. Dimonte, G.R. Rao, J. Kaspar, S. Meriani, A. Trovarelli, M. Graziani, J. Catal. 151 (1995) 168.
[27] M. Haneda, K. Miki, N. Kakuta, A. Ueno, S. Tani, S. Matsura, M. Sato, Nihon Kagaku Kaishi (1990) 820.
[28] T. Ohata, Rare Earths 17 (1990) 37.
[29] J.G. Nunan, W.B. Williamson, H.J. Robota, SAE Paper 960768 (1996).
[30] S. Otsuka-Yao, H. Morikawa, N. Izu, K. Okuda, J. Jpn. Inst. Metals 59 (1995) 1237.
[31] M.H. Yao, T.E. Hoost, R.J. Baird, F.W. Kunz, J. Catal. 166 (1997) 67.
[32] C.T. Kresge, M.E. Leonowicz, W.J. Roth, J.C. Vartuli, J.S. Beck, Nature 359 (1992) 710.

[33] Q. Huo, D.I. Margolese, U. Ciesla, P. Feng, T.E. Gier, P. Sieger, R. Leon, P.M. Petroff, B. Schüth, G.D. Stucky, Nature 368 (1994) 317.
[34] P.T. Tanev, T.J. Pinnavaia, Science 267 (1995) 865.
[35] U. Ciesla, S. Schacht, G.D. Stucky, K.K. Unger, F. Schüth, Angew. Chem. Int. Ed. Engl. 35 (1996) 541.
[36] D.M. Antonelli, J.Y. Ying, Angew. Chem. Int. Ed. Engl. 35 (1996) 426.
[37] Q. Huo, D.I. Margolese, U. Ciesla, D.G. Demuth, P. Feng, T.E. Gier, P. Sieger, A. Firouzi, B.F. Chmelka, B. Schüth, G.D. Stucky, Chem. Mater. 6 (1994) 1176.
[38] Daniela Terribile, Alessandro Trovarelli, Jordi Llorca, Carla de Leitenburg and Giuliano Dolcetti, Catal. Today 43 (1998) 79–88.
[39] K. Otsuka, T. Ushiyama, I. Yamanaka, Chem. Lett. (1993) 1517.
[40] K. Otsuka, M. Hatano, A. Morikawa, J. Catal. 79 (1983) 493.
[41] K. Otsuka, M. Hatano, A. Morikawa, Inorg. Chim. Acta 109 (1985) 193.
[42] N. Laosiripojana, S. Assabumrungrat, Appl. Catal. B: Environ. 60 (2005) 107.
[43] E. Ramirez, A. Atkinson, D. Chadwick, Appl. Catal. B 36 (2002) 193–206.

Korean J. Chem. Eng., **25**(2), 223-230 (2008)

High temperature desulfurization over nano-scale high surface area ceria for application in SOFC

Rajesh Shivanahalli Kempegowda, Navadol Laosiripojana† and Suttichai Assabumrungrat*

The Joint Graduate School of Energy and Environment, King Mongkut's University of Technology Thonburi, Bangkok 10140, Thailand
*Center of Excellence in Catalysis and Catalytic Reaction Engineering, Department of Chemical Engineering, Faculty of Engineering, Chulalongkorn University, Bangkok 10330, Thailand
(*Received 13 February 2007 • accepted 27 July 2007*)

Abstract−In the present work, suitable absorbent material for high temperature desulfurization was investigated in order to apply internally in solid oxide fuel cells (SOFC). It was found that nano-scale high surface area CeO_2 has useful desulfurization activity and enables efficient removal of H_2S from feed gas between 500 to 850 °C. In this range of temperature, compared to the conventional low surface area CeO_2, 80-85% of H_2S was removed by nano-scale high surface area CeO_2, whereas only 30-32% of H_2S was removed by conventional low surface area CeO_2. According to the XRD studies, the product formed after desulfurization over nano-scale high surface area CeO_2 was Ce_2O_2S. EDS mapping also suggested the uniform distribution of sulfur on the surface of CeO_2. Regeneration experiments were then conducted by temperature programmed oxidation (TPO) experiment. Ce_2O_2S can be recovered to CeO_2 after exposure in the oxidation condition at temperature above 600 °C. It should be noted that SO_2 is the product from this regeneration process. According to the SEM/EDS and XRD measurements, all Ce_2O_2S forming is converted to CeO_2 after oxidative regeneration. As the final step, a deactivation model considering the concentration and temperature dependencies on the desulfurization activity of CeO_2 was applied and the experimental results were fitted in this model for later application in the SOFC model.

Key words: Desulfurization, SOFC, CeO_2, Deactivation Model

INTRODUCTION

Due to the present oil crisis and global warming, numerous efforts have been focused on the use of alternative and renewable energy sources. Biogas is one important energy source due to its closed cycle operation and producibility from biodegradable solid wastes such as cattle dung (diary wastes), piggery wastes, municipal solid wastes, and industrial effluents. Currently, there are numerous attempts to use biogas as a primary fuel for electrical generation by using several energy devices, i.e., internal combustion engines and fuel cells. As biogas always contains high concentration of hydrogen sulfide (H_2S) (approximately 1,000-2,000 ppm depending on its source), it cannot be utilized directly to the energy devices. Biogas must be initially purified in order to remove H_2S which easily poisons the process reactor. In addition, the removal of H_2S would also help in preventing odors, safety hazards, and corrosion of the biogas transport equipment.

The appropriate technologies of desulfurization depend on the final applications as well as the operating conditions. Several researchers have studied desulfurization by selective oxidation of H_2S over solid absorbents at low temperature (200-300 °C). Park et al. [1] investigated this reaction over $Bi_4V_{2-x}Sb_xO_{11-y}$ material and reported good H_2S conversion with less than 2% of SO_2 selectivity in the temperature range of 220-260 °C. Lee et al. [2] also studied this desulfurization reaction on zeolite-NaX and zeolite-KX. They found that Zeolite-KX was superior to the zeolite-NaX in terms of selectivity to elemental sulfur and resistance to deactivation. In detail, elemental sulfur yield over zeolite-NaX was achieved at about 90% at 225 °C for the first 4 hours, but gradually decreased to 55% after 40 hours, whereas the yield of elemental sulfur on zeolite-KX was obtained within the range of 86% at 250 °C after 40 hours.

It should be noted that selective oxidation may not suitable for high temperature applications such as coal or residual oil gasification, and fuel cell applications, which operate in the temperature range of 400-1,200 °C, due to the large temperature differences in the process. Several high temperature desulfurization techniques are, therefore, desired for use in such applications [3]. Previously, the high temperature removal of hydrogen sulfide from simulated gas was carried out in batch type fluidized-bed reactor by using natural manganese ore consisting of several metal oxides (MnO_x: 51.85%, FeO_y: 3.86%, CaO: 0.11%) [4]. It was found that H_2S removal efficiency increased with increasing temperature but decreased with increasing excess gas velocity. In addition, the breakthrough time for H_2S decreased as the gas velocity increased.

As another example of the high temperature application, fuel cell has drawn a great interest from many researchers as it can generate electricity at high efficiency. Various types of fuel cells are available, in that the solid oxide fuel cell (SOFC) has garnered much attention because of its large electricity production capacity. To establish these highly efficient processes, it is necessary to develop a high temperature treatment process for the various feed stocks, i.e., biogas and natural gas, which consist of a significant amount of H_2S. To date, fuel cell systems rely mainly on batch operation of sorbent

†To whom correspondence should be addressed.
E-mail: navadol_l@jgsee.kmutt.ac.th

technology for sulfur removal. Although this technology possesses the necessary removal efficiency, the low capacity associated with the batchwise operation and the potential utilization of high sulfur hydrocarbon feed stocks greatly affect the fuel cell processor foot print, types of sorbent and sorbent maintenance interval [5]. A widely established metal oxide, ZnO, has been used as a high temperature desulfurization sorbent. ZnO has the most favorable thermodynamics for H_2S removal among sorbents that have been investigated. However, despite its attractive thermodynamic properties, the reduction of ZnO and subsequent vaporization of elemental zinc create a serious problem over many cycles of sulfidation/regeneration at high temperatures [6,7]. As a result, alternate absorbents to minimize ZnO problems at high temperature ranges are needed.

Meng et al. [8] and Kay et al. [9] first described the use of cerium oxide (or ceria) sorbents for high-temperature desulfurization. It is well established that ceria and metal oxide (e.g., Gd, Nb, and Zr) doped cerias provide high oxygen storage capacity, which is beneficial in oxidation processes. Several researchers have also reported the benefit of adding or doping this material on the reforming and partial oxidation catalysts in terms of catalyst stability and the resistance toward carbon deposition [10,11]. Focusing on the use of ceria as the sorbent for desulfurization, in laboratory-scaled fixed-bed reactor tests, the H_2S concentration was reduced from 1.2 v% to 3 ppmv at 872 °C and 1 atm by using reduced ceria, CeO_n ($n<2$). However, only a few data were reported particularly on the material characterization and the mechanism of desulfurization. Abbasian et al. [12] and Li et al. [13] studied mixed-oxide sorbents containing cerium and copper oxides. Although some evidence of cerium sulfidation was reported, the primary function of the ceria was considered to be for maintaining the active copper in a highly dispersed form. Zeng et al. [14] studied the H_2S removal in presence of hydrogen on CeO_2 sorbent. They reported complete conversion of CeO_2 to CeO_2S during sulfidation in the temperature range of 500-700 °C and regeneration of Ce_2O_2S to CeO_2 by using SO_2. According to phase diagrams, relevant reactions were reported by Kay et al. [9] as:

Sulfidation

$$2CeO_2+H_2S+H_2 \leftrightarrow Ce_2O_2S+2H_2O \quad (1)$$

Regeneration

$$Ce_2O_2S+SO_2 \leftrightarrow 2CeO_2+S_2 \quad (2)$$

It should be noted that the major limitations to apply CeO_2 in the high temperature process are its low specific surface and high surface area reduction percentage due to the high surface sintering. It was observed from our previous work that the surface area reduction of CeO_2 after exposure in the reaction conditions at 900 °C was 23% and 28%, respectively. The corresponding post-reaction specific surface areas were only 1.9 and 8.7 $m^2\ g^{-1}$, respectively [15]. The use of high surface area CeO_2 would be a good alternative procedure to improve the performance of H_2S removal at high temperature. In this paper, nano-scale high surface area CeO_2 (from nano-Arc Company, US) was used as a sorbent for the desulfurization process. The reactions during sulfidation and oxidative regeneration were investigated. Some analytical techniques were employed to characterize the sorbents at different stages of operation. In addition, the deactivation model considering the concentration dependency of the activity was developed and fitted with the experimental results to determine the kinetic parameters for the later application in SOFC model fueled by conventional fuel: biogas and natural gas. Regarding the selection of the suitable model, it should be noted that the formation of a dense product layer over the solid reactant results in an additional diffusion resistance and is expected to cause a drop in the reaction rate. One would also expect it to cause significant changes in the pore structure, active surface area, and activity per unit area of solid reactant with reaction extent. These changes cause a decrease of the solid reactant activity with time. As reported in the literature, the deactivation model works well for such gas-solid reactions [16]. In this model, the effects of these factors on the diminishing rate of sulfur fixation were combined in a deactivation rate term [17].

EXPERIMENTAL

1. Fixed Bed Reactor Setup

A laboratory-scaled fixed bed quartz reactor of 30 cm height and 0.635 cm internal diameter was installed vertically in an electric furnace with a programmable temperature controller. Nano-scale CeO_2 (from nano-Arc Company, US) was first calcined at 900 °C before packing between two layers of quartz wool. The physical and chemical properties of CeO_2 are provided in Table 1. A type K thermocouple was located externally at the center of the catalyst to monitor the temperature of the reactor. Swagelok fittings and tubing were used to connect the reactor to the gas supply and gas sampling systems. Details of the reactor setup were shown in Fig. 1.

2. Analytical Methods

Pure CeO_2 and spent CeO_2 were characterized by using X-ray diffractometer (XRD) employing Cu 30 kW and 15 mA to determine the sulfur deposition on the sorbent. SEM and EDS analysis was also carried out to investigate the changes in morphology and sulfur distribution by elemental mapping. The conditions used were 40 kV and resolution of 4000.

Table 1. Physical and chemical properties of CeO_2

Surface area (m^2g^{-1})	42.819
Bulk density	9.102
Pore volume	9.7443×10^{-2}

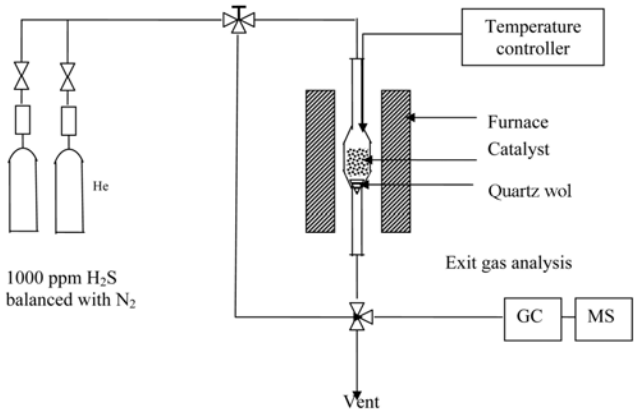

Fig. 1. Schematic diagram of experimental setup.

Table 2. Operating conditions of GC

Detector	TCD
Detector temperature (°C)	150
Column	Porapak-Q
Oven temperature (°C)	Linear programming @ 20 °C min^{-1}
Current (mA)	150

3. Gas Analysis

Gas analysis was carried out by using Shimadzu gas chromatography (GC-14B) equipped with a Porapak-Q column and a TCD detector. The H_2S peak was obtained by using a linear temperature programming in the column oven. The temperature was increased from 40 to 200 °C at a ramp rate of 20 °C min^{-1}. The operating conditions of the GC are summarized in Table 2. It should be noted that the TCD calibration was carried out by mixing pure H_2S and N_2 at various ratios. Mixture of 0.01% (molar) H_2S balanced with nitrogen was used to calibrate the concentration by diluting with helium gas.

4. Procedures for Sulfidation Experiments

The sulfidation experiments were carried out in a fixed bed reactor. The experimental procedures were divided into the study of optimum temperature and the establishment of breakthrough curves for the adsorption of H_2S on CeO_2 sorbent.

Regarding the study of optimum temperature, a set of experiments was carried out to test the desulfurization activity of CeO_2 sorbent at various temperatures: 400, 500, 600, 700, 800 and 850 °C. The amount of CeO_2 was kept at 500 mg, while the total flow rate was 100 cm^3 min^{-1}. The temperature was increased linearly at a rate of 10 °C min^{-1} until reaching a desired temperature. The reactor was then kept under isothermal condition for 30 min. The exit gases from the reactor were connected to the gas chromatography (GC) equipped with TCD detector to detect the H_2S level after adsorption at each temperature level. The breakthrough curve experiments were then carried out at the suitable temperatures for the desulfurization. The reactor was operated by using a feed gas (100 cm^3 min^{-1}) with H_2S concentration of 1,000 ppm. The reactor was heated to a desired temperature at a heating rate of 10 °C min^{-1}. The system was operated under isothermal until breakthrough of H_2S appeared at the exit of the bed.

5. Oxidative Regeneration of Sulfided CeO_2 by Temperature Programmed Reaction Study

The characteristics of the regeneration of the sulfided CeO_2 were examined with a temperature programmed oxidation (TPO) apparatus equipped with quadrupole mass spectrometer. In the TPO examination, 10% oxygen balanced in helium or nitrogen was fed into the microreactor in the TPO apparatus at a flow rate of 100 cm^3 min^{-1}. A sample of 50 mg was packed into the micro reactor of ¼" size. The sample was heated to 900 °C at a constant heating rate of 10 °C min^{-1}. The exit gases were monitored continuously with the mass spectrometer.

RESULTS AND DISCUSSION

1. Sulfidation Results

First, the effect of temperature on the desulfurization activity of nano-scale CeO_2 sorbent was studied in the range of 400 to 850 °C.

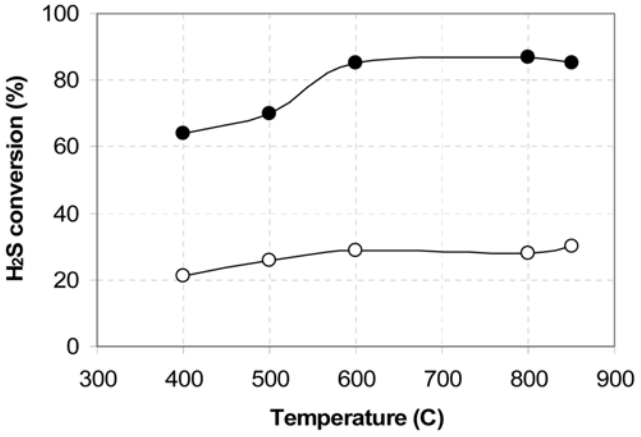

Fig. 2. Conversions of H_2S at different temperatures (nano-scale high surface area CeO_2 (●), and conventional low surface area CeO_2 (○)).

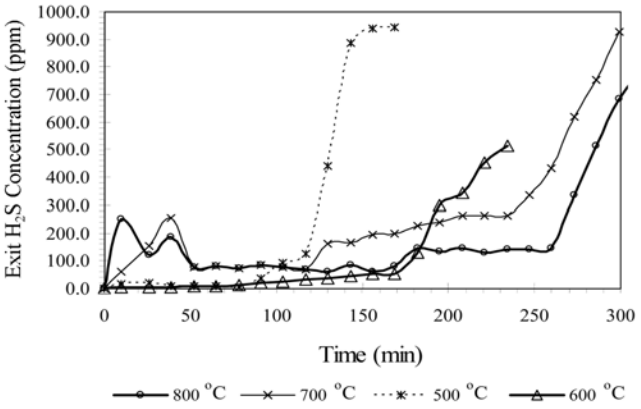

Fig. 3. Sulfidation break through curves of CeO_2.

The conversion of H_2S (X) defined in Eq. (3) was plotted with temperature as shown in Fig. 2. It should be noted that the desulfurization activity of conventional low surface area CeO_2 (synthesized by the precipitation method with the specific surface area of 3.1 m^2 g^{-1}) was also performed for comparison.

$$X = \frac{Conc_{Initial} - Conc_{Exit}}{Conc_{Initial}} \times 100 \quad (3)$$

It was found that the H_2S conversion from the desulfurization over nano-scale CeO_2 was almost 3 times higher than that over conventional low surface area CeO_2. The conversion increased readily with increasing temperature and then became constant at above 600 °C. The breakthrough results for nano-scale CeO_2, which refers to a predetermined H_2S outlet condition when a certain concentration of H_2S cannot be removed by the catalyst bed [18], at several temperatures are presented in Fig. 3. As seen from the figure, the breakthrough period increased with increasing temperature. It should be noted that a few bumps (higher H_2S concentration regions) appeared in some early part of the pre-breakthrough curves. These early bumps could be associated with incomplete reduction of ceria at the early state. Without pre-reduction, the reduction and sulfidation occurred simultaneously on the surface of ceria, as explained by Zeng et al.

[14]. According to the gas product detected from gas chromatography during the sulfidation testing, small amounts of hydrogen and oxygen were also detected along with steam, which could have been formed by the combustion of hydrogen and oxygen.

2. Regeneration of Sulfided CeO_2

Regeneration of sulfided CeO_2 was conducted by using 10% oxygen as a regeneration agent for two different samples sulfided at 700 and 800 °C. A sample was packed and heated in a micro tube reactor installed in the furnace at a constant heating rate of 10 °C min^{-1}. The amount of O_2 and SO_2 evolved at each temperature level was monitored by mass spectrometer. Figs. 4 and 5 show the results of the samples sulfided at 700 and 800 °C, respectively. Both figures indicate the consumption of O_2 and evolution of SO_2 during the temperature range of 600 and 800 °C. The evolution temperature observed in the present work is in good agreement with several previous works in the literature [19-21], which investigated the oxidation of Ce_2O_2S in the range of operating temperature between 600-800 °C by TPO technique and observed the evolution of SO_2 around 800 °C. According to the calculation of area under peaks from Figs. 4 and 5, the amount of SO_2 evolved was approximately 1.25 mol% from the sulfided sample at 700 °C by consuming oxygen of 2% whereas the amount of SO_2 evolved from the sulfided sample at 800 °C was about 3 mol% with the oxygen consuming of 4%. The difference in the amount of SO_2 evolution from the sulfidation at different temperatures, which was also observed by several researchers, could be mainly due to the increase of oxygen mobility on the

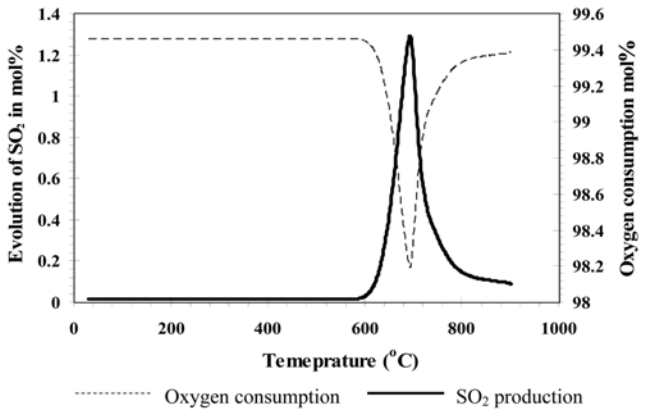

Fig. 4. Oxidative regeneration of CeO_2 sulfided at 700 °C.

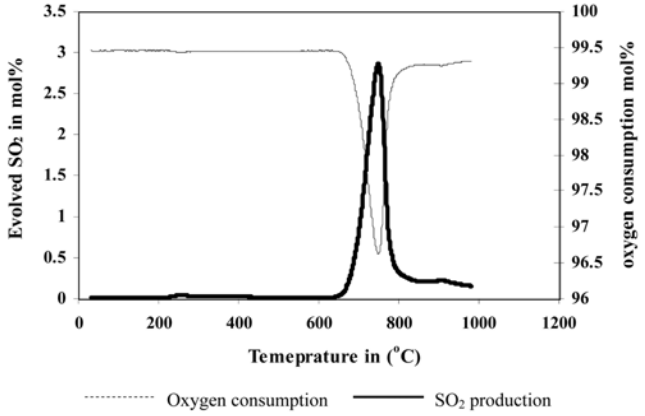

Fig. 5. Oxidative regeneration of CeO_2 sulfided at 800 °C.

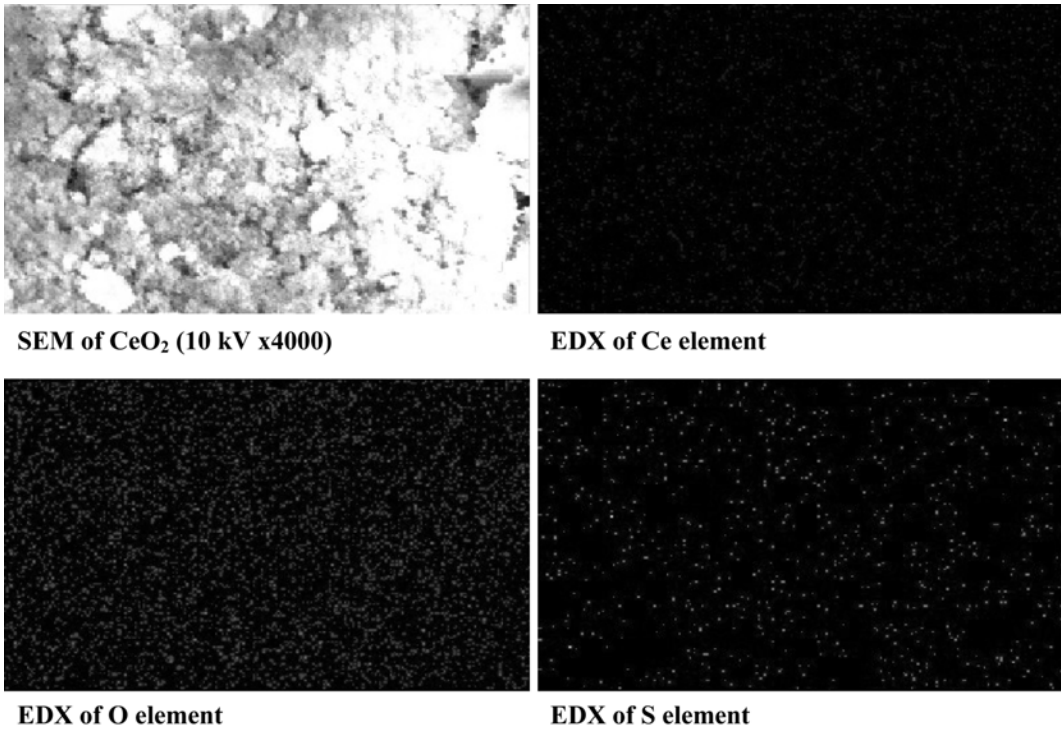

(a) SEM and elemental mapping of CeO_2 sulfided at 700°C

Fig. 6. Mapping of sulfur, oxygen and cerium distribution on the sulfided CeO_2.

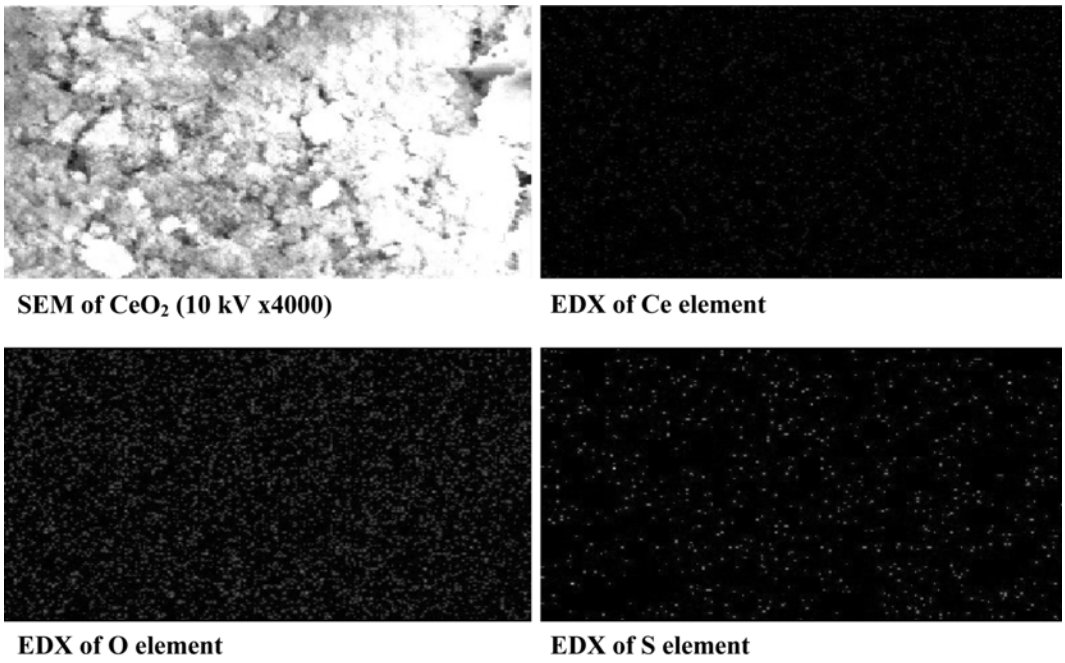

(b) SEM and elemental mapping of CeO_2 sulfided at 800°C

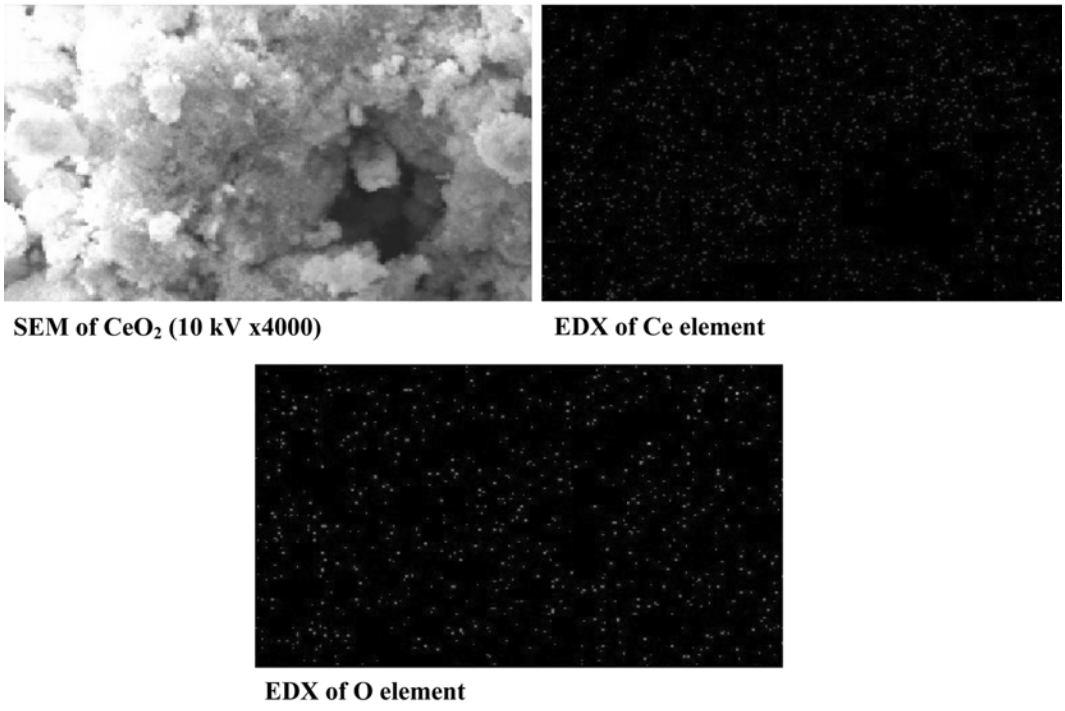

(c) SEM and elemental mapping of regenerated CeO_2

Fig. 6. Continued.

surface of CeO_2 by increasing temperature. It is well established that ceria-based material contains a high concentration of highly mobile oxygen vacancies, which act as local sources or sinks for oxygen involved in reactions taking place on its surface. That high oxygen mobility, high oxygen storage capacity, and its modifiable ability render the ceria-based material very interesting for a wide range of catalytic applications. At higher temperature, the gas-solid reaction between the inlet sulfur compound and the bulk lattice oxygen on the surface of CeO_2 occurred easily, and consequently resulted in a high sulfidation reaction [22]. Previous work from Zeng et al. [14] also reported that the degree of sulfidation increases with increasing temperature.

3. Characterization of Absorbent

Sulfided CeO_2 was subjected to its surface analysis by SEM/EDS and XRD measurements to determine the distribution of sulfur and the type of product formation on the surface of the CeO_2. From the SEM & EDS mapping as shown in Fig. 6, sulfur distribution on the surface of the catalyst was detected. According to the sulfur distribution at 700 and 800 °C, as shown in Figs. 6(a) and 6(b), respectively, the sulfur concentrations at 800 °C are higher than those at 700°C, which is in good agreement with the observed SO_2 peaks shown in Figs. 4 and 5. In addition, from the sulfur mapping observed by the EDS, it was found that the sulfur element was uniformly distributed over the surface of CeO_2. Larger particles in the figure are due to aggregation of smaller particles and the change in the porous structure. As CeO_2 consists of high surface oxygen ions, these ions make it become easily exchanged to sulfur upon H_2S adsorption [23].

In addition to the SEM/EDS measurement, sulfided CeO_2 was subjected to XRD studies to determine the type product formed. From the XRD analysis as shown in Fig. 8, major phases of the sulfided CeO_2 are Ce_2O_2S (Pattern 26-1085). The pattern was compared with that of pure CeO_2 (pattern 34-0394) as shown in Fig. 7. The XRD patterns of spent CeO_2 indicate that the cerium oxide sulfide (Ce_2O_2S) was formed from the reaction of CeO_2 with H_2S. Peaks of spent CeO_2 were decreased and peak broadening occurred at the

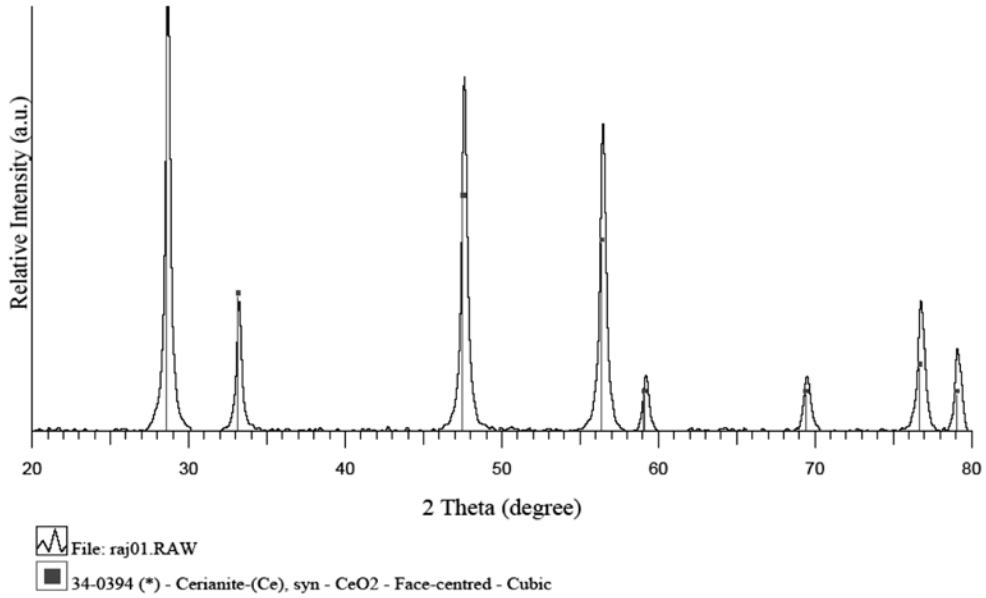

Fig. 7. XRD pattern of pure CeO_2.

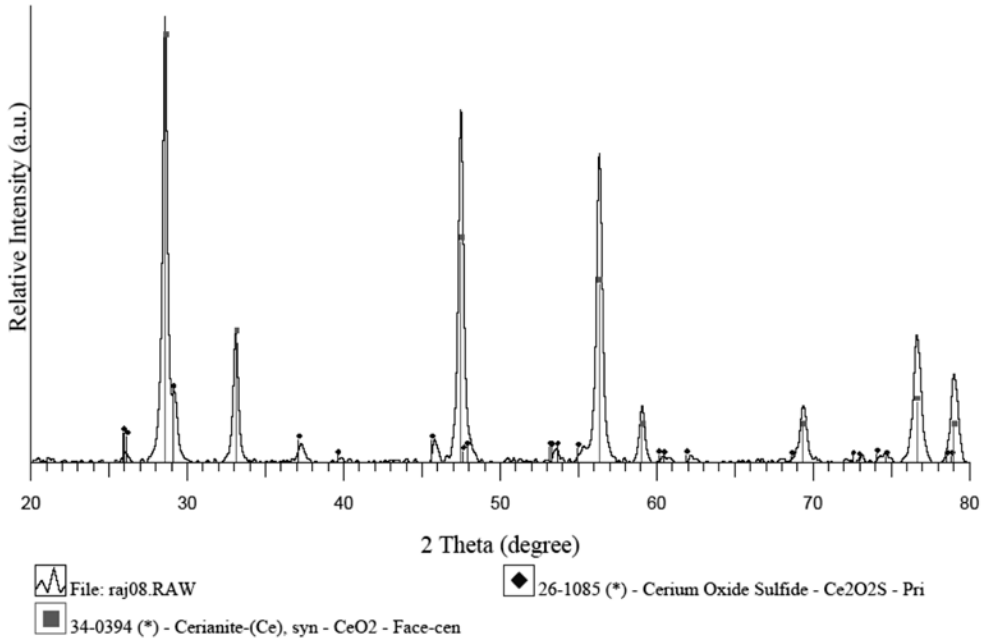

Fig. 8. XRD pattern of CeO_2 sulfided at 800 °C (JCPDS-ICDD).

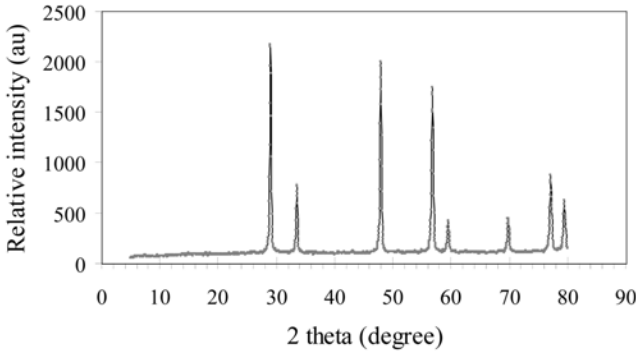

Fig. 9. XRD pattern of regenerated sulfided CeO_2 (JCPDS-ICDD).

CeO_2 peaks due to the formation of Ce_2O_2S. Sulfided CeO_2 was subjected to oxidative regeneration at a constant heating rate of 10 °C min^{-1} until 900 °C. The sample after regeneration was analyzed by XRD to determine its potential reuse as a CeO_2. It was found that the regenerated CeO_2 showed peaks at the same two theta angles as those of pure CeO_2 as shown in Fig. 9. This ensures the possible regeneration of sulfided CeO_2.

From the evidence of sulfidation, regeneration, and catalyst characterization, a sequence of reactions that occurred during these processes can be proposed. The possible reaction mechanism of the sulfidation and regeneration can be predicted as follows:

$$2CeO_2+H_2S \rightarrow Ce_2O_2S+H_2O+0.5O_2 \quad (4)$$

$$Ce_2O_2S+2O_2 \rightarrow SO_2+2CeO_2 \quad (5)$$

It should be noted that the detectable of steam from the desulfurization experiments and the observation of Ce_2O_2S phase from the XRD studies support this proposed sulfidation reaction mechanism: TPO and XRD analysis. The first experiment observed the formation of SO_2 from the regeneration process, while the second one confirmed that CeO_2 can be regenerated.

4. Deactivation Model for CeO_2 Absorbent

Deactivation models proposed in the literature [24] for gas-solid reactions with significant changes of activity of the solid due to textural changes, as well as product layer diffusion resistance during reaction, were reported to be quite successful in predicting conversion-time data. In the early work of Orbey et al. [16] and in the recent work of Suyadal et al. [25], deactivation models were used for the prediction of breakthrough curves in packed adsorption columns. In the present work, a deactivation model is proposed with the following assumptions: isothermal condition, pseudo-steady-state condition, first-order deactivation of the absorbent with respect to the solid surface which can be described in terms of an exponential decrease with time in its available surface, and constant activity throughout the surface of absorbent. The combined equation of mole balance and rate law for the packed bed reactor is given below:

$$Vo \cdot t\frac{dC_{H_2S}}{dt} = -k_o \cdot a(t)C_{H_2S} \quad (6)$$

The boundary conditions at inlet concentrations are

At t=0, $C_{H_2S}=C_{H_2Sin}$
At t=t, $C_{H_2S}=C_{H_2Sout}$

Therefore,

$$a(t)=\frac{Vo}{Wk}Ln\left(\frac{C_{H_2Sin}}{C_{H_2Sout}}\right) \quad (7)$$

The first order exponential decay is $a(t)=e^{-k_d t}$, substituting Eq. (6) to Eq. (8):

$$-k_d \cdot t = \ln\frac{Vo}{Wk_o} + \ln\ln\left(\frac{C_{H_2Sin}}{C_{H_2Sout}}\right) \quad (8)$$

This equation is equivalent to the breakthrough [25]. Thus, when $\ln\ln(C_{H_2Sin}/C_{H_2Sout})$ is plotted versus operating time (t), a straight line should be obtained with a slope equal to $-k_d$ and intercept equal to $\ln(Vo/Wk_o)$ as shown in Fig. 10. Table 3 summarizes the model parameters determined at different temperatures. The fluctuation of 10 to 15% in correlation coefficient may be due to initial bumps.

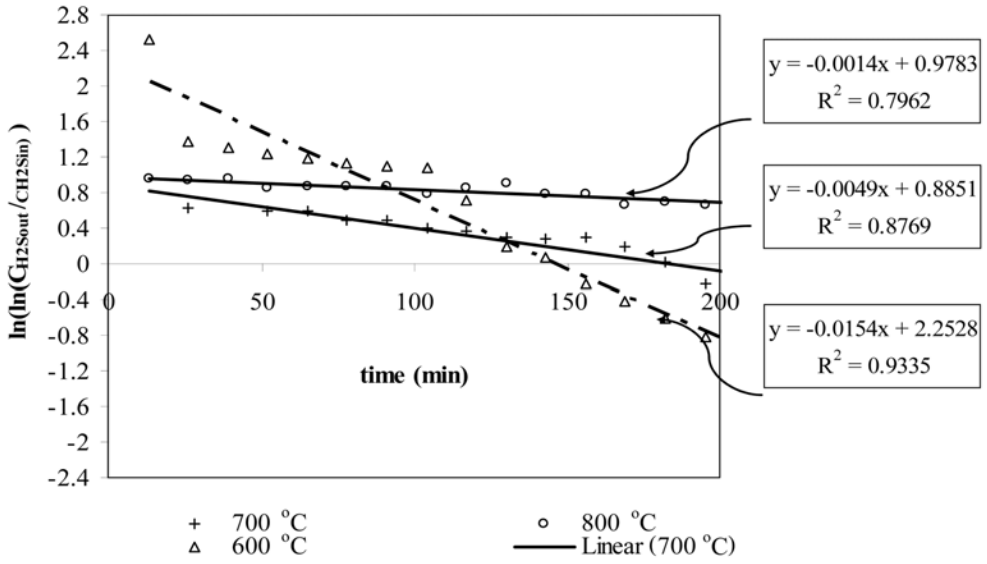

Fig. 10. Test of deactivation model equation.

Table 3. Summary of deactivation model parameters

Temperature (°C)	Vo/Wk$_o$ (-)	k$_o$ (cm^3 min^{-1} g^{-1})	k$_d$ (min^{-1})	R^2 (-)
600	2.55	3.566	0.0144	0.79
700	2.40	1.66	0.0049	0.89
800	2.66	1.503	0.0014	0.9351

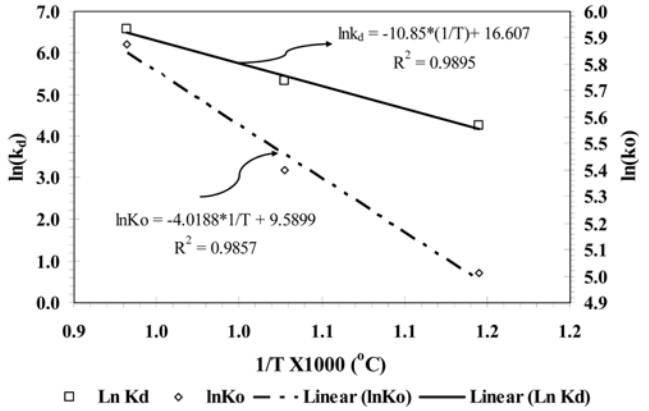

Fig. 11. Arrhenius plots of sorption rate constants and deactivation rate constants.

The advantage of the deactivation model is the presence of only two adjustable parameters such as initial sorption rate constant K_o and the deactivation rate constant K_d. Both parameters showed an increasing trend with respect to an increase in the temperature. Sorption rate constant K_o and the deactivation rate constant K_d were correlated as a function of temperature using by Arrhenius equations (Eqs. (9) and (10)).

$$K_o = k_o e^{-e/RT} \quad (9)$$

$$K_d = k_o e^{-e/RT} \quad (10)$$

The temeprature dependency was illustrated as shown in Fig. 11. The activation energies of k_o and k_d were found to be 33.4 and 90 kJ mol^{-1}. These high values of the activation energies indicate that the H_2S sorption on CeO_2 is chemical adsorption.

CONCLUSION

Nano-scale high surface area CeO_2 has useful desulfurization activity between 500 and 850 °C. Compared to the conventional low surface area CeO_2, 80-85% of H_2S was removed by nano-scale high surface area CeO_2, whereas 30-32% of H_2S was removed by conventional low surface area CeO_2. According to the XRD and EDS mapping, uniform Ce_2O_2S was formed after desulfurization. According to the TPO experiment, this component (Ce_2O_2S) can be recovered to CeO_2 after exposure in the oxidation condition at temperature above 600 °C. Furthermore, regarding the SEM/EDS and XRD measurements, all Ce_2O_2S forming is converted to CeO_2 after this oxidative regeneration.

As the final step, a deactivation model considering the concentration and temperature dependencies of the desulfurization activity was proposed for later application in the SOFC model.

ACKNOWLEDGMENT

The financial support from the Thailand Research Fund (TRF) and the Joint Graduate School of Energy and Environment (JGSEE) throughout this project is gratefully acknowledged. The authors are also thankful to Dr.Nakorn Srisukhumbowornchai for his valuable suggestions on XRD patterns.

REFERENCES

1. D. W. Park, B. H. Hwang, W. D. Ju, M. I. Kim, K. H. Kim and H. C. Woo, *Korean J. Chem. Eng.*, **22**, 190 (2005).
2. J. D. Lee, J. H. Jun, N. K. Park, S. O. Ryu and T. J. Lee, *Korean J. Chem. Eng.*, **22**, 36 (2005).
3. P. R. Westmoreland and D. P. Harrison, *Environ. Sci. Technol.*, **10**, 559 (1976).
4. H. T. Jang, S. B. Kim and D. S. Doh, *Korean J. Chem. Eng.*, **20**, 116 (2003).
5. T. H. Gardener, *Fuel*, **81**, 2157 (2002).
6. J. H. Swisher and K. Schwerdtfeger, *J. Mater. Eng. Perform.*, **1**, 399 (1992).
7. V. Patrick and G. R. Gavalas, *Ind. Eng. Chem. Res.*, **28**, 931 (1989).
8. V. V. Meng and D. A. R. Kay, *High technology ceramics*, Elsevier, Amsterdam, 2247 (1987).
9. D. A. R. Kay, W. G. Wilson and V. Jalan, *J. Alloys and Compounds*, **192**, 11 (1993).
10. K. H. Kim, S. Y. Lee and K. J. Yoon, *Korean J. Chem. Eng.*, **23**, 356 (2006).
11. K. H. Kim, S. Y. Lee, S. W. Nam, T. H. Lim, S. A. Hong and K. J. Yoon, *Korean J. Chem. Eng.*, **23**, 17 (2006).
12. J. Abbasian, A. H. Hill, M. Flytzani-Stephanopoulos and Z. Li, Final Report, DE-FC22-92PC92521 (1994).
13. Z. Li and M. Flytzani-Stephanopoulos, *Ind. Eng. Chem. Res.*, **36**, 187 (1997).
14. Y. Zeng, S. Zhang, F. R. Groves and D. P. Harrison, *Chem. Eng. Sci.*, **54**, 3007 (1999).
15. N. Laosiripojana and S. Assabumrungrat, *Applied Catal. B*, **60**, 107 (2005).
16. N. Orbey, G. Dogu and T. Dogu, *Can. J. Chem. Eng.*, **60**, 314 (1982).
17. H. S. Fogler, *Elements of chemical reaction engineering*, Prentice-Hall Inc, Englewood Cliffs, New Jersey 07632, ISBN 0-13-263476-7 (1986).
18. M. P. Cal, B. W. Strickler and A. A. Lizzio, *Carbon*, **38**, 1757 (2000).
19. R. M. Ferriz, R. J. Gorte and J. M. Vohs, *Applied Catal. B*, **43**, 273 (2003).
20. Z. Wang and M. Flytzani-Stephanopoulos, *Energy & Fuels*, **19**, 2093 (2005).
21. M. Flytzani-Stephanopoulos, Angela D. Surgenor, Report, NASA/TM-2007-214686.
22. S. Yasyerli, G. Dogu and T. Dogu, *Catal. Today*, **117**, 271 (2006).
23. M. Ziolek, *J. Molecular Catalysis A*, **97**, 49 (1995).
24. T. Dogu, *Chem. Eng. J.*, **21**, 213 (1981).
25. Y. Suyadal, M. Erol and H. Oguz, *Ind. Eng. Chem. Res.*, **39**, 724 (2000).

Available online at www.sciencedirect.com
ScienceDirect
Applied Catalysis B: Environmental 82 (2008) 103–113
APPLIED CATALYSIS B: ENVIRONMENTAL
www.elsevier.com/locate/apcatb

Kinetic dependencies and reaction pathways in hydrocarbon and oxyhydrocarbon conversions catalyzed by ceria-based materials

N. Laosiripojana [a,*], S. Assabumrungrat [b]

[a] *The Joint Graduate School of Energy and Environment, King Mongkut's University of Technology Thonburi, Bangkok 10140, Thailand*
[b] *Center of Excellence on Catalysis and Catalytic Reaction Engineering, Department of Chemical Engineering, Chulalongkorn University, Bangkok 10330 Thailand*

Received 8 February 2007; received in revised form 8 January 2008; accepted 16 January 2008
Available online 20 January 2008

Abstract

Hydrocarbons (i.e. CH_4, C_2H_4, C_2H_6, and C_3H_8) and oxyhydrocarbon (i.e. CH_3OH) conversions with and without co-reactants (H_2O and CO_2) were studied over ceria-based materials prepared by precipitation and cationic surfactant-assisted methods with/without Zr doping with an aim to understand their influences on material specific surface area, oxygen storage capacity (OSC), hydrocarbon reaction rate, resistance toward carbon deposition, and rigorous kinetic dependencies.

High surface area CeO_2 and Ce-ZrO_2 from the cationic surfactant-assisted method provided a higher degree of oxygen storage capacity (OSC) and reaction rates with greater resistance toward carbon deposition than those from the precipitation method. The reaction rates (mol g_{cat}^{-1} s^{-1}) per degree of OSC (mol_{Oxygen} g_{cat}^{-1}) were identical for all materials, indicating the linear influence of OSC on the rates. Nevertheless, the kinetic dependencies were unaffected by specific surface area, doping element, degree of OSC and reactions (i.e. H_2O reforming, CO_2 reforming and cracking). The rates were proportional to hydrocarbon partial pressures with positive fraction reaction orders; independent of co-reactant partial pressures; but inhibited by CO and H_2. These kinetic dependencies were explained by a set of redox mechanistic proposal, in which the relevant elementary step is the reaction of intermediate surface hydrocarbon with lattice oxygen (O_O^x), and that lattice oxygen is efficiently replenished by rapid surface reactions with oxygen source from either CO_2, H_2O, or even CH_3OH.

Keywords: Ceria; Oxygen storage capacity; Reforming; Redox mechanistic; Kinetic

1. Introduction

Cerium oxide (or ceria) based material contains a high concentration of mobile oxygen vacancies, which act as local sources or sinks for oxygen involved in reactions taking place on its surface. The high oxygen mobility and oxygen storage capacity render this material very interesting for a wide range of catalytic applications involving oxidation and reforming of hydrocarbons [1–8]. Recently, one of the great potential applications of ceria-based materials is in an Indirect Internal Reforming-Solid Oxide Fuel Cell (IIR-SOFC) as an in-stack reforming catalyst [9,10]. In addition, it is also successfully applied in a direct internal reforming (DIR-SOFC), in which hydrocarbon and oxyhydrocarbon compounds (i.e. C_4H_{10} and CH_3OH) were efficiently reformed at ceria-based anodes (i.e. Cu-CeO_2 and Cu-CeO_2-YSZ) [11–16].

It has been well established that the gas–solid reaction between hydrocarbons and the lattice oxygen (O_x^o) on ceria surface can generate CO and H_2 at high temperature; in addition, the reactions of reduced ceria with oxygen-containing reactants, i.e. CO_2 and H_2O can regenerate the lattice oxygen (O_x^o) on CeO_2 surface [10,17–19]. The great benefit of ceria-based catalysts for reforming reactions is their high resistance toward carbon deposition compared to conventional metal catalysts [9,10]; however, the weaknesses are their low specific surface area and high deactivation due to the thermal sintering particularly when operated at such a high temperature [20]. The use of high surface area ceria (CeO_2 (HSA)) with high resistance toward the sintering was proposed to be a good approach to improve its catalytic reactivity [20]. Several techniques have been described for the preparation of CeO_2 (HSA) solid solution, i.e. homogeneous precipitation techni-

* Corresponding author. Tel.: +66 2 8729014; fax: +66 2 8726736.
E-mail address: navadol_l@jgsee.kmutt.ac.th (N. Laosiripojana).

0926-3373/$ – see front matter © 2008 Elsevier B.V. All rights reserved.
doi:10.1016/j.apcatb.2008.01.009

ques with precipitating agents and additives [21–24], hydrothermal synthesis [25], spray pyrolysis methods [26], inert gas condensation of Ce followed by oxidation [27], thermal decomposition of carbonates [28], microemulsion [29], and electrochemical methods [30]. However, a few of these composites showed regular pore structure after calcination at moderate temperatures and a severe loss of surface area occurs during the thermal treatment [31]. Recently, Terribile et al. [32] synthesized CeO_2 (HSA) with improved textural, structural and chemical properties by using a novel cationic surfactant-assisted approach. They reported that CeO_2 with surface area of 40 $m^2\ g^{-1}$ was achieved after calcination at 1173 K. Compared to conventional CeO_2 (CeO_2 (LSA)) prepared by precipitation technique with surface area less than 10 $m^2\ g^{-1}$ after calcination at 1173 K [10], this highlights the great potential of CeO_2 prepared by surfactant-assisted technique for application as a catalyst under high reaction temperature. It should be noted that, apart from the investigation on preparation method, the addition of zirconium oxide (ZrO_2) has also been widely reported to improve surface area, oxygen storage capacity, redox property, thermal stability and catalytic activity of ceria [33–39].

Focusing on the reforming reactions of hydrocarbon compounds over ceria-based materials, until now, the reaction pathways and kinetic dependencies remains unclear. Here, we thereby probe the kinetic dependencies of hydrocarbons (i.e. CH_4, C_2H_4, C_2H_6, and C_3H_8) and also oxyhydrocarbon (i.e. CH_3OH) conversion with and without co-reactants over ceria-based materials prepared by precipitation and cationic surfactant-assisted methods and with/without Zr doping. The relation between the material specific surface area, doping element, oxygen storage capacity (OSC), reaction rate, resistance toward carbon deposition, and kinetic dependence were identified. A rigorous kinetic, reaction pathways and rate expressions were then established.

2. Experimental methods

2.1. Material synthesis and characterization

CeO_2 was synthesized by precipitation (CeO_2 (LSA)) and cationic surfactant-assisted (CeO_2 (HSA)) methods. These preparation methods were described elsewhere in our previous publication [40]. The materials were dried overnight in ambient air at 383 K, and then calcined in a flow of dry air by increasing the temperature to 1173 K with a rate of 0.167 K s^{-1} and holding at 1173 K for 6 h. After calcined, fluorite-structured CeO_2 with good homogeneity were obtained.

$Ce_{1-x}Zr_xO_2$ (or Ce-ZrO_2) with different Ce/Zr molar ratios were prepared by either co-precipitation or surfactant-assisted method of cerium nitrate ($Ce(NO_3)_3{\cdot}H_2O$), and zirconium oxychloride ($ZrOCl_2{\cdot}H_2O$) (from Aldrich). The ratio between each metal salt was altered to achieve nominal Ce/Zr molar ratios: $Ce_{1-x}Zr_xO_2$, where x = 0.25, 0.50, and 0.75 respectively. After treatment, the specific surface areas of all CeO_2 and Ce-ZrO_2 were achieved from BET measurement. As presented in Table 1, after drying in the oven, surface areas of 105 and 55 $m^2\ g^{-1}$ were observed for CeO_2 (HSA) and CeO_2 (LSA), respectively and, as expected, the surface area decreased at high calcination temperatures. However, the value for CeO_2 (HSA) is still appreciable after calcination at 1173 K. It can also be seen that the introduction of ZrO_2 stabilizes the surface area of ceria, which is in good agreement with several previous reports [41–43]. After treatment, the degree of OSC and redox reversibilities of all CeO_2 and Ce-ZrO_2 were determined by the temperature programmed reduction (TPR-1) and temperature programmed oxidation (TPO) following with second time temperature programmed reduction (TPR-2), respectively, at the same conditions. Details of these measurements are given in Section 3.1.

Table 1
Specific surface areas of ceria-based materials before and after calcination at 1173 K

Catalysts	Surface area after drying ($m^2\ g^{-1}$)	Surface area after calcinations ($m^2\ g^{-1}$)
CeO_2 (HSA)	105	29
Ce-ZrO_2 (HSA) (Ce/Zr = 1/3)	135	49
Ce-ZrO_2 (HSA) (Ce/Zr = 1/1)	120	47
Ce-ZrO_2 (HSA) (Ce/Zr = 3/1)	115	46.5
CeO_2 (LSA)	55	11
Ce-ZrO_2 (LSA) (Ce/Zr = 1/3)	82	22
Ce-ZrO_2 (LSA) (Ce/Zr = 1/1)	74	20.5
Ce-ZrO_2 (LSA) (Ce/Zr = 3/1)	70	20

2.2. Catalytic H_2O and CO_2 reforming and cracking of hydrocarbons

To undergo the catalytic testing, an experimental reactor system was constructed as shown elsewhere [40]. The feed gases including the components of interest, i.e. CH_4, C_2H_4, C_2H_6, C_3H_8, CH_3OH, deionized H_2O (introduced via a syringe pump pass through an evaporator), CO_2, CO, and H_2 were introduced to a 10-mm diameter quartz reactor, which was mounted vertically inside tubular furnace. The catalysts (50 mg of ceria-based catalysts) were diluted with SiC (to obtain the total weight of 500 mg) in order to avoid temperature gradients and loaded in the quartz reactor. Preliminary experiments were carried out to find suitable conditions in which internal and external mass transfer effects are not predominant. Considering the effect of external mass transfer, the total flow rate was kept constant at 100 $cm^3\ min^{-1}$ under a constant residence time of 5×10^{-3} g min cm^{-3} in all testing. The suitable average sizes of catalysts were also verified in order to confirm that the experiments were carried out within the region of isothermal kinetics. In our system, a Type-K thermocouple was placed into the annular space between the reactor and furnace. This thermocouple was mounted in close contact with the catalyst bed to minimize the temperature difference. Another Type-K thermocouple, covering by closed-end quartz tube, was inserted in the middle of the quartz reactor in order to re-check the possible temperature gradient.

Table 2
Results of TPR-1, TPO, TPR-2 analyses of ceria-based materials after calcination

Catalyst	Total H_2 uptake from TPR-1 ($\mu mol/g_{cat}$)	Total O_2 uptake from TPO ($\mu mol/g_{cat}$)	Total H_2 uptake from TPR-2 ($\mu mol/g_{cat}$)
CeO_2 (HSA)	4105	2067	4109
Ce-ZrO_2 (HSA) (Ce/Zr = 1/3)	2899	1475	2876
Ce-ZrO_2 (HSA) (Ce/Zr = 1/1)	3701	1862	3694
Ce-ZrO_2 (HSA) (Ce/Zr = 3/1)	5247	2640	5250
CeO_2 (LSA)	1794	898	1788
Ce-ZrO_2 (LSA) (Ce/Zr = 1/3)	1097	553	1085
Ce-ZrO_2 (LSA) (Ce/Zr = 1/1)	1745	744	1746
Ce-ZrO_2 (LSA) (Ce/Zr = 3/1)	2649	1328	2643

After the reactions, the exit gas mixture was transferred via trace-heated lines (373 K) to the analysis section, which consists of an online Porapak Q column Shimadzu 14B gas chromatograph (GC) with TCD and FID detectors and a mass spectrometer (MS). The GC was applied for the steady state kinetic studies, whereas the MS in which the sampling of the exit gas was done by a quartz capillary and differential pumping was used for the transient experiments. Kinetic effects were studied over wide ranges of temperature and reactant partial pressures.

2.3. Measurement of carbon formation

The temperature programmed oxidation (TPO) was applied to investigate the amount of carbon formed on catalyst surface by introducing 10% O_2 in He into the system, after purging with helium. The operating temperature increased from room temperature to 1273 K by a rate of 10 K min^{-1}. The amount of carbon formation on the surface of catalysts was determined by measuring the CO and CO_2 yields from the TPO results. In addition to the TPO method, the amount of carbon deposition was reconfirmed by the calculation of carbon balance in the system, which theoretically equals to the difference between inlet and outlet carbon containing components.

3. Results and discussion

3.1. Redox properties and redox reversibility

After treatment, the degree of OSC for fresh ceria-based materials were investigated using TPR-1, which was performed by heating the catalysts up to 1273 K in 5%H_2 in He. The amount of H_2 uptake was correlated to the amount of oxygen stored in the catalysts. As presented in Table 2, the amount of H_2 uptakes over Ce-ZrO_2 and CeO_2 (HSA) are significantly higher than those over the low surface area cerias, suggesting the increasing of OSC with the doping of Zr and the increasing of material specific surface area. The benefit of OSC on the reforming reaction will be later presented in Section 3.3.

After purging with He, the redox reversibilities were then determined by applying TPO following with TPR-2. The TPO was carried out by heating the catalyst up to 1273 K in 10%O_2 in He; the amounts of O_2 chemisorbed were then measured, Table 2. Regarding the TPR-2 results as also shown in Table 2, the amount of hydrogen uptakes for all materials were approximately similar to those from the TPR-1, indicating the reversibility of OSC for these synthesized ceria-based materials.

3.2. Reactivity toward the (H_2O and CO_2) reforming and cracking of CH_4

The H_2O reforming, CO_2 reforming and cracking of CH_4 were tested at 1123 K by introducing CH_4 along with co-reactant (for H_2O and CO_2 reforming). It should be noted that the reactions over Ce-ZrO_2 catalysts with different Ce/Zr ratios (1/3, 1/1, and 3/1) were firstly tested. The results revealed that Ce-ZrO_2 with Ce/Zr ratio of 3/1 shows the best performance in terms of stability and activity. Therefore, we report here detailed reactivity and kinetic data of Ce-ZrO_2 only with Ce/Zr ratio of 3/1.

Fig. 1 shows the variations in CH_4 reforming rate ($mol_{CH_4}\, g_{cat}^{-1}\, s^{-1}$) with time at the initial state (10 min; using MS) over Ce-ZrO_2 (HSA) by varying inlet co-reactant/CH_4 ratios from 0.0 (cracking reaction) to 0.3, 0.5, 0.7, 1.0, and 2.0, while Fig. 2 shows the stability and activity (under the period of 10 h; using GC-TCD) of H_2O and CO_2 reforming of CH_4 over several catalysts. The reforming rates expressed in the figures are obtained from the relation between the measured net reaction rate (r_m; $mol_{CH_4}\, g_{cat}^{-1}\, s^{-1}$) and the approach to equilibrium condition (η) using the following equation [44]:

$$r_t = r_m(1-\eta)^{-1} \tag{1}$$

where η is either the approach to equilibrium for H_2O reforming (η_s) or for CO_2 reforming (η_d). Both parameters are determined from the following equation:

$$\eta_s = \frac{[P_{CO}][P_{H_2}]^3}{[P_{CH_4}][P_{H_2O}]}\frac{1}{K_s} \tag{2}$$

$$\eta_d = \frac{[P_{CO}]^2[P_{H_2}]^2}{[P_{CH_4}][P_{CO_2}]}\frac{1}{K_d} \tag{3}$$

where P_i is partial pressure of component i (atm); K_s and K_d are the equilibrium constants for H_2O and CO_2 reforming of CH_4 at a given temperature. It should be noted that, in the present work, the values of η were always kept below 0.2 in all experiments.

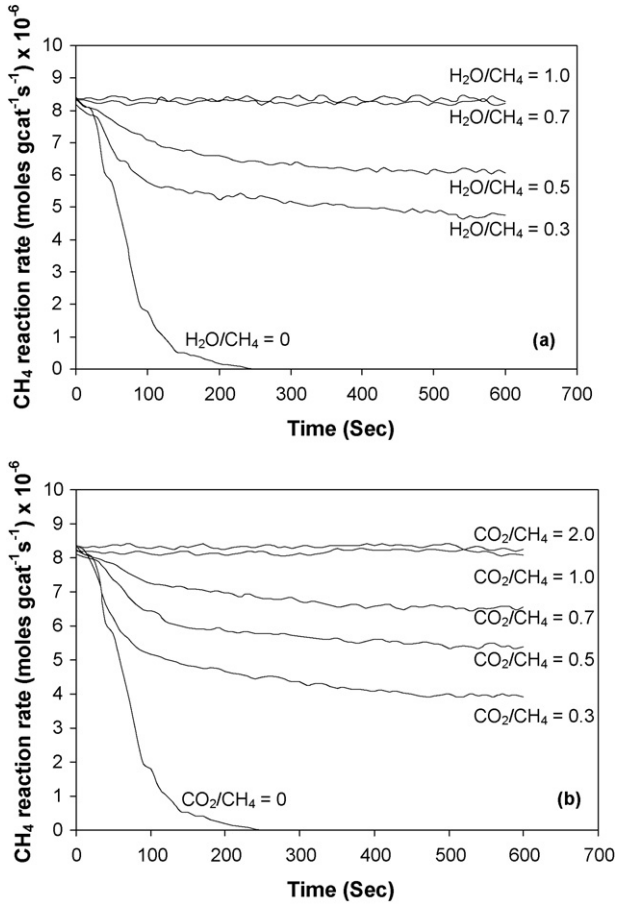

Fig. 1. CH_4 reaction rate at initial state (10 min) for H_2O reforming of CH_4 (a) and CO_2 reforming of CH_4 (b) over Ce-ZrO_2 (HSA) (1123 K with 3 kPa CH_4 in He).

The main products from the reactions over these catalysts were H_2 and CO with some CO_2, indicating a contribution from the water–gas shift at this high temperature. Based on the measured concentrations of reactants and products during CH_4 reforming, the approach to water-gas shift equilibrium condition (η_{WGS}) in the range of temperature studied (1023–1123 K) are always close to 1.0 in all type of catalysts, indicating that water–gas shift (WGS) reaction is at equilibrium. Fig. 1 indicates that the initial CH_4 reforming rate is unaffected by the concentration and type of co-reactants. Nevertheless, significant deactivation was observed for the cracking of CH_4 due to the loss of lattice oxygen (O_O^x) on the surface of ceria-based materials without the replacement by external oxygen containing sources (i.e. H_2O and CO_2). The rate of deactivation rapidly reduced when small content of H_2O or CO_2 was added.

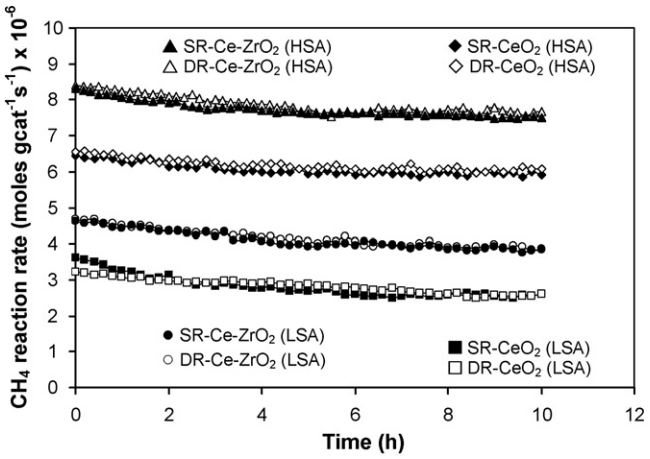

Fig. 2. Stability and activity testing of H_2O reforming (SR) and CO_2 reforming (DR) of CH_4 over several catalysts (at 1123 K with 3 kPa CH_4 and 3 kPa co-reactants).

Fig. 2 indicates that, at steady state, the high surface area materials showed much higher reactivity toward the CH_4 reforming than the low surface area one. Nevertheless, it should be noted that the CH_4 reaction rates ($mol_{CH_4}\ g_{cat}^{-1}\ s^{-1}$) per surface area ($m^2\ g^{-1}$) (in Table 1) for each type of catalyst with different surface areas are in the same range, e.g. $2.0-2.2 \times 10^{-7}\ mol_{CH_4}\ (m^2\ s)^{-1}$ for CeO_2, $1.0-1.1 \times 10^{-7}\ mol_{CH_4}\ (m^2\ s)^{-1}$ for Ce-ZrO_2 (Ce/Zr = 1/1), and $1.6-1.8 \times 10^{-7}\ mol_{CH_4}\ (m^2\ s)^{-1}$ for Ce-ZrO_2 (Ce/Zr = 3/1) (with the operating conditions of 3 kPa CH_4 at 1123 K) indicating the great impact of catalyst specific surface area on the rate. In addition, importantly, at the same reaction conditions, the CH_4 reaction rates ($mol_{CH_4}\ g_{cat}^{-1}\ s^{-1}$) per degree of OSC ($mol_{Oxygen}\ g_{cat}^{-1}$) (in Table 2) for all catalyst are approximately identical ($2.8 \times 10^{-3}\ mol_{CH_4}\ mol_{oxygen}^{-1}\ s^{-1}$ for the inlet CH_4 of 3 kPa at 1123 K) indicating the linear influence of OSC on the reforming reactivity.

After purging in helium, the TPO detected small amount of carbon on the surface of materials from CH_4 cracking reaction (between 0.09 and 0.15 mmol g_{cat}^{-1} for high surface area materials and between 0.18 and 0.21 mmol g_{cat}^{-1} for low surface area one). These amounts of carbon deposited were ensured by the calculation of carbon balance. Regarding the calculation, the moles of carbon remaining in the system were 0.07–0.14 mmol g_{cat}^{-1} for high surface area materials and were 0.20 ± 0.01 mmol g_{cat}^{-1} for low surface area materials, which are in good agreement with the values observed from the TPO. No carbon formation was observed on high surface area materials when the inlet H_2O/CH_4 and CO_2/CH_4 ratios were higher than 0.7 and 1.0, whereas low surface area materials required inlet H_2O/CH_4 and CO_2/CH_4 ratios higher than 1.0 and 2.0 to operate without detectable carbon. The good resistance toward carbon deposition for ceria-based materials, which has been widely reported by previous researchers [9–10], is mainly due to their sufficient oxygen storage capacity (OSC). It should be noted that we observed high amount of carbon formation on the surface of Ni catalysts after exposure in the same reforming conditions as ceria-based materials [45,46]. Regarding the possible carbon formation during the reforming processes, the following reactions are theoretically the most probable reactions that could lead to carbon formation:

$$2CO \Leftrightarrow CO_2 + C \quad (4)$$

$$CH_4 \Leftrightarrow 2H_2 + C \quad (5)$$

$$CO + H_2 \Leftrightarrow H_2O + C \quad (6)$$

$$CO_2 + 2H_2 \Leftrightarrow 2H_2O + C \quad (7)$$

At low temperature, reactions (6) and (7) are favorable, while reactions (4) and (5) are thermodynamically unflavored [47]. The Boudouard reaction (Eq. (4)) and the decomposition of CH_4 (Eq. (5)) are the major pathways for carbon formation at such a high temperature as they show the largest changes in Gibbs energy [48]. According to the range of temperature in this study, carbon formation would be formed via the decomposition of CH_4 and Boudouard reactions especially at high inlet CH_4/co-reactant ratio. By applying CeO_2, both reactions (Eqs. (4) and (5)) could be inhibited by the redox reaction between the surface carbon (C) forming via the adsorptions of CH_4 and CO (produced during the reforming process) with the lattice oxygen (O_O^x) at CeO_2 surface (Eq. (8)).

$$C + O_O^x \rightarrow CO + V_O^{\bullet\bullet} + 2e' \quad (8)$$

Using the Kroger–Vink notation, $V_O^{\bullet\bullet}$ denotes as an oxygen vacancy with an effective charge 2^+, and e' is an electron which can either be more or less localized on a cerium ion or delocalized in a conduction band. The greater resistance toward carbon deposition for high surface area ceria-based catalyst particularly Ce-ZrO_2 (HSA) is due to the significant higher amount of lattice oxygen (O_O^x) on their surfaces, according to the results in Section 3.1.

3.3. Kinetic dependencies of forward CH_4 reforming rate on partial pressures of reactants (i.e. CH_4 and H_2O or CO_2) and products (CO and H_2)

The kinetic dependencies of CH_4 reforming rates on the partial pressures of CH_4, H_2O, CO_2, CO, and H_2 for all ceria-based materials were studied in the temperature range of 1023–1123 K. All measurements were carried out under the operating conditions without detectable carbon formation by controlling H_2O/CH_4 and CO_2/CH_4 inlet ratios according to the results from Section 3.2.

Fig. 3 shows the effect of CH_4 partial pressure on the rate ($mol_{CH_4}\ mol_{oxygen}^{-1}\ s^{-1}$) over Ce-$ZrO_2$ (HSA) at several reaction temperatures, while Fig. 4 shows the effect of CH_4 partial pressure on the rate (per degree of OSC) over different catalysts

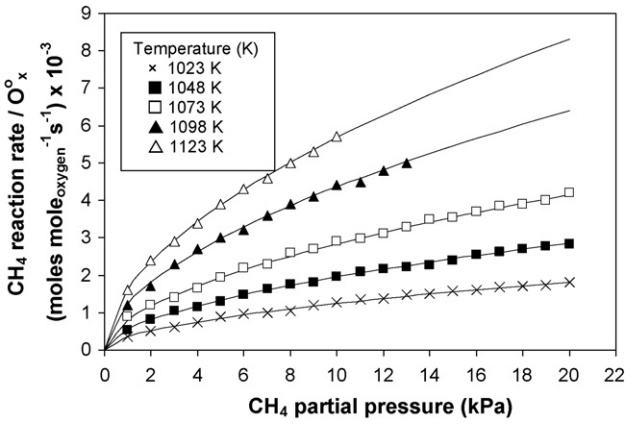

Fig. 3. Effect of temperature on CH_4 steam reforming over Ce-ZrO_2 (HSA) (with inlet CH_4/H_2O of 1.0).

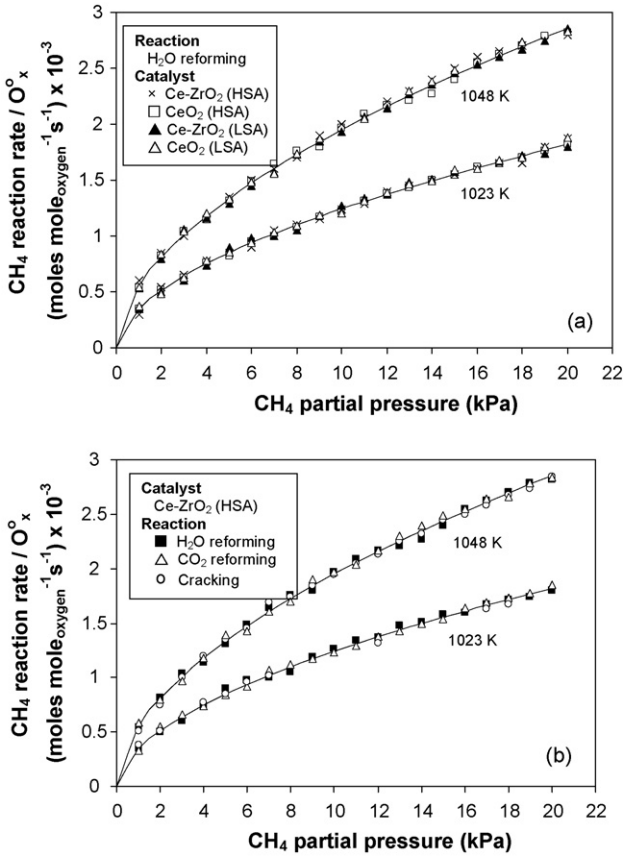

Fig. 4. Effect of CH_4 partial pressure on CH_4 reaction rate (per moles of oxygen stored) over different catalysts (a) and different reactions (b).

(Fig. 4a) and different reactions (i.e. H_2O reforming, CO_2 reforming and cracking (initial rates) of CH_4) (Fig. 4b). The rate increased with increasing CH_4 partial pressures and operating temperature for all catalysts and reactions. The reaction order in CH_4 was determined by plotting $\ln(r_t)$ versus $\ln \ln P_{CH_4}$ (the effects of product concentrations are taken into account via the term equilibrium condition (η)). The reaction orders in other components (CO_2, H_2O, H_2, and CO) were achieved using the same approach. The reaction order in CH_4 was observed to be positive fraction values approximately 0.52 ($\pm$0.03) for all catalysts and reactions, and seemed to be independent of temperature and co-reactant (CO_2 and H_2O) partial pressures in the range of conditions studied.

Several inlet CO_2 or H_2O partial pressures were then introduced to the feed with constant CH_4 partial pressure in order to investigate the influence of these co-reactant partial pressures on the rate. Fig. 5 shows the effects of co-reactant on CH_4 reaction rate with several inlet CH_4 partial pressures over different reactions (Fig. 5a) and over different catalysts (Fig. 5b). It is clear that the rates were not influenced by H_2O and CO_2 partial pressures; thus, the reaction orders in both components would be zero. The reforming in the presences of CO and H_2 were also investigated by adding either CO or H_2 to the feed gas at several operating temperatures. The results in Figs. 6 and 7 showed that the rates are dependent on both CO and H_2 concentrations. Unlike CH_4, both components inhibited the rate. The reaction order in CO was in the range of -0.15 to

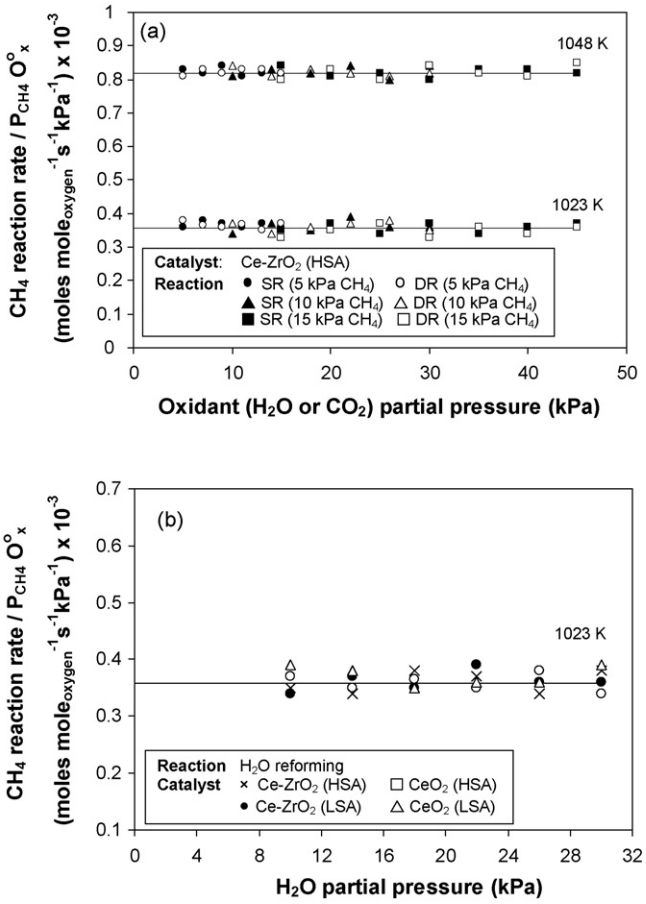

Fig. 5. Effect of co-reactant on CH_4 reaction rate (per moles of oxygen stored and inlet CH_4 partial pressure) over different reactions (with several inlet CH_4 partial pressures) (a) and different catalysts (b).

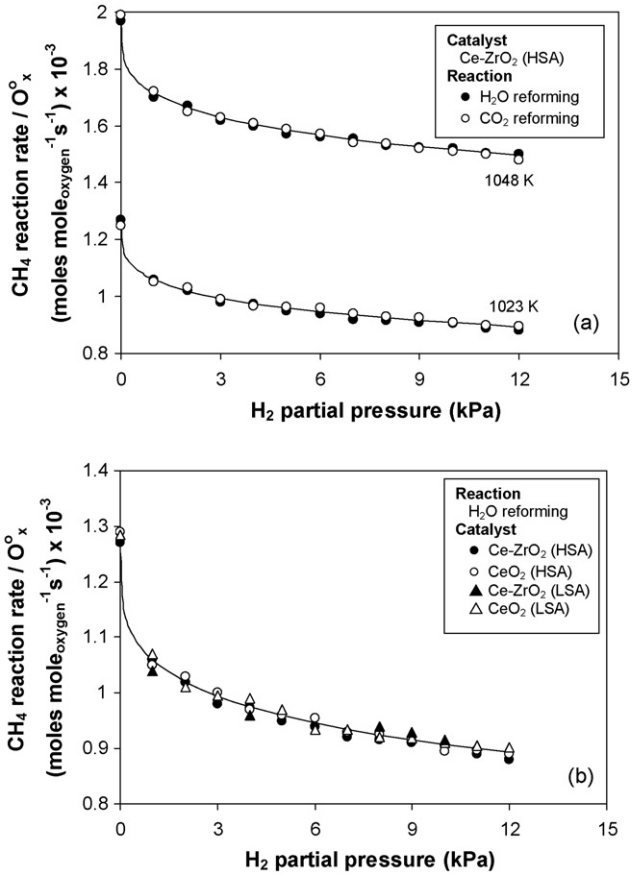

Fig. 6. Effect of H_2 on CH_4 reaction rate (per moles of oxygen stored) over different reactions (a) and different catalysts (b).

-0.12, while the reaction order in H_2 was between -0.31 and -0.28 for all catalysts. Similar reaction orders and kinetic constants for all ceria-based materials indicate that the kinetic dependencies are not affected by the specific surface area (or degree of OSC) and the doping of Zr.

Some previous researchers have proposed the redox mechanism to explain the reforming behavior of ceria-based catalysts [9,10]. They indicated that the reforming reaction mechanism involves the reaction between methane, or an intermediate surface hydrocarbon species, and lattice oxygen at the ceria-based material surface [9]. During reforming reaction, the isothermal reaction rate reaches steady state where the co-reactant, i.e. steam, provides a continuous source of oxygen. They also proposed that the controlling step is the reaction of methane with ceria, and that oxygen is replenished by a significantly more facile surface reaction of the ceria with steam [9]. Therefore, we suggested here that the CH_4 reaction pathway for ceria-based materials involves the reaction between absorbed CH_4 (forming intermediate surface hydrocarbon species) with the lattice oxygen (O_O^x) at CeO_2 surface, as illustrated schematically below.

CH_4 adsorption

$$CH_4 + 2* \rightarrow CH_3* + H* \quad (9)$$

$$CH_3* + * \rightarrow CH_2* + H* \quad (10)$$

$$CH_2* + * \rightarrow CH* + H* \quad (11)$$

$$CH* + * \rightarrow C* + H* \quad (12)$$

Co-reactant (H_2O and CO_2) adsorption

$$H_2O + 2* \Leftrightarrow OH* + H* \quad (13)$$

$$OH* + * \Leftrightarrow H* + O* \quad (14)$$

$$CO_2 + 2* \Leftrightarrow CO* + O* \quad (15)$$

Redox reactions of lattice oxygen (O_O^x) with C* and O*

$$C* + O_O^x \rightarrow CO* + V_O^{\bullet\bullet} + 2e' \quad (16)$$

$$V_O^{\bullet\bullet} + 2e' + O* \Leftrightarrow O_O^x + * \quad (17)$$

Inhibitory effects of CO and H_2

$$H_2 + 2* \Leftrightarrow H* + H* \quad (18)$$

$$H* + O_O^x \Leftrightarrow OH* + V_O^{\bullet\bullet} + 2e' \quad (19)$$

$$CO + * \Leftrightarrow CO* \quad (20)$$

$$CO* + O_O^x \Leftrightarrow CO_2* + V_O^{\bullet\bullet} + 2e' \quad (21)$$

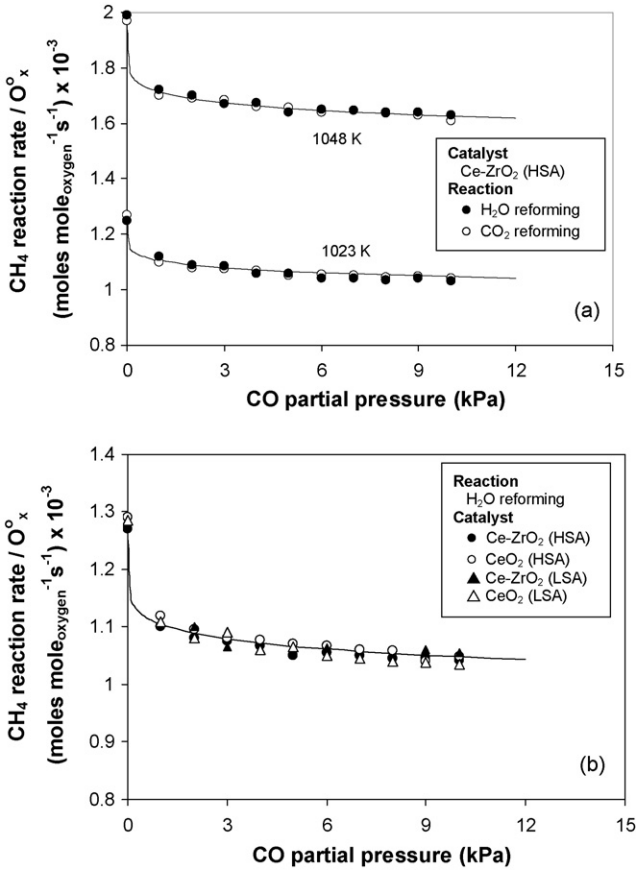

Fig. 7. Effect of CO on CH_4 reaction rate (per moles of oxygen stored) over different reactions (a) and different catalysts (b).

where * is the surface active site of ceria-based materials. During the reactions, CH_4 adsorbed on * forming intermediate surface hydrocarbon species (CH^*_x) (Eqs. (9–12)) and later reacted with the lattice oxygen (O_O^x) (Eq. (16)). The steady-state reforming rate is due to the continuous supply of the oxygen source by either CO_2 or H_2O (Eqs. (13–15)) that reacted with the reduced-state catalyst to recover lattice oxygen (O_O^x) (Eq. (17)). The identical rate for the H_2O and CO_2 reforming at similar CH_4 partial pressures, as well as the stronger linear dependence of the reforming rate on CH_4 partial pressure with the positive fraction value of reaction order in this component, and the independent effects of CO_2 and H_2O provide the evidence that the sole kinetically relevant elementary step is the reaction of intermediate surface hydrocarbon species with the lattice oxygen (O_O^x), and that oxygen is replenished by a significantly rapid surface reaction of the reduced state with the oxygen source from either CO_2 or H_2O; this fast step maintains the lattice oxygen (O_O^x) essentially unreduced by adsorbed intermediate surface hydrocarbon. The unchanged state of lattice oxygen was confirmed by the calculation of oxygen balance during reactions and TPO after reactions. We have used these methods to probe the state of lattice oxygen, because characterizations of used catalysts are not practical due to the low catalyst amounts used and its mixing with SiC. According to the oxygen balance calculation, the mole of oxygen (from co-reactant) fed into the system was almost similar to that in the products for all reactions and testing times indicating the unchanged state of CeO_2 (to CeO_{2-x}) during the experiments. Furthermore, the TPO results after reactions also proved the unchanged state of material, as no oxygen uptakes were detected.

The negative effects of CO and H_2 are due to the reactions between these adsorbed components (CO* and H*) with the lattice oxygen (O_O^x) (Eqs. (18–21)), which consequently result in the inhibition of CH_4 conversion. From all observation, a simple CH_4 reaction rate expression for H_2O reforming, CO_2 reforming and cracking (initial rate) can be written as following:

$$\text{Rate} = \frac{k[P_{CH_4}]^{0.5}}{1 + K_H[P_{H_2}]^{0.3} + K_{CO}[P_{CO}]^{0.15}} \quad (22)$$

where P_i is the partial pressure of chemical component i, k is the rate constant, and K_{CO} and K_H are adsorption parameters, obtained from Van't Hoff equation. The rate constants (k) and the activation energies measured from the H_2O reforming, CO_2 reforming and cracking (initial rate) of CH_4 are identical

Table 3
CH_4 reaction rate, rate constant and activation energies for CH_4 reactions on ceria-based materials (1048 K, 10 kPa CH_4 balance in He)

Catalysts	Reaction	CH_4 reaction rate/O_O^x (moles $mole^{-1}_{oxygen}$ s^{-1}) × 10^{-3}	Rate constant (s^{-1} kPa^{-1}) × 10^{-3}	Activation energy (kJ mol^{-1})
CeO_2 (HSA)	H_2O reforming	1.96	0.53	154.2
	CO_2 reforming	1.98	0.55	155.0
	Cracking	1.95[a]	0.53	151.8
Ce-ZrO_2 (HSA)	H_2O reforming	1.97	0.54	154.2
	CO_2 reforming	1.95	0.52	153.4
	Cracking	1.94	0.55	150.9
CeO_2 (LSA)	H_2O reforming	1.96	0.56	154.9
	CO_2 reforming	1.95	0.54	152.1
	Cracking	1.96	0.57	154.3
Ce-ZrO_2 (LSA)	H_2O reforming	1.95	0.56	155.2
	CO_2 reforming	1.94	0.55	154.4
	Cracking	1.97	0.55	153.2

[a] Initial CH_4 reaction rate.

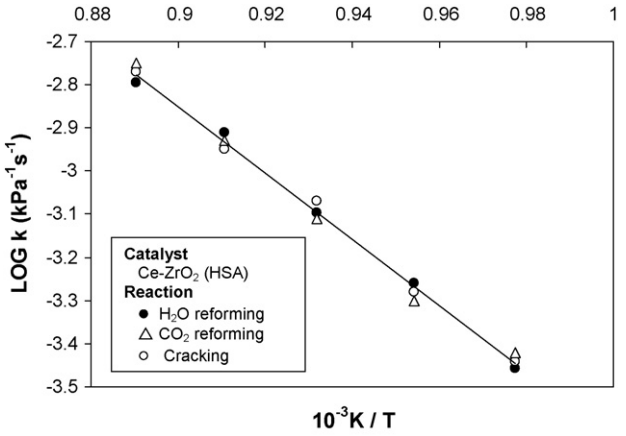

Fig. 8. Arrhenius plots for H_2O reforming, CO_2 reforming and cracking of CH_4 over Ce-ZrO_2 (HSA).

at each reaction temperature, Table 3. The activation energies for these three reactions, achieved by the Arrhenius plots as shown in Fig. 8, were between 150 and 155 kJ mol^{-1}, which are in good agreement with the values previously reported [9–10]. Due to the identical CH_4 reaction rates, the reaction order in CH_4, the rate constants, and the activation energies for all H_2O reforming, CO_2 reforming and cracking of CH_4, it could be concluded that all three reactions over ceria-based materials have similar reaction pathways in CH_4 activity.

3.4. Reactivity toward reforming and decomposition of oxyhydrocarbon

The decompositions of CH_3OH with and without co-reactant elements (i.e. H_2O and CO_2) were studied to confirm the above redox mechanism. The feed condition was co-reactant/CH_3OH in helium with the several molar ratios in the temperature range of 873–1073 K (to prevent the influence of homogeneous non-catalytic reaction). It should be noted according to our experimental results that, similar to CH_4 reforming, the reaction rate (per degree of OSC) and the kinetic dependencies of CH_3OH reaction rates were identical for all ceria-based materials, except the requirement of inlet co-reactant partial pressure to operate without detectable carbon formation. We thereby report here detailed reactivity and kinetic data only on Ce-ZrO_2 (HSA) sample.

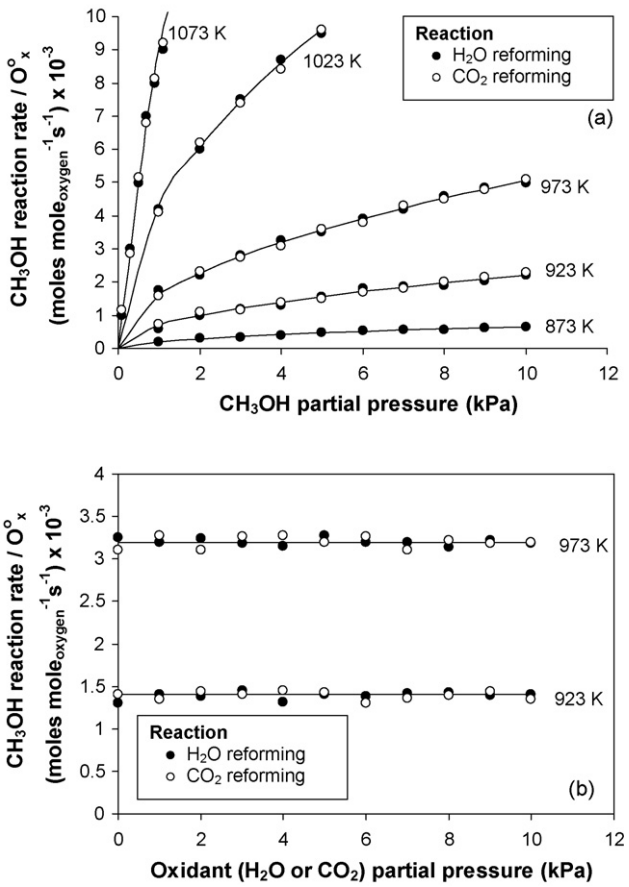

Fig. 9. Effects of CH_3OH partial pressure (a) and co-reactant partial pressure (b) on CH_3OH reaction rate (per moles of oxygen stored) over Ce-ZrO_2 (HSA).

After operation for 10 h, the main products from the reaction were H_2, CO, and CO_2, with small amount of CH_4 depending on the operating conditions, Table 4. According to the TPO, no carbon formation was observed in all studies. The effects of CH_3OH, H_2O, CO_2, CO and H_2 partial pressures on the rate was then studied by varying inlet CH_3OH partial pressure from 1 to 10 kPa (Fig. 9a) and changing the inlet co-reactant (H_2O or CO_2) partial pressure from 0 to 10 kPa (while keeping CH_3OH partial pressure constant at 4 kPa) (Fig. 9b). The results show that the reaction rate was proportional to CH_3OH concentration with the reaction order of 0.50 (±0.04). The rate was unaffected by H_2O and CO_2 partial pressures, in contrast, it was inhibited by the presence of H_2 and CO in the feed. The reaction orders in

Table 4
Reaction rate and fraction of by-products from the H_2O reforming of CH_3OH on Ce-ZrO_2 (HSA) at several temperature and various inlet H_2O/CH_3OH ratios (3 kPa CH_3OH balance in He)

Temperature (K)	H_2O/CH_3OH ratio	CH_3OH reaction rate/$O_O{}^x$ (moles $mole^{-1}_{oxygen}$ s^{-1}) × 10^{-3}	Yield of H_2 production (%)	Fraction of by-products (%)		
				CO	CO_2	CH_4
923	0.0	1.21	24.5	46.6	17.5	35.9
973	0.0	2.77	34.9	68.1	16.7	15.2
1023	0.0	7.45	42.8	85.1	14.9	0
1023	1.0	7.44	44.1	77.2	22.8	0
1023	2.0	7.46	45.9	70.3	29.7	0
1023	3.0	7.42	47.7	64.2	35.8	0

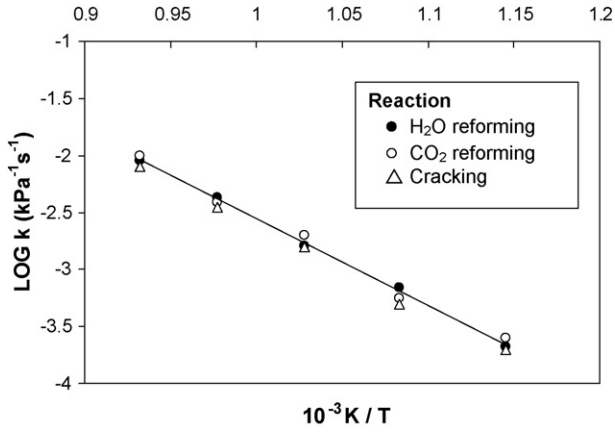

Fig. 10. Arrhenius plots for H_2O reforming, CO_2 reforming and cracking of CH_3OH over Ce-ZrO_2 (HSA).

H_2 and CO were between −0.28 (±0.01) and −0.13 (±0.02), respectively. The activation energies for H_2O reforming, CO_2 reforming and cracking of CH_3OH, achieved by the Arrhenius plots (Fig. 10), were 150–155 kJ/mol, which are closed to those observed from the CH_4 reactions. Therefore, based on the redox mechanistic proposal for CH_4 reaction, we suggested that the CH_3OH reaction mechanism over ceria-based materials could be written as followings:

$$CH_3OH + 2* \rightarrow CH_3* + OH* \quad (23)$$

$$CH_3* + 3* \rightarrow C* + 3H* \quad (24)$$

$$C* + O_O{}^x \rightarrow CO* + V_O{}^{\bullet\bullet} + 2e' \quad (25)$$

$$OH* + * \Leftrightarrow H* + O* \quad (26)$$

$$V_O{}^{\bullet\bullet} + 2e' + O* \Leftrightarrow O_O{}^x + * \quad (27)$$

CH_3OH first adsorbed on * forming intermediate surface hydrocarbon species (CH_x*) and OH* (Eq. (23)). Similar to CH_4 reforming, the intermediate surface hydrocarbons then adsorbed on the active surface site and reacted with the lattice oxygen ($O_O{}^x$) (Eqs. (24) and (25)). The steady-state reforming rate is due to the continuous supply of the oxygen containing compounds present in the system (i.e. H_2O, CO_2 and also CH_3OH) to regenerate the lattice oxygen ($O_O{}^x$). The dependence of the CH_3OH decomposition rate on CH_3OH partial pressure without the co-reactant requirement and its independence of the co-reactant partial pressures indicate that the lattice oxygen ($O_O{}^x$) is replenished by a sufficiently rapid reaction of the partially reduced state with the oxygen containing molecules in CH_3OH. The unchanged state of material was also confirmed by the calculation of oxygen balance during reactions and TPO after reactions.

The capability to decompose CH_3OH without requirement of steam is the great advantage of ceria-based materials for applying in SOFC system. Without the presence of steam being required, the consideration of water management in SOFC system is negligible and it is expected to simplify the overall SOFC system design, making SOFC more attractive to be used commercially.

3.5. Reactivity toward the high hydrocarbons (C_2H_4, C_2H_6, and C_3H_8) reforming

We again report here details only on Ce-ZrO_2 (HSA) sample, as the kinetic dependencies for these hydrocarbons were identical for all ceria-based materials. The feed was hydrocarbon (either C_2H_4, C_2H_6, or C_3H_8) and co-reactant (either H_2O or CO_2) in He. Catalyst reactivity and the product selectivities are given in Table 5. At 923 K, the main products from the reforming reactions were CH_4, H_2 CO, and CO_2. The formation of C_2H_4 was also observed toward the reforming of C_3H_8 and C_2H_6. From the studies, H_2 and CO selectivities increased with increasing temperature, whereas CO_2 and C_2H_4 selectivities decreased. The dependence of CH_4 selectivity on the operating temperature was non-monotonic; maximum CH_4 production occurred at approximately 1073 K (43.8%, 30.6% and 23.5% from steam reforming of C_2H_4, C_2H_6, and C_3H_8, respectively). These observations are in good agreement with our previous work, which studied the effect of temperature on the steam reforming of ethanol, ethane and ethylene over CeO_2 [49]. The decreases in CH_4 and C_2H_4 selectivities at higher temperature could be due to the further reforming to generate more CO and H_2. From the TPO testing, the amount of carbon deposited decreased with increasing inlet co-reactant concentration. At H_2O/hydrocarbons molar ratio higher than 3.0 and CO_2/hydrocarbons molar ratio higher than 5.0, no carbon formation was detected on the surface of Ce-ZrO_2 (HSA).

The influences of inlet component partial pressures on the reaction rate were then studied under the operating conditions without detectable carbon formation by changing the inlet

Table 5
Reaction rate and fraction of by-products from the H_2O and CO_2 reforming of C_nH_m on Ce-ZrO_2 (HSA) (923 K, 3 kPa C_nH_m and 15 kPa co-reactant, balance in He)

Reactant	Co-reactant	C_nH_m reaction rate/$O_O{}^x$	Yield of H_2 production (%)	Fraction of by-products (%)				Activation energy (kJ mol^{-1})
				C_2H_4	CH_4	CO	CO_2	
C_2H_4	H_2O	2.04[a]	26.7	–	40	48.2	11.8	150.4
	CO_2	2.10	15.5					151.9
C_2H_6	H_2O	2.85	29.9	9.3	28.6	49.2	12.9	148.6
	CO_2	2.78	18.4					147.5
C_3H_8	H_2O	5.39	34.3	18.6	20.3	48.5	12.6	145.0
	CO_2	5.44	22.1					149.7

[a] (moles $mole_{oxygen}^{-1}$ s^{-1}) × 10^{-3}.

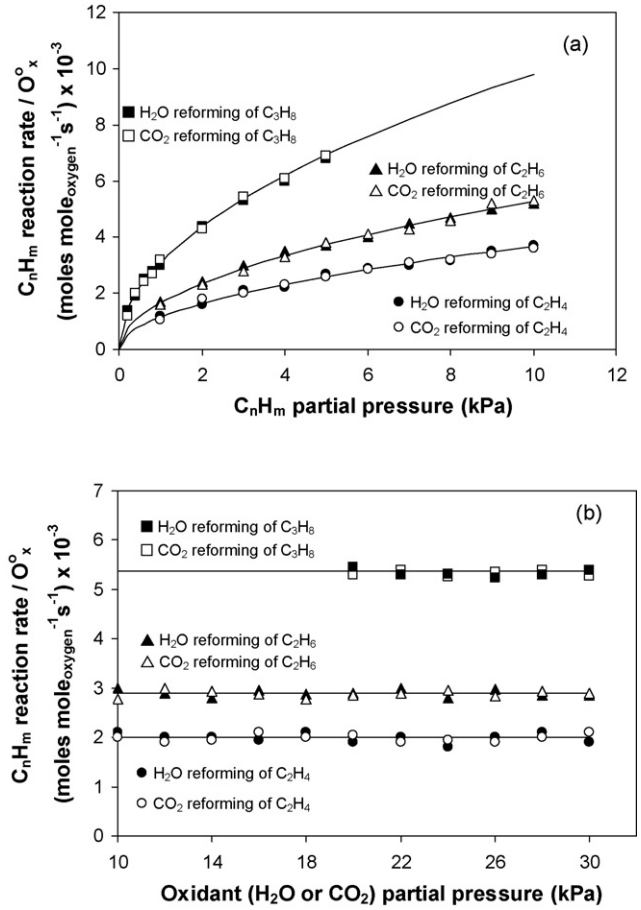

Fig. 11. Effects of C_nH_m partial pressures (a) and co-reactant partial pressure (b) on C_nH_m reaction rate (per moles of oxygen stored) over Ce-ZrO_2 (HSA) at 923 K.

hydrocarbon and co-reactant partial pressures as represented in Fig. 11a and b. Similar trends as CH_4 and CH_3OH reforming were observed. The reforming rate was proportional to the hydrocarbons concentration with the reaction orders in all hydrocarbons between 0.53 and 0.55. The rate was independent of inlet H_2O and CO_2 partial pressures, but it was inhibited by the presence of H_2 and CO in the feed. Fig. 12 shows the

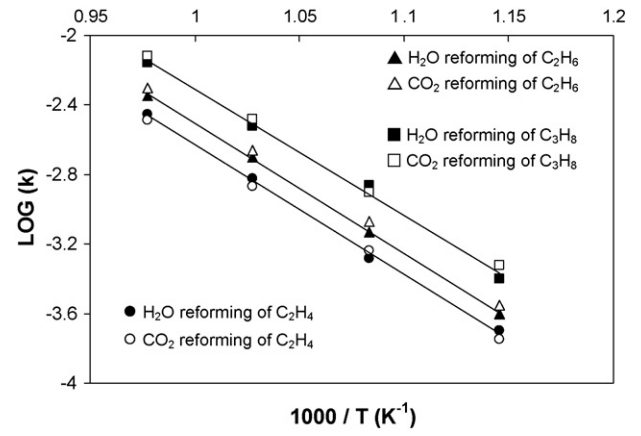

Fig. 12. Arrhenius plots for H_2O and CO_2 reforming of C_nH_m over Ce-ZrO_2 (HSA).

Arrhenius plots for both H_2O and CO_2 reforming of C_nH_m over Ce-ZrO_2 (HSA). The observed activation energies for these C_nH_m reactions were in the same range as achieved from the CH_4 and CH_3OH reactions (145–152 kJ mol^{-1}). Therefore, it can also be summarized that the mechanisms for H_2O and CO_2 reforming of high hydrocarbon are almost similar to those of CH_4 except that the adsorptions of these hydrocarbon elements (Eqs. (28–30)) are applied instead of the CH_4 adsorption. In addition, the reforming of high hydrocarbons requires considerably higher content of co-reactant at the feed in order to operate properly without the problem of carbon deposition.

$$C_3H_8 + 3* \rightarrow 2(CH_3*) + CH_2* \quad (28)$$

$$C_2H_6 + 2* \rightarrow 2CH_3* \quad (29)$$

$$C_2H_4 + 2* \rightarrow 7CH_2* \quad (30)$$

The capability to reform high hydrocarbon compounds with excellent resistance toward carbon deposition is another great benefit of ceria-based catalysts. Currently, natural gas and liquid petroleum gas (LPG) are the most promising primary fuels for the production of H_2 via reforming process. In order to reform these fuels, either an external pre-reforming unit or expensive noble metal catalysts (i.e. Rh) is normally required. By applying high surface area ceria-based materials as the reforming catalyst, all hydrocarbon elements can be reformed properly without the problem of carbon deposition eliminating the requirements of these costly processes.

4. Conclusion

High surface area CeO_2 and Ce-ZrO_2 provided higher CH_4, C_2H_4, C_2H_6, C_3H_8 and CH_3OH reforming rates with greater resistance toward carbon deposition than conventional Ce-ZrO_2 and CeO_2. The rates per amount of oxygen stored (moles $mol_{Oxygen}^{-1} s^{-1}$) on the surface of all ceria sample were in the same range, indicating the linear influence of OSC on the reaction rates. The kinetic dependencies of hydrocarbon conversions and the activation energies over these ceria-based materials were unaffected by the material specific surface area, doping element, degree of OSC and reactions. The rates were proportional to hydrocarbon partial pressures with positive fraction reaction order; independent of co-reactant partial pressures; but inhibited by CO and H_2. A set of unifying redox mechanistic proposal, in which the sole relevant elementary step is the reaction of intermediate surface hydrocarbon species with the lattice oxygen (O_O^x) and that oxygen is efficiently replenished by a rapid surface reaction with oxygen source in the system, was applied to explain these observed kinetic dependencies.

The capabilities to decompose oxyhydrocarbons without the requirement of steam and reform high hydrocarbon compounds with excellent resistance toward carbon deposition are the great benefit of ceria-based catalysts particularly for applying in SOFC system. Without the presence of steam being required, the consideration of water management in SOFC system is negligible, while the capability to reform high hydrocarbon

compounds with excellent resistance toward carbon deposition eliminates the requirement of expensive noble metal catalysts or the installation of external pre-reformer. These benefits simplify the overall SOFC system design, making SOFC more attractive for commercial uses.

Acknowledgements

The financial support from The Thailand Research Fund (TRF) throughout this project is gratefully acknowledged.

References

[1] A. Trovarelli, Catal. Rev. -Sci. Eng. 38 (1996) 439.
[2] P. Fornasiero, G. Balducci, R.D. Monte, J. Kaspar, V. Sergo, G. Gubitosa, A. Ferrero, M. Graziani, J. Catal. 164 (1996) 173.
[3] T. Miki, T. Ogawa, M. Haneda, N. Kakuta, A. Ueno, S. Tateishi, S. Matsuura, M. Sato, J. Phys. Chem. 94 (1990) 339.
[4] C. Padeste, N.W. Cant, D.L. Trimm, Catal. Lett. 18 (1993) 305.
[5] S. Kacimi, J. Barbier Jr., R. Taha, D. Duprez, Catal. Lett. 22 (1993) 343.
[6] G.S. Zafiris, R.J. Gorte, J. Catal. 143 (1993) 86.
[7] G.S. Zafiris, R.J. Gorte, J. Catal. 139 (1993) 561.
[8] S. Imamura, M. Shono, N. Okamoto, R. Hamada, S. Ishida, Appl. Catal. A 142 (1996) 279.
[9] E. Ramírez-Cabrera, A. Atkinson, D. Chadwick, Appl. Catal. B 47 (2004) 127.
[10] E. Ramírez-Cabrera, N. Laosiripojana, A. Atkinson, D. Chadwick, Catal. Today 78 (2003) 433.
[11] R.J. Gorte, J.M. Vohs, S. McIntosh, Solid State Ionics 175 (2004) 1.
[12] S. Jung, C. Lu, H. He, K. Ahn, R.J. Gorte, J.M. Vohs, J. Power Sources 154 (1) (2006) 42.
[13] T. Kim, G. Liu, M. Boaro, S.-I. Lee, J.M. Vohs, R.J. Gorte, O.H. Al-Madhi, B.O. Dabbousi, J. Power Sources 155 (2) (2006) 231.
[14] O. Costa-Nunes, R.J. Gorte, J.M. Vohs, J. Power Sources 141 (2005) 241.
[15] S. An, C. Lu, W.L. Worrell, R.J. Gorte, J.M. Vohs, Solid State Ionics 175 (2004) 135.
[16] D.J.L. Brett, A. Atkinson, D. Cumming, E. Ramírez-Cabrera, R. Rudkin, N.P. Brandon, Chem. Eng. Sci. 60 (2005) 5649.
[17] K. Otsuka, M. Hatano, A. Morikawa, J. Catal. 79 (1983) 493.
[18] K. Otsuka, M. Hatano, A. Morikawa, Inorg. Chim. Acta 109 (1985) 193.
[19] P.J. Gellings, H.J.M. Bouwmeester, Catal. Today 58 (2000) 1.
[20] D. Terribile, A. Trovarelli, J. Llorca, C. Leitenburg, G. Dolcetti, J. Catal. 178 (1998) 299.
[21] E. Abi-aad, R. Bechara, J. Grimblot, A. Aboukaïs, Chem. Mater. 5 (1993) 793.
[22] L.A. Bruce, M. Hoang, A.E. Hughes, T.W. Turney, Appl. Catal. A 134 (1996) 351.
[23] P.L. Chen, I.W. Chen, J. Am. Ceram. Soc. 76 (1993) 1577.
[24] H.K. Varma, P. Mukundam, K.G.K. Warrier, A.D. Damodaran, J. Mater. Sci. Lett. 10 (1991) 666.
[25] M. Hirano, E. Kato, J. Am. Ceram. Soc. 79 (1996) 777.
[26] M. Vallet-Regi, F. Conde, S. Nicolopoulos, C.V. Ragel, J.M. Gonzales-Calbet, Mater. Sci. Forum 235–238 (1997) 291.
[27] A. Tschöpe, J.Y. Ying, NanoStruct. Mater. 4 (1994) 617.
[28] M. Pijolat, J.P. Viricelle, M. Soustelle, Stud. Surf. Sci. Catal. 91 (1995) 885.
[29] T. Masui, K. Fujiwara, K. Machida, G. Adachi, T. Sakata, H. Mori, Chem. Mater. 9 (1997) 2197.
[30] Y. Zhou, R.J. Phillips, J.A. Switzer, J. Am. Ceram. Soc. 78 (1995) 981.
[31] V. Perrichon, A. Laachir, S. Abouarnadasse, O. Touret, G. Blanchard, Appl. Catal. A 129 (1995) 69.
[32] D. Terribile, A. Trovarelli, J. Llorca, C. Leitenburg, G. Dolcetti, Catal. Today 43 (1998) 79.
[33] M. Ozawa, M. Kimura, A. Isogai, J. Alloys Comp. 193 (1993) 73.
[34] G. Balducci, J. Kaspar, P. Fornasiero, M. Graziani, M.S. Islam, J. Phys. Chem. B 102 (1998) 557.
[35] G. Vlaic, P. Fornasiero, S. Geremia, J. Kaspar, M. Graziani, J. Catal. 168 (1997) 386.
[36] G.R. Rao, J. Kaspar, S. Meriani, R. Dimonte, M. Graziani, Catal. Lett. 24 (1994) 107.
[37] P. Fornasiero, R. Dimonte, G.R. Rao, J. Kaspar, S. Meriani, A. Trovarelli, M. Graziani, J. Catal. 151 (1995) 168.
[38] M.H. Yao, T.E. Hoost, R.J. Baird, F.W. Kunz, J. Catal. 166 (1997) 67.
[39] D. Kim, J. Am. Ceram. Soc. 72 (1989) 1415.
[40] N. Laosiripojana, W. Sutthisripok, S. Assabumrungrat, Chem. Eng. J. 127 (13) (2007) 36.
[41] N. Kruse, A. Frennet, J.M. Bastin (Eds.), Catalysis and Automotive Pollution Control IV, Elsevier, Amsterdam, 1998.
[42] J. Kaspar, P. Fornasiero, M. Graziani, Catal. Today 50 (1999) 285.
[43] H.S. Roh, H.S. Potdar, K.W. Jun, Catal. Today 93–95 (2004) 39.
[44] J. Wei, E. Iglesia, J. Catal. 225 (2004) 116.
[45] N. Laosiripojana, S. Assabumrungrat, Appl. Catal. A 290 (2005) 200.
[46] N. Laosiripojana, S. Assabumrungrat, Appl. Catal. B 60 (2005) 107.
[47] Y. Lwin, W.R.W. Daud, A.B. Mohamad, Z. Yaakob, Int. J. Hydrogen Energy 25 (2000) 47.
[48] J.N. Amor, Appl. Catal. A 176 (1999) 159.
[49] N. Laosiripojana, S. Assabumrungrat, Appl. Catal. B 66 (2006) 29.

Chemical Engineering Science 64 (2009) 459 – 466

Contents lists available at ScienceDirect

Chemical Engineering Science

journal homepage: www.elsevier.com/locate/ces

Reactivity of CeO_2 and $Ce–ZrO_2$ toward steam reforming of palm fatty acid distilled (PFAD) with co-fed oxygen and hydrogen

A. Shotipruk[a], S. Assabumrungrat[a], P. Pavasant[a,c], N. Laosiripojana[b,*]

[a]Department of Chemical Engineering, Faculty of Engineering, Chulalongkorn University, Bangkok, Thailand
[b]The Joint Graduate School of Energy and Environment, King Mongkut's University of Technology Thonburi, Bangkok 10140, Thailand
[c]National Center of Excellence for Environmental and Hazardous Waste Management, Chulalongkorn University, Bangkok 10330, Thailand

ARTICLE INFO

Article history:
Received 14 June 2008
Received in revised form 30 August 2008
Accepted 3 September 2008
Available online 4 October 2008

Keywords:
Ceria
Hydrogen
Oxygen storage capacity
Steam reforming
Autothermal reforming
Palm fatty acid distillate

ABSTRACT

Steam reforming of three types free fatty acids (i.e. palmitic, oleic and linoleic acids) and palm fatty acid distilled (PFAD) were studied over ceria-based materials prepared by precipitation and cationic surfactant-assisted methods with/without Zr doping with an aim to develop good reforming catalyst for converting PFAD to hydrogen with high reforming reactivity and low carbon deposition. Among all catalysts, high surface area (HSA) $Ce–ZrO_2$ (with Ce/Zr ratio of 3/1) prepared by cationic surfactant-assisted method provided the highest steam reforming reactivity with greatest resistance toward carbon deposition; due to the high oxygen storage capacity (OSC) of this material. During steam reforming, the redox reactions between absorbed hydrocarbons (forming intermediate surface hydrocarbon species) with lattice oxygen (O_0^x) at $Ce–ZrO_2$ surface take place. The rapid redox reactions between surface carbon (C^*) forming via the adsorptions of hydrocarbon with lattice oxygen (O_0^x) prevents the formation of carbon species from decomposition of hydrocarbons. At 1173 K, the main products from the steam reforming of PFAD over this catalyst are H_2, CO, and CO_2 with some amounts of CH_4 and C_2H_4 generated; the formations of these high hydrocarbons can be eliminated by increasing temperature up to 1273 K.

The addition of either oxygen or hydrogen together with PFAD and steam considerably reduced the degree of carbon deposition. The presence of oxygen also reduced the formations of hydrocarbons, on the other hand, these formations increased when hydrogen was introduced at the feed. The negative effect of hydrogen is due to hydrogenation reaction as well as the reduction of lattice oxygen by hydrogen, which consequently inhibits the reaction of lattice oxygen with surface hydrocarbon species.

1. Introduction

According to the current oil crisis and the shortage of fossil fuels, the development of the biomass-based fuels (or biofuel) attracts much attention. Nowadays, one of the most practical biofuels is biodiesel, which are produced from palm oil. It should be noted that, recently, there are also several attempts to convert lignocellulosic biomass to biofuels (i.e. BTL); this conversion will reduce the competition of fuel with food market, which results in the food shortage and the rising of food price. Nevertheless, this technology remains need further development to achieve high efficiency.

Focusing on palm oil, over the past 10 years, this compound has become one of the attractive resources for biodiesel production since it constitutes a renewable and sustainable source of energy. Importantly, palm oil always contain high amount of free fatty acid (FFA) and the presence of too high FFA easily results in high amounts of soap produced simultaneously with the transesterification reaction. Therefore, to avoid this reaction, most of FFA in palm oil must be firstly processed or removed (as called palm fatty acid distilled or PFAD). The conversion of this removed PFAD to valuable products or fuels (e.g. fatty acid methyl esters via esterification or even hydrogen) is an alternative way to reduce the cost for biodiesel production and consequently make biodiesel enable to compete economically with conventional petroleum diesel fuels. Among the prospective fuels, hydrogen is expected to be one of the most promising fuels in the near future. It is known as the zero-emission fuel and could be produced efficiently from the catalytic reforming of several hydrocarbon sources such as methane, methanol, bio-ethanol, gasoline and other oil derivatives. On this basis, the production of hydrogen from PFAD will provide the great benefit in terms of energy, environmental, and economical aspects.

Focusing on catalytic reforming process, steam reforming of several oxygenated hydrocarbons, e.g. methanol, acetic acid, ethanol, acetone, phenol or cresol as model compounds of bio-oils has widely

* Corresponding author. Tel.: +66 2 8729014; fax: +66 2 8726736.
E-mail address: navadol_l@jgsee.kmutt.ac.th (N. Laosiripojana).

0009-2509/$ - see front matter © 2008 Elsevier Ltd. All rights reserved.
doi:10.1016/j.ces.2008.09.013

been investigated (Basagiannis and Verykios, 2006; Galdámez et al., 2005; Czernik et al., 2004; Wang et al., 1997, 1996; Polychronopoulou et al., 2004; Takanabe et al., 2004; Fatsikostas et al., 2002; Liguras et al., 2003). Recently, many researchers have also investigated the addition of oxygen together with steam in a single process, calling an autothermal reforming, in order to reduce the degree of carbon formation as well as provide the thermal self-sustaining process. Until now, no literature work has reported the conversion fatty acids or PFAD to hydrogen by the catalytic reforming process; only few works have presented the catalytic reforming or cracking of acetic acid to hydrogen (Basagiannis and Verykios, 2007, in press; Davidian et al., 2008). PFAD normally consists mainly of palmitic acid ($C_{16}H_{32}O_2$; $CH_3(CH_2)_{14}COOH$), oleic acid ($C_{18}H_{34}O_2$; $CH_3(CH_2)_7CH=CH(CH_2)_7COOH$) and linoleic acid ($C_{18}H_{32}O_2$; $CH_3(CH_2)_4CH=CHCH_2CH=CH(CH_2)_7CO_2H$) with various ratios depending on the source of palm oils. The major difficulty to reform high hydrocarbon compounds like PFAD is the possible deactivation of the reforming catalyst due to the carbon deposition, as fatty acids can decompose homogenously and form carbon species on the surface of catalyst. In addition, from its thermal decomposition, several gaseous hydrocarbon elements, which act as very strong promoters for carbon formation, can be formed. Worldwide efforts are in progress to explore a novel catalyst with high activity and stability for the reforming of heavy hydrocarbon compounds.

Recently, it is established that ceria and metal oxide (e.g. Gd, Nb, and Zr) doped cerias provide high oxygen storage capacity (OSC), which is beneficial in oxidation and reforming processes (Ramirez et al., 2002). The great benefit of ceria-based catalysts for the reforming reaction is their high resistance toward carbon deposition compared to the conventional metal catalysts i.e. Ni (Ramírez-Cabrera et al., 2003; Terribile et al., 1998a); however, the main weaknesses of the materials are their low specific surface area and high deactivation due to the thermal sintering particularly when operated at such a high temperature (Terribile et al., 1998a). The preparation and use of high surface area (HSA) ceria (CeO_2, HSA) with high resistance toward the sintering would be a good alternative method to improve the catalytic reactivity (Terribile et al., 1998a). Recently, Terribile et al. (1998b) synthesized CeO_2 (HSA) with improved textural, structural and chemical properties for environmental applications by using a novel cationic surfactant-assisted approach. They reported that the reaction of cerium salts under basic conditions with ammonia in the presence of a cationic surfactant results in the precipitation of a gelatinous hydrous cerium oxide/surfactant mixture, which after calcination gives HSA, fluorite-structured CeO_2 with good homogeneity and stability. They suggested that the cationic surfactant acts as a surface area enhancer by incorporation into the hydrous oxide and lowering of the surface tension of water in the pores during drying.

In addition to the investigation on preparation method, the addition of zirconium oxide (ZrO_2) has also been reported to improve the specific surface area, OSC, redox property, thermal stability and catalytic activity of ceria (Ozawa et al., 1993; Balducci et al., 1998; Vlaic et al., 1997; Rao et al., 1994; Fornasiero et al., 1995; Yao et al., 1997). These benefits were associated with enhanced reducibility of cerium (IV) in Ce–ZrO_2, which is a consequence of high O^{2-} mobility inside the fluorite lattice. The reason for the increasing mobility might be related to the lattice strain, which is generated by the introduction of a smaller isovalent Zr cation into the CeO_2 lattice (Zr^{4+} has a crystal ionic radius of 0.84 å, which is smaller than 0.97 å for Ce^{4+} in the same co-ordination environment) (Kim, 1989).

In the present work, it is aimed to develop the reforming catalysts that can convert PFAD to hydrogen with high reforming activity and great resistance toward carbon formation. CeO_2 and Ce– ZrO_2 prepared by two different methods i.e. typical (co-) precipitation and cationic surfactant-assisted methods were selected as the catalyst in the present work. The steam reforming of palmitic acid, oleic acid and linoleic acid (as main components in PFAD) over these catalysts were firstly studied and compared to conventional Ni/Al_2O_3. The steam reforming of PFAD over selected catalyst was then carried out. The effects of temperature, oxygen adding and hydrogen adding on the reforming reactivity were also investigated. Lastly, the possible mechanism for steam reforming of PFAD over ceria-based catalysts was discussed.

2. Experimental methods

2.1. Raw material and chemicals

In the present work, palm fatty acid distillate (PFAD) was obtained from Chumporn Palm Oil Industry Public Company Limited., Thailand. It consists of 93 wt% FFA (mainly contains 46% palmitic acid, 34% oleic acid and 8% linoleic acid with small amount of other fatty acids i.e. stearic, myristic, tetracosenoic, linolenic, ecosanoic, ecosenoic, and palmitoleic acid). The rest elements are triglycerides, diglycerides (DG), monoglycerides (MG) and traces of impurities. The lab grade palmitic acid, oleic acid, and linoleic acid were supplied from Aldrich.

2.2. Material synthesis and characterization

In the present work, CeO_2 was synthesized by precipitation (CeO_2 (LSA)) and cationic surfactant-assisted (CeO_2 (HSA)) methods. CeO_2 (LSA) was prepared by the precipitation of cerium nitrate ($Ce(NO_3)_3 \cdot H_2O$) from Aldrich. The starting solution was prepared by slowly adding of 0.4 M ammonia (with flow rate of 0.254 $cm^3\,h^{-1}$) to 0.1 M of cerium nitrate solution until reaching volumetric ratio of 2:1. This solution was stirred by magnetic stirring (100 rpm) for 3 h, then sealed and placed in a thermostatic bath maintained at 363 K for 3 days to prevent an agglomeration of the particles. The precipitate was filtered and washed with deionized water and acetone to remove the free surfactant. It was dried overnight in an oven at 383 K, and then calcined at 1173 K for 6 h. Following to the work from Terribile et al. (1998b), CeO_2 (HSA) were prepared by adding an aqueous solution of the appropriate cationic surfactant, 0.1 M cetyltrimethylammonium bromide solution from Aldrich, to a 0.1 M cerium nitrate. The molar ratio of ([Ce])/[cetyltrimethylammonium bromide] was kept constant at 0.8. The mixture was stirred and then aqueous ammonia was slowly added with vigorous stirring until the pH was 11.5 (Terribile et al., 1998b). After treatment with the same procedure as CeO_2 (LSA), fluorite-structured CeO_2 with good homogeneity were obtained.

$Ce_{1-x}Zr_xO_2$ (or Ce–ZrO_2) with different Ce/Zr molar ratios were also prepared by either co-precipitation or surfactant-assisted method of cerium nitrate ($Ce(NO0_3)_3 \cdot H_2O$), and zirconium oxychloride ($ZrOCl_2 \cdot H_2O$) (from Aldrich). The ratio between each metal salt was altered to achieve nominal Ce/Zr molar ratios: $Ce_{1-x}Zr_xO_2$, where $x = 0.25$, 0.50, and 0.75, respectively. After treatment, the specific surface areas of all CeO_2 and Ce–ZrO_2 were achieved from BET measurement. As presented in Table 1, after drying in the oven,

Table 1
Specific surface area of CeO_2 and Ce–ZrO_2 before and after calcination at 1173 K

Catalysts	Surface area after drying ($m^2\,g^{-1}$)	Surface area after calcination ($m^2\,g^{-1}$)
CeO_2 (HSA)	105	29
Ce–ZrO_2 (HSA) (Ce/Zr = 1/3)	135	49
Ce–ZrO_2 (HSA) (Ce/Zr = 1/1)	120	47
Ce–ZrO_2 (HSA) (Ce/Zr = 3/1)	115	46.5
CeO_2 (LSA)	55	11
Ce–ZrO_2 (LSA) (Ce/Zr = 1/3)	82	22
Ce–ZrO_2 (LSA) (Ce/Zr = 1/1)	74	20.5
Ce–ZrO_2 (LSA) (Ce/Zr = 3/1)	70	20

Table 2
Physicochemical properties of Ni/Al_2O_3 after reduction

Catalyst	Metal-load[a] (wt%)	BET surface area ($m^2\,g^{-1}$)	Metal-reducibility[b] (%)	Metal-dispersion[c] (%)
Ni/Al_2O_3	4.9	40	92.1	4.87

[a]Measured from X-ray fluorescence analysis.

[b]Measured from temperature-programmed reduction (TPR) with 5% hydrogen.

[c]Measured from temperature-programmed desorption (TPD) of hydrogen after TPR measurement.

surface areas of 105 and 55 $m^2\,g^{-1}$ were observed for CeO_2 (HSA) and CeO_2(LSA), respectively, and, as expected, the surface area decreased at high calcination temperatures. However, the value for CeO_2 (HSA) is still appreciable after calcination at 1173 K. The achievement of HSA material by surfactant-assisted procedure is due to the interaction of hydrous oxide with cationic surfactants under basic conditions during the preparation (Terribile et al., 1998b). At high pH value, conducting the precipitation of hydrous oxide in the presence of cationic surfactant allows cation exchange process between H^+ and the surfactant, resulting in a developed pore structure with an increase in surface area (Terribile et al., 1998b). It can also be seen that the introduction of ZrO_2 stabilizes the surface area of ceria, which is in good agreement with several previous reports (Kruse et al., 1998; Kaspar et al., 1999; Roh et al., 2004).

For comparison, Ni/Al_2O_3 (5 wt% Ni) was also prepared by impregnating γ-Al_2O_3 (from Aldrich) with $Ni(NO_3)_2$ solution (from Aldrich). After stirring, the solution was dried and calcined at 1173 K for 6 h. The catalyst powder was reduced with 10% H_2/Ar at 773 K for 6 h before use. After reduction, Ni/Al_2O_3 was characterized by several physicochemical methods. The weight contents of Ni were determined by X-ray fluorescence (XRF) analysis. The reducibility percentage of nickel was measured and calculated from the degree of H_2 uptakes from temperature-programmed reduction (TPR) test using 5% H_2 with the total flow rate of 100 $cm^3\,min^{-1}$ and temperature from room temperature to 773 K, while the dispersion percentage of nickel was identified from temperature-programmed desorption (TPD) by measuring the volumetric H_2 chemisorbed. All physicochemical properties of the synthesized catalysts are presented in Table 2.

2.3. Apparatus and procedures

To undergoing the catalytic testing, an experimental reactor system was constructed. The feed including palmitic acid, oleic acid and linoleic acid, PFAD and deionized H_2O was introduced via a heated syringe pump passing through our design quartz vaporizer-mixer system, where the inlet fatty acids are injected as droplet before vaporized and mixed with steam/carrier gas. All inlet components were introduced to a 10-mm diameter quartz reactor, which is mounted vertically inside tubular furnace. The catalyst (100 mg) was loaded in the quartz reactor, which was packed with a small amount of quartz wool to prevent the catalyst from moving. Preliminary experiments were carried out to find suitable conditions in which internal and external mass transfer effects are not predominant. Considering the effect of external mass transfer, the total gas flow rate was varied between 10 and 150 $cm^3\,min^{-1}$ under a constant residence time of 10^{-3} g min cm^{-3}. It was found that the reforming rate was independent of gas velocity when the gas flow rate was higher than 70 $cm^3\,min^{-1}$, indicating the absence of external mass transfer effects at this high velocity. Furthermore, the reactions on different average sizes of catalysts (up to 500 μm) were carried out to confirm that the experiments were in the region of intrinsic kinetics. It was observed that the catalysts with the particle size less than 200 μm showed no intraparticle diffusion limitation in the range of conditions studied. Therefore, the total flow rate was kept constant at 100 $cm^3\,min^{-1}$ whereas catalyst diameter was between 100 and 200 μm in all experiments.

In our system, a Type-K thermocouple was placed into the annular space between the reactor and the furnace. This thermocouple was mounted on the tubular reactor in close contact with the catalyst bed to minimize the temperature difference between the catalyst bed and the thermocouple. Another Type-K thermocouple was inserted in the middle of the quartz tube in order to re-check the possible temperature gradient. It is noted that the inner-system thermocouple is covered with small closed-end quartz rod to prevent the catalytic reactivity of thermocouple during reaction. After the reactions, the exit gas mixture was transferred via trace-heated lines to the analysis section, which consists of a Porapak Q column Shimadzu 14B gas chromatograph (GC) and a mass spectrometer (MS). The MS in which the sampling of the exit gas was done by a quartz capillery and differential pumping was used for the transient and carbon formation experiments, whereas the GC was applied in order to investigate the steady-state condition experiments and to recheck the results from MS. In the present work the reactivity of catalyst toward the reaction was defined in terms of hydrogen and other gaseous hydrocarbon by-product selectivities (based on carbon balance).

2.4. Measurement of carbon formation

In order to investigate the amount of carbon formed on catalyst surface, the oxidation reaction was applied by introducing 10% O_2 in helium into the system at isothermal condition (1173 K), after purging the system with helium. The amount of carbon formation on the surface of catalysts was determined by measuring the areas under peak of CO and CO_2 from the test compared with those from the calibrations of these components. It is noted that the calibrations of CO and CO_2 were performed by injecting a known amount of these calibration gases from a loop, in an injection valve in the bypass line.

3. Results and discussion

3.1. Redox properties and redox reversibility

After treatment, the degrees of OSC for fresh ceria-based materials were investigated using reduction measurement (R-1), which was performed by purging the catalysts with 5% H_2 in helium at 1173 K. The amount of H_2 uptake is correlated to the amount of oxygen stored in the catalysts. As presented in Table 3, the amount of H_2 uptakes over HSA Ce–ZrO_2 and CeO_2 are significantly higher than those over the low surface area cerias, suggesting the increasing of OSC with the doping of Zr and the increasing of material specific surface area. The benefit of OSC on the reforming reaction will be later presented in Section 4. After purged with helium, the redox

Table 3
R-1, Ox-1, R-2 analyses of ceria-based materials after calcination

Catalyst	Total H_2 uptake from R-1 ($\mu mol/g_{cat}$)[a]	Total O_2 uptake from Ox-1 ($\mu mol/g_{cat}$)[a]	Total H_2 uptake from R-2 ($\mu mol/g_{cat}$)[a]
CeO_2 (HSA)	4087	2012	4077
Ce–ZrO_2 (HSA) (Ce/Zr = 1/3)	2883	1423	2879
Ce–ZrO_2 (HSA) (Ce/Zr = 1/1)	3692	1848	3687
Ce–ZrO_2 (HSA) (Ce/Zr = 3/1)	5221	2620	5213
CeO_2 (LSA)	1789	884	1780
Ce–ZrO_2 (LSA) (Ce/Zr = 1/3)	1087	551	1075
Ce–ZrO_2 (LSA) (Ce/Zr = 1/1)	1701	709	1694
Ce–ZrO_2 (LSA) (Ce/Zr = 3/1)	2625	1305	2621

[a]Deviation = ±3%

Table 4
Hydrogen selectivity and distribution of other gaseous by-products from the steam reforming of fatty acids over several catalysts at 1173 K

Fuel	Catalyst	Hydrogen selectivity (%)	Distribution of the by-products (%)					
			CO	CO_2	CH_4	C_2H_6	C_2H_4	C_3H_6
Palmitic acid	Ce– ZrO_2 (HSA)	71.8	24.1	44.7	25.4	1.9	3.7	0.2
	CeO_2 (HSA)	68.3	21.4	39.1	30.7	2.5	5.8	0.5
	Ce–ZrO_2 (LSA)	62.7	19.2	38.6	31.7	3.3	6.3	0.9
	CeO_2 (LSA)	54.9	18.1	35.5	34.8	3.5	7.1	1.0
Oleic acid	Ce– ZrO_2 (HSA)	69.2	22.2	40.9	28.3	2.5	5.3	0.8
	CeO_2 (HSA)	61.9	19.1	38.2	33.8	2.6	5.4	0.9
	Ce–ZrO_2 (LSA)	60.4	18.9	37.6	33.3	2.9	6.7	0.6
	CeO_2 (LSA)	52.3	17.4	32.2	36.4	3.9	8.9	1.2
Linoleic acid	Ce– ZrO_2 (HSA)	67.4	21.8	39.5	27.6	3.8	5.9	1.4
	CeO_2 (HSA)	63.8	20.1	37.5	29.0	3.7	8.5	1.2
	Ce–ZrO_2 (LSA)	57.8	19.7	36.1	30.2	3.9	8.7	1.4
	CeO_2 (LSA)	51.5	18.7	32.0	35.1	3.7	9.2	1.3
Palmitic acid	Ni/Al_2O_3	65.5	29.8	40.1	22.2	3.9	9.8	1.4

reversibilities were then determined by applying oxidation measurement (Ox-1) following with second time reduction measurement (R-2). The amounts of O_2 chemisorbed and H_2 uptake are presented in Table 3. Regarding the results as also shown in Table 3, the amount of hydrogen uptakes for all materials were approximately identical to those from the R-1, indicating the reversibility of OSC for these synthesized ceria-based materials.

3.2. Reactivity toward the steam reforming of fatty acids

Before undergoing the tests on PFAD, the steam reforming of palmitic acid, oleic acid and linoleic acid were firstly investigated as these three hydrocarbons are the main components in PFAD. The experiments were carried out at 1173 K by introducing each fatty acid along with steam as co-reactant. It should be noted that the reactions for Ce–ZrO_2 with different Ce/Zr ratios (1/3, 1/1, and 3/1) were preliminary done over palmitic acid and the results revealed that Ce–ZrO_2 with Ce/Zr ratio of 3/1 synthesized from both techniques shows the best performance in terms of stability, activity and product selectivities. Therefore, we report here detailed reactivity of Ce– ZrO_2 only with Ce/Zr ratio of 3/1.

Table 4 presents the summarize of gaseous product distribution from the steam reforming of palmitic acid, oleic acid and linoleic acid over CeO_2 and Ce–ZrO_2 prepared by two techniques, while Fig. 1 shows the variations in hydrogen selectivity (%) with time (under the period of 48 h) from the steam reforming of palmitic acid over these catalysts. It is noted that the product distribution in the present work is reported in term of selectivity, as the conversion of fatty acids is always 100% in the range of conditions studied. It can be seen from Fig. 1 that no significant deactivation was detected from these four catalysts indicating their good stability toward the reactions. From Table 4, apart from H_2, CO, and CO_2 productions, significant amount of CH_4, C_2H_4, C_2H_6, and C_3H_6 were also detected from the reactions. The production of CO_2 indicates the contribution of the water–gas shift at this high temperature, while the presenting of gaseous hydrocarbons (i.e. CH_4, C_2H_4, C_2H_6, and C_3H_6) comes from the decomposition of these fatty acids Eq. (1) in the Discussion section). Between these three fatty acids, palmitic acid provides highest hydrogen production, whereas hydrogen production from oleic acid is slightly higher than that from linoleic acid. Furthermore, compared between four catalysts (CeO_2 (HSA), CeO_2 (LSA), Ce– ZrO_2 (HSA), and Ce–ZrO_2 (LSA)), Ce–ZrO_2 (HSA) presents the highest hydrogen production with considerably lower formations of CH_4, C_2H_4, C_2H_6, and C_3H_6. It should be noted that, for comparison, the steam reforming of palmitic acid over conventional Ni/Al_2O_3 was tested at 1173 K. As

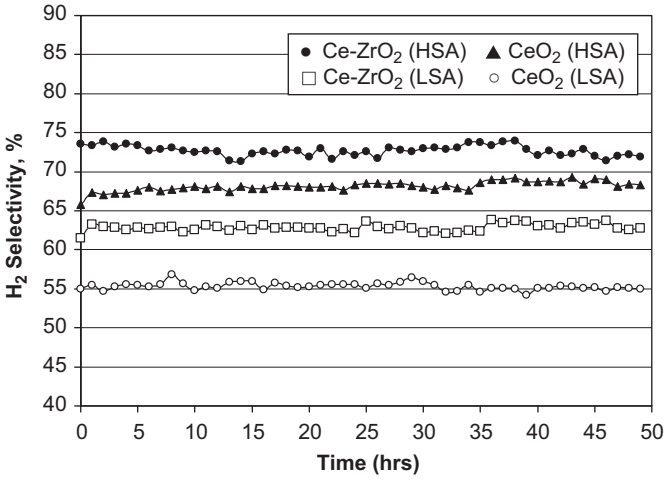

Fig. 1. Variation in hydrogen selectivities with time from steam reforming of palmitic acid at 1173 K over several catalysts.

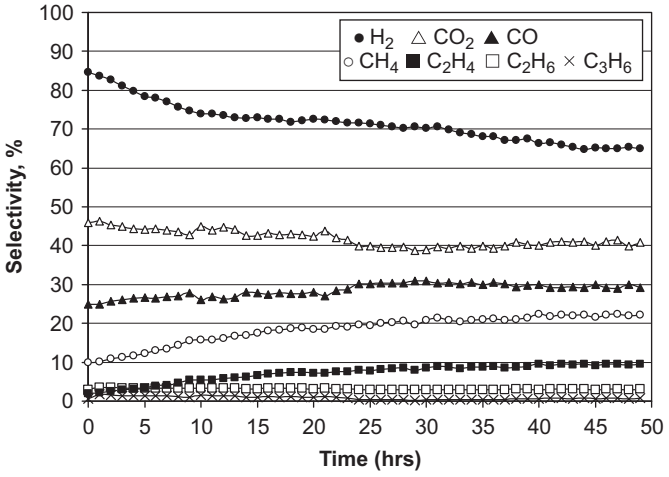

Fig. 2. Variations in hydrogen and other gaseous product selectivities with time from steam reforming of palmitic acid at 1173 K over Ni/Al_2O_3.

seen in Fig. 2, unstable profiles of hydrogen production yield, which related to the formation of carbon species on the surface of catalyst, were observed.

Table 5
Amount of carbon deposition on the surface of each catalyst after exposure in the steam reforming of fatty acids at 1173 K for 48 h

Fuel	Catalyst	Carbon formation (mmol g_{cat}^{-1})
Palmitic acid	Ce– ZrO_2 (HSA)	5.0
	CeO_2 (HSA)	5.3
	Ce–ZrO_2 (LSA)	5.9
	CeO_2 (LSA)	6.4
Oleic acid	Ce– ZrO_2 (HSA)	5.1
	CeO_2 (HSA)	5.5
	Ce–ZrO_2 (LSA)	6.4
	CeO_2 (LSA)	6.9
Linoleic acid	Ce– ZrO_2 (HSA)	5.4
	CeO_2 (HSA)	5.5
	Ce–ZrO_2 (LSA)	6.6
	CeO_2 (LSA)	7.0
Palmitic acid	Ni/Al_2O_3	9.5

After purging in helium, the post-reaction oxidation experiments were carried out by introducing of 10% oxygen in helium to determine the amount of carbon formation occurred in the system. The oxidation measurement detected some amount of carbon on the surface of ceria-based catalysts (between 5.0 and 5.5 mmol g_{cat}^{-1} for HSA materials and between 5.9 and 7.0 mmol g_{cat}^{-1} for low surface area one), whereas significantly higher amount of carbon was found over Ni/Al_2O_3, Table 5, indicating the greater resistance toward carbon deposition of ceria-based catalysts. The explanation for the steam reforming reactivity of ceria-based catalysts with high resistance toward carbon deposition will be given in the Discussion section.

3.3. Reactivity toward the steam reforming of PFAD

From the results in Section 3.1, among all ceria-based catalysts, Ce– ZrO_2 (HSA) with Ce/Zr ratios of 3/1 showed the greatest reactivities toward the steam reforming of palmitic acid, oleic acid and linoleic acid. Therefore, it was chosen for the further study to investigate the reactivity toward the steam reforming of PFAD. Instead of individual fatty acid, the feed was PFAD/H_2O in helium with the steam/carbon ratio of 3.0. It is noted that, before studying the catalyst performance, homogeneous (non-catalytic) steam reforming of PFAD (with above steam/carbon ratio) was also investigated at 1123 K. It was found that at this temperature PFAD were all homogeneously converted to $CH_4, C_2H_6, C_2H_4, C_3H_6$, CO, CO_2 and H_2 (with H_2 selectivity of 41.3% and $CH_4, C_2H_6, C_2H_4, C_3H_6$, CO, CO_2 selectivities of 22.3, 10.3, 16.8, 5.0, 16.4, 29.2%, respectively). It should also be noted that significant amount of carbon was also detected in the blank reactor after exposure for 10 h.

As for the catalyst testing, the variations in hydrogen production and gaseous by-product selectivities with time from the steam reforming of PFAD over Ce– ZrO_2 at 1123 K are shown in Fig. 3. Similar trend as all three fatty acids was observed; the main products are H_2, CO, and CO_2 with some amounts of CH_4, C_2H_4, C_2H_6, and C_3H_6. The post-reaction oxidation measurement indicated that the amount of carbon deposition on the surface of Ce–ZrO_2 after exposure in reforming condition for 48 h is 5.1 mmol g_{cat}^{-1}. As the next step, the effects of inlet steam/carbon ratio and temperature on the reforming reactivity were then studied by varying the inlet steam/carbon ratio from 3.0 to 5.0, 7.0, 9.0 and 11.0, and increasing the operating temperature from 1173 to 1198, 1223, 1248 and 1273 K. Fig. 4 presents the effect of inlet steam/carbon ratio on the hydrogen production and other by-product selectivities (after held the system for 10 h at each condition to ensure that the reaction reactivity is stable), whereas Table 6 presents the degree of carbon deposition observed from the post-reaction oxidation measurement.

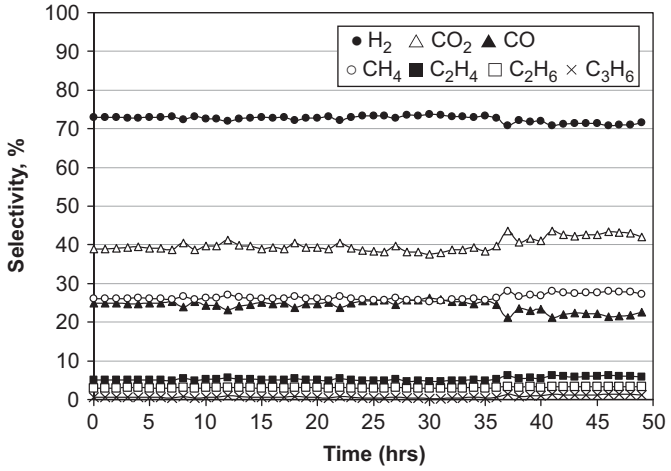

Fig. 3. Variations in hydrogen and other gaseous product selectivities with time from steam reforming of PFAD at 1173 K over Ce–ZrO_2 with Ce/Zr ratio of 3/1.

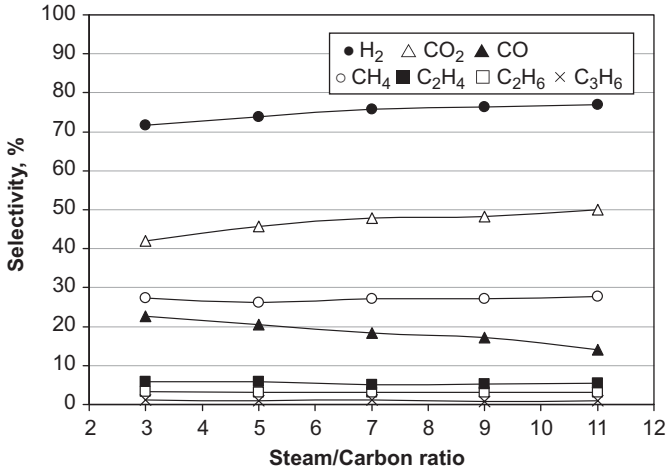

Fig. 4. Effect of inlet steam/carbon molar ratio on gaseous product selectivities from steam reforming of PFAD at 1173 K over Ce–ZrO_2 with Ce/Zr ratio of 3/1.

Table 6
Effects of inlet steam/carbon molar ratio and temperature on the degree of carbon formation after exposure in steam reforming of PFAD for 10 h

Catalyst	Steam/carbon molar ratio	Temperature (K)	Carbon formation (mmol g_{cat}^{-1})
Ce–ZrO_2 (Ce/Zr = 3/1)	3.0	1173	5.1
	5.0	1173	5.0
	7.0	1173	5.2
	9.0	1173	5.1
	11.0	1173	5.0
	3.0	1198	4.7
	3.0	1223	4.3
	3.0	1248	3.9
	3.0	1273	3.5

It can be seen that hydrogen and carbon dioxide increase with increasing steam content, whereas carbon monoxide decreases; this could be mainly due to the contribution of the water gas shift reaction. Nevertheless, all hydrocarbon (CH_4, C_2H_4, and C_2H_6) selectivities remain unchanged with increasing steam content and the amount of carbon deposition was relatively unaffected by the increasing of steam. Fig. 5 illustrates the influence of temperature

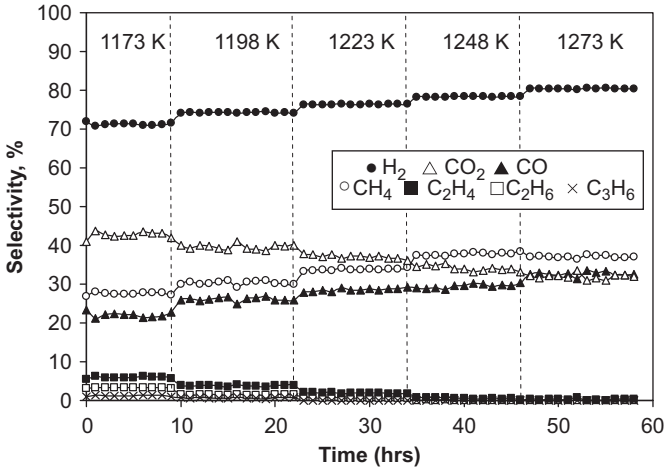

Fig. 5. Effect of temperature on hydrogen and other gaseous product selectivities with time from steam reforming of PFAD over Ce–ZrO_2 with Ce/Zr ratio of 3/1.

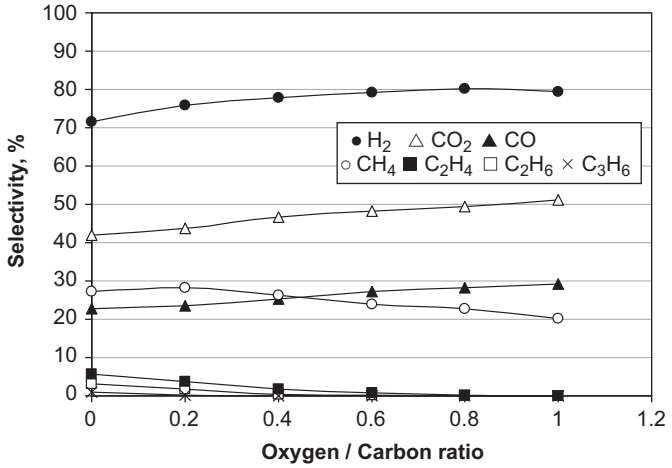

Fig. 6. Effect of inlet oxygen/carbon molar ratio on gaseous product selectivities from steam reforming of PFAD at 1173 K over Ce–ZrO_2 with Ce/Zr ratio of 3/1.

on the hydrogen yield and gaseous product selectivities. Clearly, the activities of catalyst increased with increasing temperature. At 1273 K, the main products from the steam reforming of PFAD over Ce–ZrO_2 were H_2, CO, CO_2, and CH_4, with insignificant amounts of C_2H_4, C_2H_6, and C_3H_6. Table 6 also presents the effect of temperature on the degree of carbon deposition; it can be seen that the amount of carbon formation on Ce–ZrO_2 surface decreased with increasing temperature.

3.4. Reactivity towards reforming of PFAD with co-fed oxygen

According to the results in Section 3.3, Ce–ZrO_2 can reform PFAD efficiently with high resistance toward carbon formation compared to conventional Ni/Al_2O_3. Nevertheless, the major consideration for ceria-based catalyst is its relatively low reforming reactivity, which results in the remains of high hydrocarbons in the product due to the incomplete reforming reaction particularly at low operating temperature (1173–1198 K). These formations could be minimized by increasing the temperature to 1273 K, which means significantly high energy input is required for the system. As an alternative procedure to reduce the formations of these hydrocarbons, oxygen was added in the feed together with PFAD and steam as autothermal reforming operation. In the present work, the inlet steam/carbon molar ratio was kept constant at 3.0, while the inlet O_2/carbon molar ratios were varied from 0.2, 0.4, 0.6, 0.8, to 1.0. The effect of oxygen concentration on product selectivities at 1173 K (after held the system for 10 h at each condition to ensure that the reaction reactivity is stable) is shown in Fig. 6.

It can be seen that hydrogen selectivity increased with increasing O_2/carbon molar ratio until the ratio reached 0.8, then oxygen showed no effect on the hydrogen production at higher inlet O_2/carbon molar ratio values. It should be noted that the conversion of O_2 was always closed to 100% in all testing. Fig. 6 also indicates that the dependence of oxygen on CH_4 production is non-monotonic. At suitable O_2/carbon molar ratio, higher H_2, CO, and CO_2 were observed from the autothermal reforming of PFAD, whereas no formation of C_2H_6, C_2H_4, and C_3H_6 was found compared to the steam reforming at the same operating conditions. The post-reaction oxidation measurement was then carried out to determine the degree of carbon formation on catalyst surface. From the oxidation measurement results shown in Table 7, significantly less quantities of carbon deposited were observed at high O_2/carbon molar ratio.

Table 7
Effects of inlet oxygen/carbon and hydrogen/carbon molar ratio on the degree of carbon formation after exposure in steam reforming of PFAD at 1023 K for 10 h

Catalyst	Oxygen/carbon molar ratio	Hydrogen/carbon molar ratio	Carbon formation (mmol g_{cat}^{-1})
Ce–ZrO_2 (Ce/Zr = 3/1)	0.2	–	4.7
	0.4	–	4.1
	0.6	–	3.6
	0.8	–	3.2
	1.0	–	3.0
	–	0.5	4.8
	–	1.0	4.5
	–	1.5	4.4
	–	2.0	4.2
	–	2.5	4.1
	–	3.0	3.9
	–	3.5	3.9
	–	4.0	3.8
	–	4.5	3.9
	–	5.0	3.8

3.5. Reactivity towards reforming of PFAD with co-fed hydrogen

Previously, we reported that the addition of hydrogen as co-feeding along with oxyhydrocarbon (i.e. ethanol) and steam over Ni catalysts could reduce the degree of carbon formation in the system as well as minimize the presences of intermediate hydrocarbon i.e. C_2H_4 and C_2H_6 occurring form the decomposition of ethanol during reaction (Laosiripojana et al., 2007). Here, we thereby investigated the reactivity of Ce–ZrO_2 towards reforming of PFAD with co-fed hydrogen. The inlet steam/carbon molar ratio was kept constant at 3.0, while the inlet H_2/carbon molar ratios were varied from 0.5 to 5.0. As hydrogen was used as the feed, the effect of this component on the catalyst performance was investigated in term of gaseous hydrocarbon (i.e. CH_4, C_2H_6, C_2H_4, and C_3H_6) distribution instead of hydrogen production selectivity. Fig. 7 presents all product distribution from the steam reforming of PFAD in the presence of hydrogen over Ce–ZrO_2 (after held the system for 10 h at each condition to ensure that the reaction reactivity is stable), while Table 7 also reports the effect of hydrogen adding on the amount of carbon formation.

It was found that, with the presence of hydrogen, less amount of carbon deposited were observed on the surface of Ce–ZrO_2. However, the formations of hydrocarbon particularly CH_4 in the product increased with increasing H_2 content. Thus, the adding of hydrogen

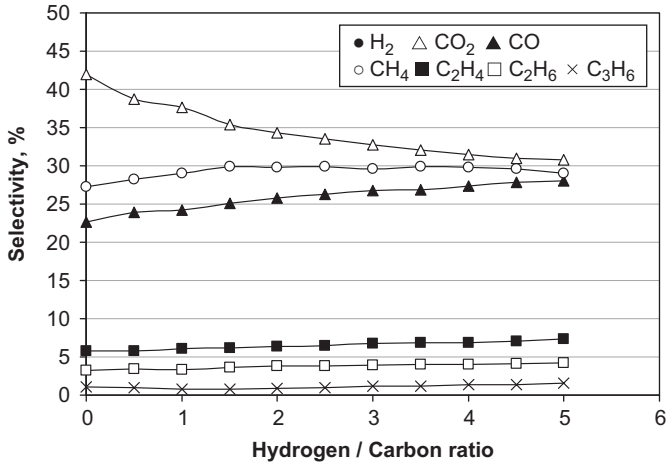

Fig. 7. Effect of inlet hydrogen/carbon molar ratio on gaseous product selectivities from steam reforming of PFAD at 1173 K over Ce–ZrO_2 with Ce/Zr ratio of 3/1.

as co-fed is not the suitable procedure for improving the steam reforming performance of PFAD over Ce–ZrO_2.

4. Discussion

Ce–ZrO_2 (HSA) was found in this study to have good reactivity toward the steam reforming of PFAD with excellent resistance towards carbon deposition compared to conventional Ni/Al_2O_3. Although Ni/Al_2O_3 provided higher initial H_2 yield, the reactivity decreases rapidly with time due to the significant carbon formation on its surface resulting in the low H_2 yield at steady-state condition (Fig. 2, Tables 4 and 5). It is noted that Ce–ZrO_2 (HSA) also presented good reactivity toward steam reforming of palmitic, oleic, and linoleic acids. Among these three fatty acids, the steam reforming of palmitic acid provided highest hydrogen production with lowest presence of hydrocarbons (i.e. CH_4, C_2H_6, C_2H_4, and C_3H_6) in the product; this could be due to the lighter carbon molecule of palmitic acid (C_{16}) compared to oleic and linoleic acids (C_{18}). Nevertheless, the differences are not much significant. At the temperature of 1173 K, the main products from the reforming of PFAD over Ce–ZrO_2 (HSA) were H_2, CO, CO_2, and CH_4 with some amounts of C_2H_6, C_2H_4, and C_3H_6. According to the mechanistic viewpoint, the overall reactions involved in the steam reforming of PFAD are very complex. At such a high operating temperature in the present work, the thermal decomposition of PFAD can take place producing several gaseous products (i.e. hydrogen, carbon monoxide, carbon dioxide, light hydrocarbons (C_nH_m) and oxygenates ($C_nH_mO_x$)) as well as carbon species forming on the surface of catalyst. By feeding steam, the steam reforming of hydrocarbons and oxygenates can then occur along with some side-reactions (e.g. water gas shift reaction and methanation).

$$C_nH_m + nH_2O \rightarrow nCO + (n + 0.5m)H_2 \quad (1)$$

$$C_nH_mO_x + (n - x)H_2O \rightarrow nCO + (n - x + 0.5m)H_2 \quad (2)$$

$$nCO + nH_2O \rightarrow nCO_2 + nH_2 \quad (3)$$

$$nCO + 3nH_2 \rightarrow nCH_4 + nH_2O \quad (4)$$

$$nCO_2 + 4nH_2 \rightarrow nCH_4 + 2nH_2O \quad (5)$$

Previously, we have proposed the redox mechanism to explain the reforming behavior of ceria-based catalysts by indicating that the reforming reaction mechanism involves the reaction between methane, or an intermediate surface hydrocarbon species, and lattice oxygen at the ceria-based material surface (Laosiripojana and Assabumrungrat, 2005). During reforming reaction, the isothermal reaction rate reaches steady-state where co-reactant i.e. steam provides a continuing source of oxygen. We also proposed that the controlling step is the reaction of methane with ceria, and that oxygen is replenished by a significantly more facile surface reaction of the ceria with steam (Laosiripojana and Assabumrungrat, 2005). Therefore, we suggested here that the reaction pathway for steam reforming of PFAD over ceria-based materials involves the reaction between absorbed hydrocarbons (forming intermediate surface hydrocarbon species) with the lattice oxygen (O_O^x) at CeO_2 surface, as illustrated schematically below.

C_nH_m *adsorption*:

$$C_nH_m + (n + m)^* \rightarrow (CH_x^*) + (H^*) \rightarrow n(C^*) + m(H^*) \quad (6)$$

Co-reactant (H_2O) *adsorption*:

$$H_2O + 2^* \Leftrightarrow OH^* + H^* \quad (7)$$

$$OH^* + ^* \Leftrightarrow H^* + O^* \quad (8)$$

Redox reactions of lattice oxygen (O_O^x) *with* C* *and* O*

$$C^* + O_O^x \rightarrow CO^* + V_O^{\cdot\cdot} + 2e' \quad (9)$$

$$V_O^{\cdot\cdot} + 2e' + O^* \Leftrightarrow O_O^x + ^* \quad (10)$$

Desorption of products (CO and H_2)

$$CO^* \Leftrightarrow CO + ^* \quad (11)$$

$$2(H^*) \Leftrightarrow H_2 + 2^* \quad (12)$$

Using the Kroger–Vink notation, $V_O^{\cdot\cdot}$ denotes as an oxygen vacancy with an effective charge 2^+, and e' is an electron which can either be more or less localized on a cerium ion or delocalized in a conduction band. * is the surface active site of ceria-based materials, there are two possibilities for this scheme depending on what is assumed for the catalyst active site. It can be a unique site, or can also be considered to be the same site as the catalyst oxidized site (O_x) (Laosiripojana and Assabumrungrat, 2005). During the reactions, hydrocarbons adsorbed on * forming intermediate surface hydrocarbon species (CH_x^*) (Eq. (6)) and later reacted with the lattice oxygen (O_O^x) (Eq. (9)). The steady-state reforming rate is due to the continuous supply of the oxygen source by H_2O (Eqs. (7) and (8)) that reacted with the reduced-state catalyst to recover lattice oxygen (O_O^x) (Eq. (10)).

The high resistance towards carbon deposition for ceria-based catalysts particularly Ce–ZrO_2 (HSA) is mainly due to the high OSC of material. Previously, we reported the excellent resistance towards carbon deposition for CeO_2 especially for HSA CeO_2 (Laosiripojana and Assabumrungrat, 2005). CeO_2 contains a high concentration of highly mobile oxygen vacancies and thus acts as a local source or sink for oxygen on its surface. It has been reported that at high temperature the lattice oxygen (O_O^x) at the CeO_2 surface can oxidize gaseous hydrocarbons (methane Laosiripojana and Assabumrungrat, 2005, propane and butane Laosiripojana and Assabumrungrat, 2006). Although conventional CeO_2(CeO_2 (LSA)) has also been reported to provide high resistance towards carbon formation, the major weaknesses of CeO_2 (LSA) are its low specific surface area and also high size reduction due to the thermal sintering impact, resulting in its significant lower redox properties than CeO_2 (HSA). These disadvantages result in the low steam reforming reactivity for CeO_2 (LSA). It was also concluded here that the addition of ZrO_2 on CeO_2 promoted the reforming reactivity, which is in good agreement with the literatures.

According to our interested reaction (steam reforming of PFAD), carbon formation could occur from the decompositions of fatty acids

and gaseous hydrocarbon products. Theoretically, it can also occur from the Boudouard reaction especially at low inlet steam/carbon molar ratio:

$$2CO \Leftrightarrow CO_2 + C \quad (13)$$

These reactions could be inhibited by the redox reaction between the surface carbon (C) with the lattice oxygen (O_O^x) at CeO_2 surface:

$$C + O_O^x \rightarrow CO + V_O^{\cdot\cdot} + 2e' \quad (14)$$

The greater resistance toward carbon deposition for HSA ceria-based catalyst particularly Ce–ZrO_2 (HSA) is due to the significant higher amount of lattice oxygen (O_O^x) on their surfaces, according to the results in Section 3.1.

It was also observed from the study that the addition of either oxygen or hydrogen together with PFAD and steam reduced the degree of carbon deposition. By addition of oxygen along with PFAD and steam as autothermal reforming, the partial oxidation of fatty acids takes place and fatty acids could possibly oxidize to methane and carbon monoxide; thus, the rate of fatty acid decomposition reduces and less C_2H_6, C_2H_4, and C_3H_6 are generated, which consequently results in the lower degree of carbon deposition on the surface of catalyst. In addition, oxygen also prevents the formation of carbon species via the hydrocarbon depositions by oxidizing these hydrocarbons to gaseous elements that are unfavored to form carbon species. Importantly, the presence of oxygen also helps steam to regenerate the lattice oxygen (O_O^x) on CeO_2 surface ($0.5O_2 + V_{O^{\cdot\cdot}} + 2e' \rightarrow O_O^x$), which eventually help promoting the reforming reactivity of ceria. It is noted that the major consideration of the autothermal reforming operation is the O_2/carbon ratio. The presence of too high oxygen concentration could oxidize hydrogen produced from the reaction and generate more steam.

By adding hydrogen at the feed, the degree of carbon formation also reduced due to the hydrogenation reaction. Nevertheless, it was found that in the presence of hydrogen at the feed the formations of hydrocarbon particularly CH_4 in the product increased. This negative effect of hydrogen appearance on CH_4, C_2H_4, and C_2H_6 conversions could be due to the hydrogenation of adsorbed CH_x species with this adding hydrogen and also from reduction of lattice oxygen by hydrogen and consequently inhibits the reaction of the lattice oxygen with the surface hydrocarbon species. This explanation is in good agreement with our previous studies (Laosiripojana and Assabumrungrat, 2005) which studied kinetics parameters for the methane steam reforming on ceria-based materials and reported the negative effect of hydrogen on methane conversion.

5. Conclusion

Steam reforming of free fatty acids (i.e. palmitic, oleic and linoleic acids) and palm fatty acid distilled (PFAD) were tested over ceria-based materials prepared by precipitation and cationic surfactant-assisted methods with/without Zr doping. Among all ceria-based catalysts, Ce–ZrO_2 (with Ce/Zr ratio of 3/1) from cationic surfactant-assisted method (Ce–ZrO_2 (HSA)) provided the highest degree of oxygen storage capacity (OSC) and steam reforming reactivity with greatest resistance toward carbon deposition. At 1173 K, the main products from the steam reforming of PFAD over Ce–ZrO_2 (HSA) are H_2, CO, and CO_2 with some amounts of CH_4, C_2H_4, C_2H_6, and C_3H_6; the formations of high hydrocarbon can be eliminated by increasing the operating temperature up to 1273 K.

The addition of either oxygen or hydrogen together with PFAD and steam reduced the degree of carbon deposition. The presence of oxygen also reduced the formations of C_2H_6, C_2H_4, and C_3H_6 due to the possible oxidation of fatty acids, which is eventually converted to methane and carbon monoxide. At suitable O_2H_2O/PFAD ratio, high H_2 selectivity without the formation of C_{2+} hydrocarbon was achieved. On the other hand, in the presence of hydrogen at the feed the formations of hydrocarbon in the product increased. This negative effect of hydrogen appearance on CH_4, C_2H_4, and C_2H_6 conversions is due to hydrogenation reaction and the reduction of lattice oxygen by hydrogen, which consequently inhibits the reaction of the lattice oxygen with the surface hydrocarbon species.

Acknowledgements

The financial support from The Thailand Research Fund (TRF) and National Metal and Materials Technology Center (MTEC) throughout this project is gratefully acknowledged.

References

Balducci, G., Kaspar, J., Fornasiero, P., Graziani, M., Islam, M.S., 1998. Journal of Physical Chemistry B 102, 557.
Basagiannis, A.C., Verykios, X.E., 2006. Applied Catalysis A 308, 182.
Basagiannis, A.C., Verykios, X.E., 2007. International Journal of Hydrogen Energy 32, 3343.
Basagiannis, A.C., Verykios, X.E., 2008. Applied Catalysis B 82, 77.
Czernik, S., French, R.J., Magrini-Bair, K.A., Chornet, E., 2004. Energy Fuels 18, 1738.
Davidian, T., Guilhaume, N., Daniel, C., Mirodatos, C., 2008. Applied Catalysis A 335, 64.
Fatsikostas, A.N., Kondarides, D.I., Verykios, X.E., 2002. Catalysis Today 75, 145.
Fornasiero, P., Dimonte, R., Rao, G.R., Kaspar, J., Meriani, S., Trovarelli, A., Graziani, M., 1995. Journal of Catalysis 151, 168.
Galdámez, J.R., García, L., Bilbao, R., 2005. Energy Fuels 19, 1133.
Kaspar, J., Fornasiero, P., Graziani, M., 1999. Catalysis Today 50, 285.
Kim, D., 1989. Journal of the American Ceramic Society 72, 1415.
Kruse, N., Frennet, A., Bastin, J.M. (Eds.), 1998. Catalysis and Automotive Pollution Control IV. Elsevier, Amsterdam.
Laosiripojana, N., Assabumrungrat, S., 2005. Applied Catalysis B: Environmental 60, 107.
Laosiripojana, N., Assabumrungrat, S., 2006. Journal of Power Sources 158, 1348.
Laosiripojana, N., Assabumrungrat, S., Charojrochkul, S., 2007. Applied Catalysis A 327, 180.
Liguras, D.K., Kondarides, D.I., Verykios, X.E., 2003. Applied Catalysis B: Environmental 43, 345.
Ozawa, M., Kimura, M., Isogai, A., 1993. Journal of Alloys and Compounds 193, 73.
Polychronopoulou, K., Costa, C.N., Efstathiou, A.M., 2004. Applied Catalysis A 272, 37.
Ramirez, E., Atkinson, A., Chadwick, D., 2002. Applied Catalysis B 36, 193.
Ramírez-Cabrera, E., Laosiripojana, N., Atkinson, A., Chadwick, D., 2003. Catalysis Today 78, 433.
Rao, G.R., Kaspar, J., Meriani, S., Dimonte, R., Graziani, M., 1994. Catalysis Letters 24, 107.
Roh, H.S., Potdar, H.S., Jun, K.W., 2004. Catalysis Today 93–95, 39.
Takanabe, K., Aika, K., Seshan, K., Lefferts, L., 2004. Journal of Catalysis 227, 101.
Terribile, D., Trovarelli, A., Llorca, J., Leitenburg, C., Dolcetti, G., 1998a. Journal of Catalysis 178, 299.
Terribile, D., Trovarelli, A., Llorca, J., Leitenburg, C., Dolcetti, G., 1998b. Catalysis Today 43, 79–88.
Vlaic, G., Fornasiero, P., Geremia, S., Kaspar, J., Graziani, M., 1997. Journal of Catalysis 168, 386.
Wang, D., Montané, D., Chornet, E., 1996. Applied Catalysis A 143, 245.
Wang, D., Czernik, S., Montané, D., Mann, M., Chornet, E., 1997. Industrial and Engineering Chemistry Research 36, 1507.
Yao, M.H., Hoost, T.E., Baird, R.J., Kunz, F.W., 1997. Journal of Catalysis 166, 67.